U.PORTO

FEUP FACULDADE DE ENGENHARIA
UNIVERSIDADE DO PORTO

An Assessment of the Principle of Separation of Scales in Coupled Multi-Scale Finite Element Analyses

Luís Justino Fernandes Pedreira Alves

Master's Degree in Mechanical Engineering

Supervisor:
Prof. Francisco Manuel Andrade Pires

Second Supervisors:
Eng. Igor André Rodrigues Lopes
Dr. Daniel de Bortoli

June, 2018

Abstract

An Assessment of the Principle of Separation of Scales in Coupled Multi-Scale Analyses

Multi-scale constitutive models are a new approach in computational mechanics. Their ability to predict complex material behaviours and to assess properties at both the micro and macro-scales makes them extremely attractive for structural mechanics analyses. This type of models are based in computational homogenization, therefore, for such models to be applied, the principle of separation of scales must be verified.

Throughout the work of this thesis the principle of separation of scales is assessed for different characteristics sizes of RVEs, different kinds of macro-scale specimens, solicitations and material behaviours and, lastly, for different kinds of heterogeneities. The principle of separation of scales is evaluated by comparing results provided by the multi-scale models with corresponding DNS analysis in terms of their macro-scale response (reaction forces/bending moments) and, also, in terms of the micro-scale distribuition of the the equivalent Cauchy stress and equivalent strain fields. Furthermore a study about the results provided by a second-order homogenisation method is made, where the characteristic absolute length of the RVE plays a major role in the results obtained at the micro-scale (in the first-order homogenisation method, the RVE size is irrelevant for the results obtained, i.e., the results are equal for all RVEs' characteristic length). From all the analyses performed it is possible to conclude that the RVE length by its own, does not provide information whether the principle of separation of scales will be validated or not. For such a violation to happen, the magnitude of the deformation variation "inside" the RVE in the DNS analysis needs to be large enough. In this case, a second-order homogenisation is useful since the results are affected by the RVE, thus providing results more approximates to the ones obtained by a DNS analysis.

Keywords: Micromechanics; Multi-Scale models; Homogenization; DNS Model; Principle of Separation of Scales; Representative Volume Element;

Resumo

Uma Avaliação do Princípio de Separação de Escalas em Análises Acoplada Multi-Escala

Os modelos multi-escala são a nova tendência na área da mecânica computacional. A sua capacidade para prever comportamentos de materiais complexos bem como de avaliar propriedades tanto à macro como à micro-escala fazem com que estes modelos se tornem bastante atrativos no que diz respeito a análises do foro da mecânica estrutural. Este tipo de modelos são baseados em homogeneização computacional, e, como tal, o princípio de separação de escalas tem de ser satisfeito para que eles possam ser utilizados.

Ao longo desta tese o princípio de separação de escalas é avaliado para diferentes tamanhos de RVE, diferentes tipos de provetes/geometrias à macro-escala, solicitações, comportamentos de materiais e, por último, para diferentes tipos de heterogeneidades. O princípio de separação de escalas é avaliado através da comparação dos resultados obtidos através dos modelos multi-escala com simulações equivalentes DNS em termos dos resultados obtidos à macro-escala (forças de reação/momentos fletores), bem como à micro-escala tendo em consideração as distribuições da tensão efetiva de Cauchy e da deformação equivalente. Para além disso é ainda feito um estudo acerca dos resultados obtidos através da utilização de um modelo de homogenização de segunda ordem, onde o tamanho absoluto do RVE desempenha um papel preponderante nos resultados obtidos à micro-escala (em homogenização de primeira ordem o tamanho absoluto do RVE não influencia os resultados, isto é, os resultados obtidos são idênticos para tamanhos diferentes de RVE). Através de todas as análises mencionadas acima é possível concluir que o tamanho do RVE, por si próprio, não desempenha um grande papel no não cumprimento do princípio de separação de escalas, uma vez que para isso acontecer, é necessário que os fenómenos de deformação tenham uma magnitude de variação no interior do RVE da análise DNS muito grande, isto é tem de existir um gradiente espacial de deformação "grande" no interior do RVE para que o princípio de separação de escalas não possa ser validado. Nestes casos, um modelo multi-escala com homogenização de segunda ordem é vantajoso uma vez que consegue captar este tipo de fenómeno, fazendo com que os resultados sejam mais próximos dos obtidos por análises DNS.

Palavras-chave: Micro-mecânica; Modelos Multi-Escala; Homogeneização; Modelos DNS; Princípio de Separação de Escalas; Elemento de Volume Representativo; Materiais heterogéneos.

Acknowledgements

First of all, I would like to thank my supervisor, Professor Francisco Pires, for all the support and advices given while structuring and documenting this thesis. It is truly satisfying to have the opportunity to work with someone that always promotes critical thinking and that provides encouragement even when the results are not the best. Secondly, I would like to thank my co-supervisor Igor for his patience and availability to clarify all my questions, to provide me the tools that were needed for the accomplishment of this work and for his good mood. It is unquestionable his relevance in the accomplishment of this work. To Daniel also a kind word for his attention and interest while discussing results and problems that took place. Also to the other members of the CM2S group, a kind word for making me feel part of the group and for promoting good spirit among the group. To the friends that I had the opportunity to share this journey, Luís Oliveira, Gomes, Moreira, Rafael Vieira, Samuel, Ricardo, João Costa, Kevin, Costa, William, Bernardo, Mariana and Rosa and many others a sincere thank you for all the experiences that we shared throughout this five years. To my childhood friends, João Moreira, Guilherme, Francisco, João Pedro and Paulo Campos a special thank you for being my support throughout this years. Most of the times we may be apart but the same friendship still remains. A special tanks to Fortunato for always being present even when things weren't going as expected and for being a support throughout this years. Lastly, but not the least, I would like express my sincere words to my family, specially to my parents, for the education that they gave me and for the effort that they made all this years to never lack anything. Thank you also for always encouraging me to follow my dreams and for always being by my side. An apology is also due for my absence during this years, especially during this semester.

A special thanks to all of you,
Luís Justino Fernandes Pedreira Alves

"Successfull engineering is all about understanding how things break or fail"

Henry Petrosky

Contents

List of Figures

List of Tables

Nomenclature

Notation

a	Scalar value;
$\boldsymbol{a}$	Vector;
$\boldsymbol{A}$	Second-order tensor;
$\mathbf{a}$, $\mathbf{A}$	Finite elements' related array (vector and tensor);
A	Third-order tensor;
$\mathscr{A}$	Space or Body;
$\boldsymbol{x}$	Macroscopic spatial coordinate;
$\boldsymbol{X}$	Macroscopic material coordinate;
$\boldsymbol{y}$	Microscopic spatial coordinate;
$\boldsymbol{Y}$	Microscopic material coordinate

Acronyms

2D	Two dimensional;
3D	Three dimensional;
RVE	Representative Volume Element;
LINKS	Large Strain Implicit Non-Linear Finite Element Analysis of Solids Linking Scales;
FEM	Finite Element Method
PSS	Principle of Separation of Scales;
DOF	Degrees of Freedom;
nGP	Number of Gauss Points;
GP	Gauss Point;
DNS	Direct Numerical Simulation;
VVF	Void Volume Fraction

Indices

$(\cdot)_t$	Time dependent;
$(\cdot)_{\text{iso}}$	Isochoric component;
$(\cdot)_{\text{v}}$	Volumetric component;
$\bar{(\cdot)}$	Reference configuration;
$(\cdot)^d$	Discretized domain;
$(\cdot)^e$	Element domain;
$(\cdot)^g$	Global domain;
$(\cdot)^{(j)}$	Generic iterative step of the Newton-Raphson method;
$(\cdot)^{+/-}$	Positive/negative part of the periodic boundary of the RVE;

Operators

$\dot{(\cdot)}$	Time derivative;
$\ddot{(\cdot)}$	Second time derivative;
$\partial(\cdot)$	Boundary domain;
$\partial(\cdot)/\partial a$	Derivative with respect to a;
$\nabla(\cdot)$	Gradient;
$\nabla^s(\cdot)$	Symmetric gradient;
$\nabla^x(\cdot)$	Spatial gradient;
$\nabla^X(\cdot)$	Material gradient;
$\text{tr}(\cdot)$	Trace;
$\det(\cdot)$	Determinant;
$\mid (\cdot) \mid$	Scalar norm (absolute value);
$\parallel (\cdot) \parallel$	Euclidean norm of vectors or tensors;
$\ln(\cdot)$	Natural logarithm;
$\text{div}_x(\cdot)$	Spatial divergence;
$\text{div}_x(\cdot)$	Material divergence;
$(\cdot) : (\cdot)$	Double contraction of tensors;
$(\cdot) \cdot (\cdot)$	Simple contraction of tensors;
$(\cdot) \times (\cdot)$	Vector product;
$(\cdot) \otimes (\cdot)$	Tensor product;
$\bigcup(\cdot)$	Union operator;
$\mathsf{A}(\cdot)$	Assemblage of finite elements;

Chapter 1

Introduction

In the branch of structural mechanics, numerical methods are commonly used to predict the response of a certain structural component for a set of diverse loads. One of the numerical methods most widely utilised is the finite element method. However it is of utmost importance that the behaviour of the materials is modelled with precision. So that such goal to be achieved, and with the constant innovation in terms of materials that is going on, it is necessary to develop new constitutive models such that they can capture the behaviour of more complex materials. Multi-scale models belong to the type of constitutive models which incorporate information from two (or more) scales of observation simultaneously. This type of problems have their basis in the continuum mechanics theories where a microscopic equilibrium problem is solved from a solicitation that is applied at the macro-scale. This micro-macro modelling procedure defines the stress-strain relation at each macroscopic point through a homogenization procedure, which involves a solution of a boundary problem over a statistically Representative Volume Element (RVE). In practice, considering the finite element method, this numerical approach consists in solving simultaneously two boundary problems: the macroscopic problem and the microscopic boundary value problem at each macroscopic integration Gauss point. These can only be applied if the principle of separation of scales is satisfied, this is, the micro-structure needs to be representative, i.e., the characteristic size of the micro-structure - representative volume element (RVE)- needs to be much smaller than the macro-scale size and larger than the size of the material heterogeneities.

In order to assess this principle, it is possible to compare the solution obtained by this type of models with a corresponding direct numerical simulation (DNS) where the micro-structure of the material is explicitly modelled. Nevertheless, this type of models (DNS) can be extremely heavy in computational time and memory. Therefore, in DNS models only a macro-scale problem is solved and the "interactions" between the micro and macro-scales cannot be replicated. The coupled multi-scale finite element analysis aims to solve this problem and it is less heavy in computational resources than the DNS analysis, therefore it is of utter importance to study, develop and optimize this type of constitutive models.

1.1 Goals

The main goal of the work developed in this semester is to evaluate the effects of the RVE characteristic length in the principle of separation of scales. This principle will be evaluated by comparing the macroscopic response (reaction forces/bending moment) of the DNS models and the correspondent multi-scale one. The microscopic response is also going to be assessed in terms of the effective Cauchy and equivalent strain fields by comparing a RVE of the DNS model to an "equivalent" in the multi-scale model.

Other goals of this work are to study the influence of different types of loadings (traction/bending), different types of materials and different types of micro-structures in this principle.

One final goal of this work is also to show that in some cases a second-order homogenisation scheme is needed in order to obtain a better characterization of the microscopic properties.

1.2 Structure of the Document

In this section, the overall structure of the document is going to be addressed. Furthermore, a brief introduction to the chapters is made in this section.

Chapter 2

In this chapter, the fundamentals of both the *Continuum Mechanics* and the *Finite Element Method* are presented. The theories that rule the behaviour of a general body under deformation are introduced. The formulation that is used is made under assumption of large deformations theory. The numerical implementation of this problem is also briefly described in the context of the finite element method.

Chapter 3

In this chapter the fundamentals of the *Multi-Scale models* are going to be presented. The concept of a Representative Volume Element is introduced and it's described the concept of homogenisation (both first and second order). The admissible kinematical boundary conditions are also described. Finally the procedure of obtaining the solution of the micro-scale equilibrium problem is presented.

Chapter 4

In this chapter the principle of separation of scales is evaluated for two different kind of sprecimens with different geometries (one has a 4 mm notch and the other as a 12 mm one). The DNS models that have been utilised are presented as well as the corresponding multi-scale ones for three different RVE characteristic sizes and for two different types of microstructure (one with a circular void and another with an elastic inclusion).

Chapter 5

An assessment of the principle of separation of scales for two different types of beams under a bending loading is conducted and presented. The DNS and multi-scale models are described as well as the results that were obtained. A second-order homogenisation scheme is used to obtain the solution at the micro-scale of one of the examples and it is compared to the first-order homogenisation solution.

Chapter 6

Following the study of the bending loading a study about the effects of the material behaviour for the worst-case scenario that was determined in the previous chapter is made. Again, a second-order homogenisation scheme is used for obtaining the solution at the micro-scale of one of the examples.

Also, an assessment of the principle of separation of scales is made taking into account the void volume fraction of heterogeneities that are embeded in the micro-structure.

Chapter 7

Finally, in this chapter, a conclusion note about the work performed in this thesis is presented, along with suggestions to keep investigating this models in future works.

Chapter 2

Continuum Mechanics and Thermodynamics. Finite Element Method

Before beginning the discussion of *Multi-Scale Models* there are some base concepts that one must be familiar with. To be able to create a model that can depict the behavior of a solid, one needs to know its physical relations and entities, being *Continuum mechanics* the theory that establishes them. Although all materials are constituted by atoms and subatomic particles, at larger scales, one can assume that the material is continuous. Thus, the term "particle" will be referred in this chapter as an infinitesimal volume of material being so that the "sum" of the particles in the material forms its body. Given that, in the discipline of *Continuum Mechanics* the kinematics and the mechanical behavior of the materials are studied assuming that the medium is continuum instead of considering that the medium is constituted by discrete particles.

In many engineering problems, the complexity of the geometry of the bodies and/or the constitutive models that model their behaviour are difficult to solve, in an analytical way, since they are usually governed by a set of differential equations. Thus, for such models it is required to employ numerical approximations. The *Finite Element Method* is a powerful and commonly used tool among the industry and the scientific community to solve problems in the domain of solid and structural mechanics. This method relies in dividing the domain of the problem in a finite number of smaller parts (sub-domains or finite elements) and to solve a system of equations (on which the equations of each finite element are assembled) that can approximate the mechanical behavior of the body to be studied.

In this chapter the topics discussed above are going to be introduced taking into account the work of Neto et al. (2011) and Rubin et al. (2012). For a more detailed study of the topics discussed in this chapter the works of Holzapfel (2000) and Tadmor et al. (2012) are suggested for the *Continuum Mechanics* topic. For the *Finite Element Method* the works of Zienkiewicz et al. (2013) and Zienkiewicz and Taylor (2000) are recommended.

2.1 Kinematics of Deformation

Taking into account the body $\mathscr{B}$ which occupies a certain region Ω with a regular boundary $\partial\Omega$ in the three-dimensional Euclidean space $\mathscr{E}$ in its reference configuration. The deformation of the body $\mathscr{B}$ can be expressed as the function

$$\varphi : \Omega \to \mathscr{E}.$$

The deformation of the body occurs due to its displacement, which can be decomposed in two components (see Figure 2.1):

- **Rigid-body displacement** which is said to occur when all particles of the body maintain the same relative distance between even tough the body has experienced a translation and/or rotation. This results in the body maintaining its reference shape.
- **Deformation** is the opposite of a rigid-body deformation or deformation. The particles that constitute the body experience changes in their relative distance leading to the occurrence of modifications of the shape/size of the body relative to its reference configuration.

Taking into consideration a particle $\boldsymbol{X} \in \mathscr{B}$ one can express it's position utilising the function that maps the deformation of the body. Thus, the point where the particle lies can be expressed as

$$\boldsymbol{x} = \varphi(\boldsymbol{X}), \tag{2.1}$$

where $\boldsymbol{X}$ refers to the position of the particle p in its reference configuration and x to the deformed configuration of the body.

The displacement field of the particle, $\boldsymbol{u(X)}$, can be expressed by

$$\boldsymbol{u(X)} = \varphi(\boldsymbol{X}) - \boldsymbol{X}, \tag{2.2}$$

making it possible to express the position of the particle in its deformed configuration by the function

$$\boldsymbol{x} = \boldsymbol{X} + \boldsymbol{u(X)}. \tag{2.3}$$

A rigid deformation of a body due to displacements of translation and/or rotation is said to occur if and only it is expressed by

$$\varphi(\boldsymbol{X}) = \varphi(\boldsymbol{q}) + \boldsymbol{R}(\boldsymbol{X} - \boldsymbol{q}), \tag{2.4}$$

being $\boldsymbol{R}$ a rotation tensor and $\boldsymbol{q}$ the point about the rotation of the body $\mathscr{B}$ occurs.

One can define a *motion of* $\mathscr{B}$ as a time dependent deformation of $\mathscr{B}$ and it can be expressed by the function

$$\varphi : \Omega \times \mathscr{R} \to \mathscr{E}.$$

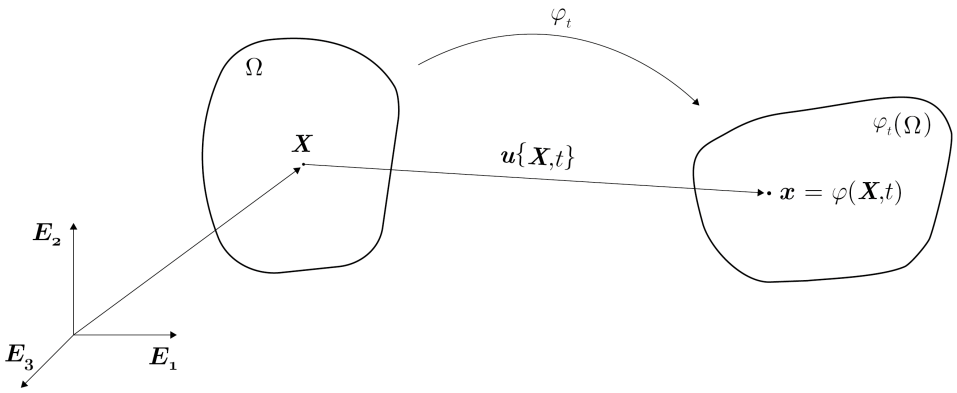

Figure 2.1: Deformation of a body. Adapted from Neto et al. (2011).

The expression presented above allows one to be able to define the deformation map at a general time, t, as being a function of the particle's position in the reference state $\boldsymbol{X}$ and the time, t. Thus, during the motion of the body, the deformed position, $\boldsymbol{x}$, of the particle at a certain time, t, can be determined by

$$\boldsymbol{x} = \varphi(\boldsymbol{X}, t). \tag{2.5}$$

The motion is expressed in terms of the displacement field as

$$\varphi(\boldsymbol{X}, t) = \boldsymbol{X} + \boldsymbol{u}(\boldsymbol{X}, t). \tag{2.6}$$

The function that maps the motion will also be denoted as φ_t throughout this document.

Attending to equations (2.5) and (2.6) one can write

$$\boldsymbol{x} = \boldsymbol{X} + \boldsymbol{u}(\boldsymbol{X}, t). \tag{2.7}$$

Having the expression for the position of the particle in the deformed configuration depending of the considered time instant t (see Equation (2.7)), one can describe the velocity of a material particle as

$$\dot{\boldsymbol{x}}(\boldsymbol{X}, t) = \frac{\partial \varphi(\boldsymbol{X}, t)}{\partial t}. \tag{2.8}$$

The place that material points occupy at a certaint time, t, can be formulated due to the fact that the map $\varphi(\bullet, t)$ is considered to be invertible by assumption as a result of the map being considered a one-to-one function. Hence, the expression of the location of the material points comes as

$$\boldsymbol{X} = \varphi^{-1}(\boldsymbol{x}, t) = \boldsymbol{x} - \boldsymbol{u}^{-1}(\varphi^{-1}(\boldsymbol{x}, t), t). \tag{2.9}$$

The term φ^{-1} is labeled as reference map and by means of its use one can define the function

$$\boldsymbol{v}(\boldsymbol{x}, t) \equiv \dot{\boldsymbol{x}}(\varphi^{-1}(\boldsymbol{x}, t)), \tag{2.10}$$

being the field $\boldsymbol{v}$ referrenced as the *spatial velocity* which contains information about the velocity of the material particle positioned at $\boldsymbol{x}$ at a time,t.

2.1.1 Material and Spatial Fields

Analyzing and comparing the arguments that are present in Equation (2.8) and Equation (2.10) it is possible to state that both equations have different physical meaning. Hence, it is possible to make a distinction between *Material* and *Spatial* fields. Both of them have time as an argument but the first one (Equation (2.8)) has the material particle $\boldsymbol{X}$ as an argument and the second one (Equation (2.10)) has the spatial position $\boldsymbol{x}$.

Material field is also commonly known as *Lagrangean formulation* and contains information about the evolution of certain variables in a fixed material point $\boldsymbol{X}$. Spatial field is also known has *Eulerian formulation* and consists in evaluating the variables in a fixed point of space $\boldsymbol{x}$.

2.1.2 Deformation Gradient

The deformation gradient is a second-order tensor of the motion φ, $\boldsymbol{F}$, which is defined by

$$\boldsymbol{F}(\boldsymbol{X},t) = \nabla_X \ \varphi(\boldsymbol{X},t) = \frac{\partial \boldsymbol{x}_t}{\partial \boldsymbol{X}}. \tag{2.11}$$

Accordingly to the equation (2.6), the expression written above can be expressed also as

$$\boldsymbol{F} = \boldsymbol{I} + \nabla_X \ \boldsymbol{u}. \tag{2.12}$$

Taking into consideration the reference map (see equation (2.9)) the deformation gradient is expressed by

$$\boldsymbol{F}(\boldsymbol{x},t) = [\nabla_x \ \varphi^{-1}(\boldsymbol{x},t)]^{-1} = [\boldsymbol{I} - \nabla_x \ \boldsymbol{u}]^{-1}. \tag{2.13}$$

In Equation (2.11) and Equation (2.13) the gradient operators, ∇_X and ∇_x, refer to material and spatial descriptions respectively. Aiming to understand the concept of the deformation gradient, one infinitesimal material fibre is going to be considered. The infinitesimal material fibre $d\boldsymbol{X}$ connects two adjoining material particles $\boldsymbol{X}$ and $\boldsymbol{X} + d\boldsymbol{X}$. Once the deformation φ_t occurs, the particles will have new positions that can be expressed by $\boldsymbol{x}$ and $\boldsymbol{x} + d\boldsymbol{x}$. The relation between the deformed fibers, $d\boldsymbol{x}$, and the material ones, $d\boldsymbol{X}$, can be made employing the *deformation gradient* operator. Hence, the deformation gradient, $\boldsymbol{F}$, is considered to be the linear operator that establishes the relationship between the infinitesimal material fibers with their deformed and homologous deformed fibers. Hence, one can write

$$d\boldsymbol{x} = \boldsymbol{F} \ d\boldsymbol{X}. \tag{2.14}$$

If the deformation gradient is independent of the the particle $\boldsymbol{X}$ one can state that the deformation gradient is uniform. Hence, a deformation of a body $\mathscr{B}$ in this conditions is known

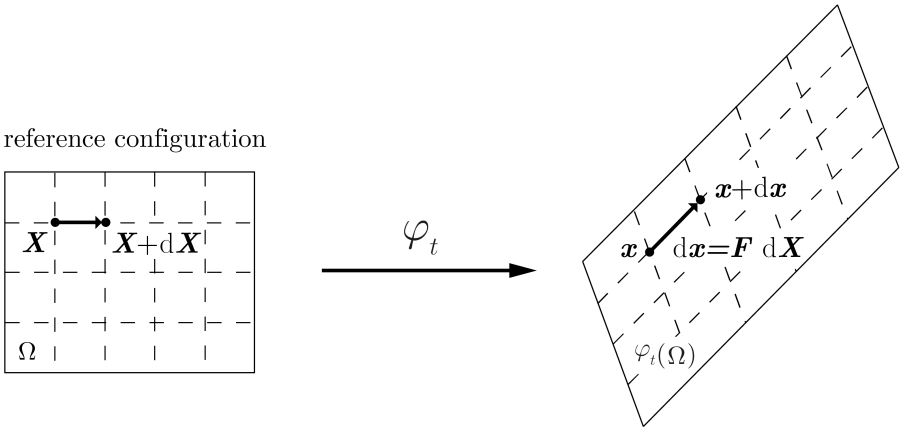

Figure 2.2: Deformation Gradient. Adapted from Neto et al. (2011).

as an *homogenous deformation* and it is represented by

$$\varphi(\boldsymbol{X}) = \varphi(\boldsymbol{Q}) + \boldsymbol{F}(\boldsymbol{X} - \boldsymbol{Q}), \tag{2.15}$$

being $\boldsymbol{X}$, $\boldsymbol{Q}$ points belonging to a body, $\mathscr{B}$, and $\boldsymbol{F}$ a positive definite tensor. As examples of homogenous deformations, one can point the displacements of rigid translations and rotations.

Isochoric and Volumetric Decomposition of the Deformation Gradient

It is possible to decompose, locally, any type of deformation in terms of its volumetric and/or isochoric components. Before introducing the theory of the decomposition of the deformation gradient it is important to understand the physical meaning of the determinant of the deformation gradient. The determinant of the deformation gradient represents, locally, the ratio between the volume after deformation and the reference volume. Hence, the determinant of the deformation gradient can be expressed as a volume change ratio being written as

$$J \equiv \det \boldsymbol{F}. \tag{2.16}$$

It is important to state some restrictions upon the values that J can take from a physical point of view. Attending to equation (2.16) one can state that:

- $J \neq 0$, since the body cannot collapse into a single particle.
- $J > 0$, since for the situation of $J < 0$ to happen, at some time, the condition of $J = 0$ would have to happen, which is impossible, given that the deformation map is assumed to be one-to-one.

Having been introduced the concept of the determinant of the deformation gradient one can proceed to the definition of the following types of deformations:

Isochoric deformation - by definition an isochoric deformation does not produce variations in volume, consequently, one can write

$$J = 1, \tag{2.17}$$

for an isochoric deformation.

Volumetric deformation - in a volumetric deformation occurs contractions ($J < 1$)/dilatations ($J > 1$) uniformly in all directions. In this type of deformation, the deformation gradient can be expressed by the tensor

$$\boldsymbol{F} = \alpha \boldsymbol{I}, \tag{2.18}$$

being the scalar α the corresponding dilatation/contraction (deformation) ratio. Taking into account the example of the material fibers, the deformation ratio can be obtained by dividing the length of the deformed fiber, l by the length of the undeformed fiber l_0 resulting in

$$\alpha = \frac{l}{l_0}. \tag{2.19}$$

As it is already been stated, the local deformation of a body can be decomposed in its isochoric and volumetric components. Hence, one can decompose the deformation of a body in an isochoric deformation followeb by a volumetric deformation and vice versa. Accordingly, the deformation gradient can be multiplicatively split as

$$\boldsymbol{F} = \boldsymbol{F}_{\mathbf{iso}}\ \boldsymbol{F}_{\mathbf{v}} = \boldsymbol{F}_{\mathbf{v}}\ \boldsymbol{F}_{\mathbf{iso}}, \tag{2.20}$$

being

$$\boldsymbol{F}_{\mathbf{v}} \equiv (\det \boldsymbol{F})^{\frac{1}{3}} \boldsymbol{I} \tag{2.21}$$

$$\boldsymbol{F}_{\mathbf{iso}} \equiv (\det \boldsymbol{F})^{-\frac{1}{3}}\ \boldsymbol{F}. \tag{2.22}$$

Some important statements should be made about the split of the deformation gradient in its isochoric and volumetric components. Accordingly to Equation(2.21) and Equation (2.22) one can verify that:

$$\det \boldsymbol{F}_{\mathbf{v}} = [(\det \boldsymbol{F})^{\frac{1}{3}}]^3\ \det \boldsymbol{I} = \det \boldsymbol{F}, \tag{2.23}$$

and

$$\det \boldsymbol{F}_{\mathbf{iso}} = [(\det \boldsymbol{F})^{-\frac{1}{3}}]^3\ \det \boldsymbol{F} = 1. \tag{2.24}$$

Attending to Equation (2.23) and Equation (2.24) that are presented above, there are some important remarks to be made. Firstly, one can verify that $\boldsymbol{F}_{\mathbf{v}}$ produces the same change in volume that $\boldsymbol{F}$, corresponding indeed to a purely volumetric decomposition. Furthermore one can also verify that $\boldsymbol{F}_{\mathbf{iso}}$ doesn't produce any changes in volume, corresponding to a purely isochoric decomposition.

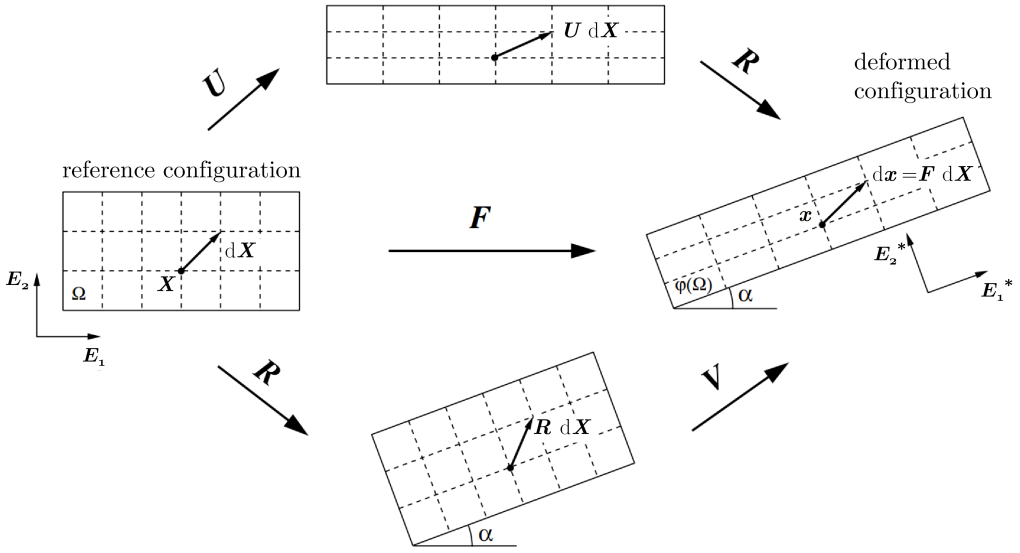

Figure 2.3: Representation of left and right polar decomposition of the deformation gradient. Adapted from Neto et al. (2011).

Polar Decomposition of the Deformation Gradient

The decomposition of the deformation gradient, $\boldsymbol{F}$, can also be made by a set of pure elongations and/or rotations. Considering a polar decomposition one obtains

$$\boldsymbol{F} = \boldsymbol{R}\boldsymbol{U} = \boldsymbol{V}\boldsymbol{R}, \tag{2.25}$$

where the symmetric positive tensors $\boldsymbol{U}$ and $\boldsymbol{V}$ are the right and the left stretch tensor, respectively. The orthogonal tensor, $\boldsymbol{R}$, is the local rotation tensor. The left and right stretch tensors can be related by means of the expression:

$$\boldsymbol{V} = \boldsymbol{R}\boldsymbol{U}\boldsymbol{R}^T \tag{2.26}$$

Attending to the image Figure 2.3 one can verify that applying the right polar decomposition, $\boldsymbol{F} = \boldsymbol{R}\boldsymbol{U}$, firstly the stretches are mapped by $\boldsymbol{U}$ and only then the rotation is applied, whereas in the left polar decomposition, $\boldsymbol{F} = \boldsymbol{V}\boldsymbol{R}$ the rotation is applied before the mapping of the stretches. Due to the fact that both stretch tensors, $\boldsymbol{U}$ and $\boldsymbol{V}$, are symmetric, they admit spectral decomposition resulting in:

$$\boldsymbol{U} = \sum_{i=1}^{3} \lambda_i \boldsymbol{l}_i \otimes \boldsymbol{l}_i, \tag{2.27a}$$

$$\boldsymbol{V} = \sum_{i=1}^{3} \lambda_i \boldsymbol{e}_i \otimes \boldsymbol{e}_i, \tag{2.27b}$$

where λ_i are the eigenvalues shared by both types of stretch tensors, which represent the

principal stretches. The eigenvectors $\boldsymbol{l}_i$ and $\boldsymbol{e}_i$ represent Lagrangian and Eulerian principal directions, that share the relation:

$$\boldsymbol{l}_i = \boldsymbol{R}\boldsymbol{e}_i. \tag{2.28}$$

The stretch tensors and be expressed as

$$\boldsymbol{U} = \sqrt{\boldsymbol{C}}, \tag{2.29a}$$
$$\boldsymbol{V} = \sqrt{\boldsymbol{B}}, \tag{2.29b}$$

being $\boldsymbol{C}$ and $\boldsymbol{B}$ the right and left Cauchy-Green strain tensors, respectively, and can be defined by:

$$\boldsymbol{C} = \boldsymbol{F}^T\boldsymbol{F}, \tag{2.30a}$$
$$\boldsymbol{B} = \boldsymbol{F}\boldsymbol{F}^T. \tag{2.30b}$$

2.1.3 Second Order Gradient Continuum Mechanics

In order to achieve a second-order homogenization computational scheme (which is going to be briefly introduced later), one must obtain the second order displacements gradient i.e. the gradient of the deformation gradient, since the first-order deformation gradient that has been presented in Section 2.1.2 doesn't take into consideration the absolute size of the continuum, making it impossible to address geometrical size effects. One can express the second order displacements gradient as

$$\mathbf{G} = \nabla_X \ \boldsymbol{F} = \nabla_X \left(\nabla_X \boldsymbol{u}\right) \Rightarrow G_{ijk} = \frac{\partial u_i}{\partial X_j \partial X_k}, \tag{2.31}$$

For further understanding of this concept one should read the aforementioned works, Kouznetsova (2002).

2.2 Strain Measures

Strain tensors are derived from the deformation gradient and aim to describe the deformation of a solid. Despite existing several alternatives to quantify the deformation that a solid can suffer, the process of selection of the tensor is based in a process of commitment between the phenomena that one pretends to model and its mathematical implementation.

The most used strain tensors are the *Lagrange* and *Euler* strain tensors, which are functions of the right and left stretch tensors, respectively. The Lagrange strain tensor can be expressed by

$$\boldsymbol{E}^{(m)} = \begin{cases} \frac{1}{m}(\boldsymbol{U}^m - \boldsymbol{I}) & , \ m \neq 0, \\ \ln[\boldsymbol{U}] & , \ m = 0, \end{cases} \tag{2.32}$$

being m a real number and $\ln[\cdot]$ the tensor logarithm of $[\cdot]$.

The Euler strain tensor comes as

$$\boldsymbol{\varepsilon}^{(m)} = \begin{cases} \frac{1}{m}(\boldsymbol{V}^m - \boldsymbol{I}) & , \ m \neq 0, \\ \ln[\boldsymbol{V}] & , \ m = 0, \end{cases} \tag{2.33}$$

where m is a real number and $\ln[\cdot]$ the tensor logarithm of $[\cdot]$.

Both types of tensor can be related due to the fact that tehey only differ from each other by a local rotation $\boldsymbol{R}$. The relation between the Lagrange and Euler strain tensors is defined by

$$\boldsymbol{\varepsilon}^{(m)} = \boldsymbol{R}\boldsymbol{E}^{(m)}\boldsymbol{R}^T. \tag{2.34}$$

The program utilized in the scope of this project takes into account finite strains and utilizes the logarithmic Eulerian strain tensor. This tensor is commonly known as *Hencky* strain tensor and it can be expressed as

$$\boldsymbol{\varepsilon} = \ln[\boldsymbol{V}] \equiv \ln[\sqrt{\boldsymbol{F}\boldsymbol{F}^T}]. \tag{2.35}$$

Considering infinitesimal deformations the definitions of both Lagrange and Euler strain tensors tend to the same tensor, which can be written as

$$\boldsymbol{\varepsilon} \approx \boldsymbol{\varepsilon}_{inf} \approx \nabla^s \boldsymbol{u} \approx \frac{1}{2}[\nabla \boldsymbol{u} + (\nabla \boldsymbol{u})^T] \tag{2.36}$$

2.3 Stress Measures

When a body is in a deformed state one can directly relate its deformation with the forces that are applied on it. The forces associated with the deformation of a body can be grouped in two different classes: body and surface forces (which contains the internal interactions of adjacent parts of the body). The body forces are present in the interior of the body and their units are force per unit of volume. Examples of this type of forces are the gravitational and magnetic forces. Surface forces have the units of force per unit of area and they result from the application of forces in the surface of the body. Internal forces occur due to the transmission of forces in the contact surfaces of the body.

The concept of stress is directly correlated to the quantification of the surface forces. In this section, the stress tensors that are utilized in this project will be introduced.

2.3.1 Cauchy Stress Tensor

The *Cauchy* stress tensor, $\boldsymbol{\sigma}$, is expressed by

$$\boldsymbol{t}(\boldsymbol{x}, \boldsymbol{n}) = \boldsymbol{\sigma}(\boldsymbol{x})\boldsymbol{n}, \tag{2.37}$$

being $\boldsymbol{t}$ the surface force and $\boldsymbol{n}$ its outward unit normal vector. The Cauchy stress tensor is often referenced in the literature as the true stress tensor because it refers to the deformed configuration. By establishing a balance of moments one can conclude that the Cauchy stress

tensor is symmetric which means that

$$\boldsymbol{\sigma} = \boldsymbol{\sigma}^T \tag{2.38}$$

Similarly to the decomposition of the deformation gradient in its isochoric and volumetric components, one can decompose the Cauchy stress tensor in its *Deviatoric* and *Hydrostatic* stresses. The decompostion of the Cauchy stress tensor comes as

$$\boldsymbol{\sigma} = \boldsymbol{s} + p\boldsymbol{I}, \tag{2.39}$$

where $\boldsymbol{s}$ is the deviatoric stress and p is the hydrostatic pressure or stress and it is expressed as

$$p = \frac{1}{3}\boldsymbol{\sigma}. \tag{2.40}$$

The deviatoric component is obtained by using the expression (2.39) resulting in

$$\boldsymbol{s} = \boldsymbol{\sigma} - p\boldsymbol{I}. \tag{2.41}$$

2.3.2 First Piola-Kirchhoff Stress Tensor

The *First Piola-Kirchhoff* stress tensor is related with the undeformed configuration of the body $\mathscr{B}$ and it can be related with the Cauchy stress tensor. Therefore, the first Piola-Kirchhoff stress tensor can be defined as the material version of the Cauchy stress tensor and it is expressed by

$$\boldsymbol{P} = J\boldsymbol{\sigma}\boldsymbol{F}^{-T}, \tag{2.42}$$

being J the determinant of the deformation gradient, $\boldsymbol{F}$. While the Cauchy stress tensor is symmetric, the first Piola-Kirchhoff stress tensor is, generaly, unsymmetric.

2.3.2.1 Kirchhoff Stress Tensor

By means of the utilization of the Cauchy stress tensor and the determinant of the deformation gradient, it is possible to define another symmetric stress tensor, the *Kirchhoff stress tensor*, being it defined by

$$\boldsymbol{\tau} = J\boldsymbol{\sigma} \tag{2.43}$$

2.4 Fundamental Conservation Principles

In the previous sections, only the variables that allows one to characterize the motion and deformation of a body as well as the relevant stress and strain measures were addressed. Although thermodynamic principles are outside the focus of this work, one must introduce some of them, as they must be always respected. In this section the principles of *Conservation of Mass* and the *Momentum Balance* are introduced due to the fact that these principles govern

the deformation of a solid. Other thermodinamic principles and laws such as the *Second Law of Thermodynamics* are not going to be introduced.

2.4.1 Conservation of Mass

The principle of the *conservation of mass* states that the following expression must be always respected:

$$\dot{\rho} + \rho \, \mathrm{div}_x \dot{\boldsymbol{u}} = 0 \tag{2.44}$$

being ρ the density of the solid and $\mathrm{div}(\bullet)$ the spatial divergence operator.

2.4.2 Momentum Balance

The momentum balance principle is defined by a set of partial differential equations utilising the *Cauchy Stress Tensor* which was introduced in the section Section 2.3.1. Taking into account the *spatial description* one can write the principle of momentum balance as:

$$\begin{cases} \mathrm{div}_x \, \boldsymbol{\sigma} + \boldsymbol{b} = \rho \ddot{\boldsymbol{u}} & , \text{in } \varphi(\Omega), \\ \boldsymbol{t} = \boldsymbol{\sigma} \boldsymbol{n} & , \text{on } \varphi(\partial\Omega), \end{cases} \tag{2.45}$$

being $\boldsymbol{b}$ the body forces in the deformed configuration per unit of deformed volume, $\boldsymbol{n}$ the unit outward normal vector to the deformed boundary of the body $\mathscr{B}$, $\boldsymbol{\varphi}(\partial\Omega)$ and $\boldsymbol{t}$ the traction vector field on $\boldsymbol{\varphi}(\partial\Omega)$.

The above momentum balance equations are written taking into account the deformed configuration of the solid, that is, the spatial description. However, one can write the same equations utilising the reference configuration of the body (material description). Thus one will utilise the first Piola-Kirchhoff stress tensor which was introduced in the section Section 2.3.2, resulting in

$$\begin{cases} \mathrm{div}_p \, \boldsymbol{P} + \bar{\boldsymbol{b}} = \bar{\rho} \, \ddot{\boldsymbol{u}} & , \text{in } \Omega, \\ \bar{\boldsymbol{t}} = \boldsymbol{P} \, \bar{\boldsymbol{n}} & , \text{on } \varphi(\partial\Omega), \end{cases} \tag{2.46}$$

where $\bar{\boldsymbol{b}}$ is named as the reference body force and it's measured per unit volume in the reference configuration resulting in

$$\bar{\boldsymbol{b}} = J \, \boldsymbol{b}, \tag{2.47}$$

and $\bar{\rho}$ it's the reference material density which is expressed as

$$\bar{\rho} = J \, \rho, \tag{2.48}$$

and $\bar{\boldsymbol{t}}$ expresses the traction field with normal outward unit vector, $\bar{\boldsymbol{n}}$, on the undeformed boundary. It is important to state that the expressions of the momentum balance principle are commonly known as the *strong equilibrium equations*.

2.5 Weak Equilibrium Equations

The strong equilibrium equations mentioned in the section are obtained by defining a set of governing equations or balance laws as it has been introduced in section Section 2.4. However, in order that the computational implementation of such principles can be made one must elaborate *Week Equilibrium Equations* due to the fact that the materialization of strong equilibrium equations in a numerical framework is quite arduous. The weak equilibrium equations are then going to be discretized and solved by the *Finite Element Method*. This section aims to provide the weak equilibrium equations recurring to the *Principle of Virtual Work*.

Taking into consideration a body $\mathscr{B}$ that occupies the region Ω that belongs to the euclidean space $\mathscr{E}$ with boundary defined as $\partial\Omega$ in its reference configuration that is subjected to body forces in its interior and surface tractions in its boundary. The deformed configuration can be obtained by applying the function that maps the deformation of the body φ. Furthermore, it is going to be considered a quasi-static deformation, thus inertia effects of the solid can be negleted.

2.5.1 Spatial Description

The spatial description claims that the body is in equilibrium if and only if the following equation is satisfied:

$$\int_{\varphi(\Omega)} [\boldsymbol{\sigma} : \nabla_x \boldsymbol{\eta} - \boldsymbol{b} \cdot \boldsymbol{\eta}] \, \mathrm{d}V - \int_{\varphi(\partial\Omega)} \boldsymbol{t} \cdot \boldsymbol{\eta} \, \mathrm{d}A = 0, \qquad \forall \boldsymbol{\eta} \in \mathscr{V}, \tag{2.49}$$

where $\boldsymbol{b}$ and $\boldsymbol{t}$ are the body forces per unit of deformed volume and boundary traction per unit of deformed area, respectively, and $\boldsymbol{\eta}$ is the admissible virtual displacement that belongs to the space of admissible virtual displacements, $\mathscr{V}$.

2.5.2 Material Description

The principle of virtual work can also be applied in the reference configuration of the body $\mathscr{B}$. Thus, the virtual work principle states that the body is in equilibrium if and only if its first Piola-Kirchhoff stress field, $\boldsymbol{P}$ fills the expression

$$\int_{\Omega} \left[\boldsymbol{P} : \nabla_X \boldsymbol{\eta} - \bar{\boldsymbol{b}} \cdot \boldsymbol{\eta}\right] \mathrm{d}V - \int_{\partial\Omega} \bar{\boldsymbol{t}} \cdot \boldsymbol{\eta} \, \mathrm{d}A = 0, \qquad \forall \boldsymbol{\eta} \in \mathscr{V}, \tag{2.50}$$

where where $\bar{\boldsymbol{b}}$ is named as the reference body force and it's measured per unit volume in the reference configuration, $\bar{\boldsymbol{t}}$ expresses the traction field with normal outward unit vector, $\bar{\boldsymbol{n}}$, on the undeformed boundary and $\boldsymbol{\eta}$ being the admissible virtual displacement belonging to the space of admissible virtual displacements, $\mathscr{V}$.

2.6 Finite Element Method

In Section 2.5 the weak equilibrium equations were presented. Those equations can, in some cases, have a high level of complexity. Thus, In order to obtain a solution for those equations, it is mandatory to resort to adequate numerical methods to solve them. The method that is most widely known and used is the *Finite Element Method*. Even though the solution obtained by this method is not perfect, it can be used provided that the error linked with the approximated solution is insignificant. In this condition, the approximated solution can be taken into consideration.

In order to use this method, the following steps must be applied:

1. Integral formulation of the problem;
2. Spatial domain discretization;
3. Temporal domain discretization;
4. Resolution of the system of equations that originates from the spatial and temporal domain discretizations. Usually the *Newton-Raphson* method is used.

In the following subsections the steps mentioned above are going to be addressed.

2.6.1 Integral Formulation of the Problem

The integral formulation of the problem, also known as weak formulation, can be obtained by applying one of several methods such as *Hamilton's Principle*, *Virtual Work Principle* - which was the method used in this work - etc. The integral formulation of the problem was presented in Section 2.5.1 - Equation (2.49) - and Section 2.5.2 - Equation (2.50) - for the spatial and material description, respectively.

2.6.2 Spatial Discretization

The spatial domain discretization is the cornerstone of the finite element method and it consists in the division of the continuum domain of the problem (Ω) in a set of finite sub-domains which are referred as finite elements. Thus, one can write the following expression:

$$\Omega \approx \Omega^d = \bigcup_{e=1}^{n_e} \Omega^e \tag{2.51}$$

where Ω^d is the discretized entity, n_e is the number of elements, Ω^e is the spatial domain of each finite element and $\bigcup$ refers to the union operation.

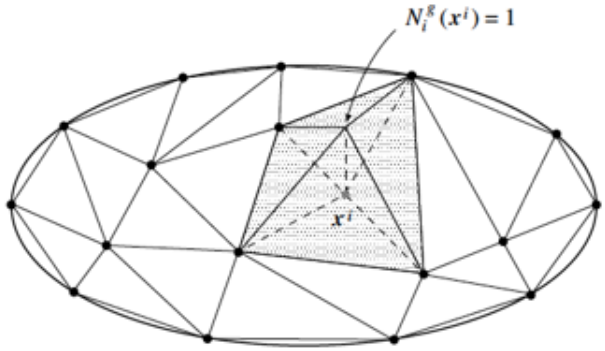

Figure 2.4: Finite element interpolation. The global shape function.

Interpolation of Variables

Once the domain of the problem is discretized, all variables of the each sub-domain are calculated by interpolation. Taking into consideration a generic vectorial field $\boldsymbol{a}(\boldsymbol{x})$ the referred interpolation process can be written as:

$$\boldsymbol{a}(\boldsymbol{x}) = \sum_{i=1}^{n_{nodes}} N_i^e(\boldsymbol{x})\ \boldsymbol{a}\{\boldsymbol{x_i}\}, \qquad \boldsymbol{x} \in \Omega^e, \tag{2.52}$$

being $\boldsymbol{a}\{\boldsymbol{x_i}\}$ the value of the vectorial field at the node number i. The function that is responsible for the interpolation is the term $N_i^e(\boldsymbol{x})$, also known as shape function, which is evaluated at the point of interest , $\boldsymbol{x}$.

The shape functions are different depending on the type of element that is going to be used. One particular characteristic that all shape functions share is the *Kronecker delta* characteristic, this is:

$$N_i^e(\boldsymbol{x_j}) = \delta_{ij}, \tag{2.53}$$

where δ_{ij} is the *Kronecker delta* function,

$$\begin{cases} \delta_{ij} = 1 & \text{, if } i = j, \\ \delta_{ij} = 0 & \text{, if } i \neq j. \end{cases} \tag{2.54}$$

This process can be also used for a discretized global domain, Ω^d:

$$\boldsymbol{a}(\boldsymbol{x}) = \sum_{i=1}^{n_{points}} N^g(\boldsymbol{x})\ \boldsymbol{a}\{\boldsymbol{x_i}\}, \qquad \boldsymbol{x} \in \Omega^d, \tag{2.55}$$

being the shape function $N^g(\boldsymbol{x})$ related, in this case, with the entire domain of the problem - while on the last case it was only related to the finite element domain. Usually, the shape functions can be represented by a matrix that is referred as the global interpolation matrix.

For a problem with n_{points}, the global interpolation matrix comes as:

$$N^g(\boldsymbol{x}) = \left[\text{ diag}\left[N_1(\boldsymbol{x})\right] \,\middle|\, \text{diag}[N_2(\boldsymbol{x})] \,\middle|\, \ldots \,\middle|\, \text{diag}[N_{n_p oints}(\boldsymbol{x})] \right], \tag{2.56}$$

where $\text{diag}\left[N_i(\boldsymbol{x})\right]$ denotes the $n_{\text{dof}} \times n_{\text{dof}}$ diagonal matrix, being n_{dof} the number of degrees of freedom of each point:

$$\text{diag}\left[N_i(\boldsymbol{x})\right] = \begin{bmatrix} N_i(\boldsymbol{x}) & 0 & \ldots & 0 \\ 0 & N_i(\boldsymbol{x}) & \ldots & 0 \\ \vdots & \vdots & \ddots & \vdots \\ 0 & 0 & \ldots & N_i(\boldsymbol{x}) \end{bmatrix}. \tag{2.57}$$

One can also "assemble" the nodal values in a global vector $\mathbf{u}^g$ resulting:

$$\mathbf{u}^g = \{u_1^1 \ , \ \ldots \ , \ u_{n_{\text{dof}}}^1 \ , \ \ldots \ , \ \ldots \ , \ u_1^{n_p} \ , \ \ldots \ , \ u_{n_{\text{dof}}}^{n_p}\}^T, \tag{2.58}$$

being the generic element u_i^j is the i-th component of the displacement vector of the global node j. Thus, the vectorial field in a point $\boldsymbol{x}$ can be expressed as:

$$\boldsymbol{u}\{\boldsymbol{x}\} = N(\boldsymbol{x}) \ \mathbf{u}^g. \tag{2.59}$$

The spatial discretization of the problem requires that two global discrete operators, being them the global discrete gradient operator, $\mathbf{G}^g$, and the global discrete symmetric gradient operator, $\mathbf{B}^g$. Both operators need to be established taking into account the conditions of the problem that needs to be solved, i.e. 2-dimensional or 3-dimensional fields, plane-stress or plane-strain, etc. For a 2-dimensional field and for a plane-strain problem the operators can be defined as:

$$\mathbf{B}^g = \left[\begin{array}{cc|cc|c|cc} \frac{\partial N_1}{\partial x} & 0 & \frac{\partial N_2}{\partial x} & 0 & \ldots & \frac{\partial N_{n_p}}{\partial x} & 0 \\ 0 & \frac{\partial N_1}{\partial y} & 0 & \frac{\partial N_2}{\partial y} & \ldots & 0 & \frac{\partial N_{n_p}}{\partial y} \\ \frac{\partial N_1}{\partial y} & \frac{\partial N_1}{\partial x} & \frac{\partial N_2}{\partial y} & \frac{\partial N_2}{\partial x} & \ldots & \frac{\partial N_{n_p}}{\partial y} & \frac{\partial N_{n_p}}{\partial x} \end{array}\right], \tag{2.60a}$$

$$\mathbf{G}^g = \left[\begin{array}{cc|cc|c|cc} \frac{\partial N_1}{\partial x} & 0 & \frac{\partial N_2}{\partial x} & 0 & \ldots & \frac{\partial N_{n_p}}{\partial x} & 0 \\ 0 & \frac{\partial N_1}{\partial x} & 0 & \frac{\partial N_2}{\partial x} & \ldots & 0 & \frac{\partial N_{n_p}}{\partial x} \\ \frac{\partial N_1}{\partial y} & 0 & \frac{\partial N_2}{\partial y} & 0 & \ldots & \frac{\partial N_{n_p}}{\partial y} & 0 \\ 0 & \frac{\partial N_1}{\partial y} & 0 & \frac{\partial N_2}{\partial y} & \ldots & 0 & \frac{\partial N_{n_p}}{\partial y} \end{array}\right]. \tag{2.60b}$$

Usually, $\mathbf{B}^g$ is referred as deformation matrix for cases where infinitesimal deformations occur.

Spatial Discretization of the Equilibrium Equations

By utilising the notation introduced in the last section, one can perform the spatial discretization of the virtual work expression that was introduced on Section 2.5.

Taking into account the spatial formulation presented in Equation (2.49) one can write its discretized counterpart by:

$$\left\{ \int_{\varphi(\Omega^d)} \left[(\mathbf{B}^g)^T \, \boldsymbol{\sigma} - N^T \, \mathbf{b} \right] \mathrm{d}V - \int_{\varphi(\partial\Omega^d)} N^T \, \mathbf{t} \, \mathrm{d}A \right\}^T \cdot \boldsymbol{\eta} = 0, \qquad \forall \boldsymbol{\eta} \in \mathscr{V}^d, \tag{2.61}$$

where $\mathscr{V}^d$ represents the discretized virtual displacement space and $\boldsymbol{\sigma}$ is the vector representation of the Cauchy stress tensor $\boldsymbol{\sigma}$.

For the material formulation presented in Equation (2.50) one can write its discretized counterpart as follows:

$$\left\{ \int_{\Omega^d} \left[(\mathbf{G}^g)^T \, \mathbf{P} - \mathbf{N}^T \, \bar{\mathbf{b}} \right] \mathrm{d}V - \int_{\partial\Omega^d} \mathbf{N}^T \, \bar{\mathbf{t}} \, \mathrm{d}A \right\}^T \cdot \boldsymbol{\eta} = 0, \qquad \forall \boldsymbol{\eta} \in \mathscr{V}^d, \tag{2.62}$$

in which $\mathbf{P}$ is the vector configuration of the first Piola-Kirchhoff stress tensor $\boldsymbol{P}$.

For the equations above to be valid they must be satisfied for all virtual displacements, η. Thus, the term within brackets must be null. Making some algebraic manipulation and some substitutions one can obtain an equation that consists in a balace of internal and external forces, this is:

$$\mathbf{f}^{\text{int}} - \mathbf{f}^{\text{ext}} = 0, \tag{2.63}$$

where $\mathbf{f}^{\text{int}}$ and $\mathbf{f}^{\text{ext}}$ are, respectively, the global internal and external force vectors, and in the spatial form are written as:

$$\mathbf{f}^{\text{int}} = \int_{\varphi(\Omega^d)} (\mathbf{B}^g)^T \, \boldsymbol{\sigma} \, \mathrm{d}V, \tag{2.64a}$$

$$\mathbf{f}^{\text{ext}} = \int_{\varphi(\Omega^d)} \mathbf{N}^T \, \mathbf{b} \, \mathrm{d}A + \int_{\varphi(\partial\Omega^d)} \mathbf{N}^T \, \mathbf{t} \, \mathrm{d}A. \tag{2.64b}$$

In the computational framework of the finite element method, these force vectors are analysed element by element, and are obtained by integration over its domain,

$$\mathbf{f}_e^{\text{int}} = \int_{\varphi(\Omega^e)} (\mathbf{B}^e)^T \, \boldsymbol{\sigma} \, \mathrm{d}V, \tag{2.65a}$$

$$\mathbf{f}_e^{\text{ext}} = \int_{\varphi(\Omega^e)} (\mathbf{N}^e)^T \, \mathbf{b} \, \mathrm{d}A + \int_{\varphi(\partial\Omega^e)} (\mathbf{N}^e)^T \, \mathbf{t} \, \mathrm{d}A, \tag{2.65b}$$

in the deformed configuration. In the material formulation the force vectors are given by:

$$\mathbf{f}_e^{\text{int}} = \int_{\Omega^e} (\mathbf{G}^e)^T \, \mathbf{P} \, \mathrm{d}V, \tag{2.66a}$$

$$\mathbf{f}_e^{\text{ext}} = \int_{\Omega^e} (\mathbf{N}^e)^T \, \mathbf{b} \, \mathrm{d}A + \int_{\partial\Omega^e} (\mathbf{N}^e)^T \, \mathbf{t} \, \mathrm{d}A. \tag{2.66b}$$

Then, the element force vectors are assembled in the corresponding global force vector,

$$\mathbf{f}^{\text{int}} = \mathop{\mathsf{A}}_{e=1}^{n_e} \mathbf{f}_e^{\text{int}}, \tag{2.67a}$$

$$\mathbf{f}^{\text{ext}} = \mathop{\mathsf{A}}_{e=1}^{n_e} \mathbf{f}_e^{\text{ext}}, \tag{2.67b}$$

being A an assembly operator.

Gaussian Quadrature

In the last subsection it was stated that the element force vectors are obtained by solving the respective integral. This process is made by recurring to a numerical method, being the Gaussian Quadrature one of the most utilised methods. The use of this method is facilitated by converting the coordinates of the finite elements into a set of parametric coordinates $\boldsymbol{\zeta}$. The transofrmation of coordinates is made by the Jacobian matrix:

$$\mathbf{J} = \frac{\partial \boldsymbol{x}}{\partial \boldsymbol{\zeta}}. \tag{2.68}$$

The Gaussian quadrature method can be written as:

$$\int_{\Omega} \boldsymbol{a}\{\boldsymbol{x}\} \, \mathrm{d}V = \int_{-1}^{1} \boldsymbol{a}\{\boldsymbol{\zeta}\} \, \det(\mathbf{J}) \, \mathrm{d}\boldsymbol{\zeta} \equiv \sum_{i=1}^{\text{nGP}} \boldsymbol{a}\{\boldsymbol{\zeta}_i\} \, W_i \, \det(\mathbf{J}_i), \tag{2.69}$$

being $\boldsymbol{\zeta}_i$ the position of the i-th Gauss point and W_i the correspondent Gauss point weight. The number of Gauss points has to be chosen taking into account the degree n and for an exact numerical solution one should use at least, the number of Gauss points (nGP) that respect the following expression:

$$n = 2 \times \text{nGP} - 1. \tag{2.70}$$

It is important to note that, when emplying the Gaussian quadrature, the variables are obtained in each Gauss point, i.e. the constitutive law is analysed in each Gauss point.

2.6.3 Time Discretization

In a general way, materials usually present a behaviour that depends on the deformation history i.e. the deformation rate and/or the deformation path. To solve this kind of problems utilising the finite element method one must implement an incremental strategy in which the time is also discretized resulting in the division of the time interval $[t_0, t]$ in $n+1$ sub-intervals where in each one of them the equilibrium equations must be verified.

In order to include the deformation history in the constitutive models that characterize the stress tensor, one must utilise an internal variable, $\boldsymbol{\theta}$, to store the information of the previous increments.

This results in obtaining the stress response at the increment $n+1$ while taking into consideration the new deformation state and the previous internal variables, $\boldsymbol{\theta}_n$. Thus, one can write:

$$\boldsymbol{\sigma}_{n+1} = \hat{\boldsymbol{\sigma}}\{\boldsymbol{F}_{n+1}, \boldsymbol{\theta}_n\}, \tag{2.71a}$$

$$\boldsymbol{P}_{n+1} = \hat{\boldsymbol{P}}\{\boldsymbol{F}_{n+1}, \boldsymbol{\theta}_n\}, \tag{2.71b}$$

being the relations above expressed for the spatial and material formulations, respectively and $\hat{\boldsymbol{\sigma}}\{\boldsymbol{F}_{n+1}, \boldsymbol{\theta}_n\}$ and $\hat{\boldsymbol{P}}\{\boldsymbol{F}_{n+1}, \boldsymbol{\theta}_n\}$, the incremental constitutive functional for each configuration.

For infinitesimal deformations the ongoing deformation is obtained by the infinitesimal strain tensor, which has been presented in Equation (2.36) resulting in:

$$\boldsymbol{\sigma}_{n+1} = \hat{\boldsymbol{\sigma}}\{\boldsymbol{\varepsilon}_{n+1}, \boldsymbol{\theta}_n\}. \tag{2.72}$$

Taking the weak spatial equilibrium equation, Equation (2.49), one can define the quasi-static incremental boundary value problem as:

Given a set of internal variables, $\boldsymbol{\theta}$, and the displacement field at time t_n and knowing the forces $\boldsymbol{b}_{n+1}$ and $\boldsymbol{t}_{n+1}$ find the displacement field $\boldsymbol{u}_{n+1}$ such that:

$$\int_{\varphi(\Omega)} [\hat{\boldsymbol{\sigma}}\{\boldsymbol{F}_{n+1}, \boldsymbol{\theta}_n\} : \nabla_x \boldsymbol{\eta} - \boldsymbol{b} \cdot \boldsymbol{\eta}] \, \mathrm{d}V - \int_{\varphi(\partial\Omega)} \boldsymbol{t} \cdot \boldsymbol{\eta} \, \mathrm{d}A = 0, \qquad \forall \boldsymbol{\eta} \in \mathscr{V}. \tag{2.73}$$

2.6.4 Incremental Finite Element Solution

After discretizing the equation present above, Equation (2.73), it can be expressed as:

$$\mathbf{r}\{\mathbf{u}_{n+1}\} = \mathbf{f}^{\text{int}}\{\mathbf{u}_{n+1}\} - \mathbf{f}^{\text{ext}}_{n+1} \tag{2.74}$$

where, for each increment, the unknown variable is the nodal vector displacement, $\boldsymbol{u}_{n+1}$ that leads to the residual, $\mathbf{r}$, being null or very small. For each increment the external forces and

internal ones can be expressed as:

$$\mathbf{f}_{e_{n+1}}^{\text{int}} = \int_{\varphi(\Omega^e)} (\mathbf{B}^e)^T \, \hat{\boldsymbol{\sigma}}\{\boldsymbol{F}_{n+1}, \boldsymbol{\theta}_n\} \, \mathrm{d}V, \tag{2.75a}$$

$$\mathbf{f}_{e_{n+1}}^{\text{ext}} = \int_{\varphi(\Omega^e)} (\mathbf{N}^e)^T \; \mathbf{b}_{n+1} \, \mathrm{d}A + \int_{\varphi(\partial\Omega^e)} (\mathbf{N}^e)^T \; \mathbf{t}_{n+1} \, \mathrm{d}A. \tag{2.75b}$$

Due to the fact that the material can have a non-linear behaviour and/or a non-linear geometry, Equation (2.74) is non-linear. Thus, for such equation can be solved in a computational way, one must rely on an efficient method. One of the most popular methods to achieve the numerical solution is the *Newton-Raphson* method. One of its desirable characteristics is that this method has a quadratic rate of asymptotic convergence which leads to achieve a solution in a faster way.

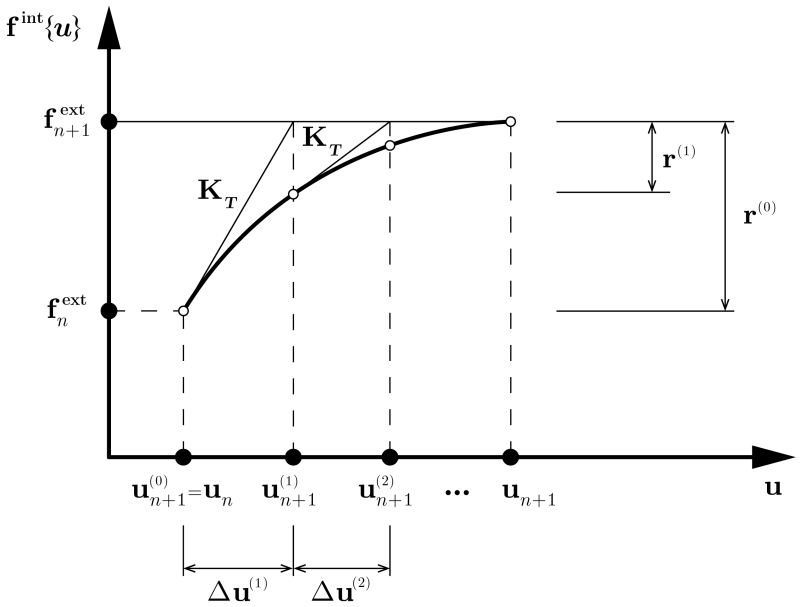

Figure 2.5: The Newton-Raphson algorithm for the incremental finite element solution. Adapted from Neto et al. (2011)..

A typical iteration, j of this method can be resumed as:

1. The global tangent stiffness matrix $\mathbf{K}_T$ is obtained as:

$$\mathbf{K}_T^{(j-1)} = \left.\frac{\partial \mathbf{r}}{\partial \mathbf{u}_{n+1}}\right|_{\mathbf{u}_{n+1}^{(j-1)}} = \mathop{\mathsf{A}}_{e=1}^{n_e} \int_{\varphi(\Omega^e)} (\mathbf{B}^e)^T \mathbf{D} \mathbf{B}^e \, \mathrm{d}V, \tag{2.76}$$

where $\mathbf{D}$ is the matrix representation of the spatial tangent modulus,

$$\mathbf{D} = \frac{\partial \boldsymbol{\sigma}}{\partial \boldsymbol{F}}. \tag{2.77}$$

2. $\Delta\mathbf{u}^{(j)}$ is obtained in each iteration (j) of the Newton-Raphson method through the resolution of the linearised version of the equilibrium equation:

$$\mathbf{K}_T^{(j-1)}\Delta\mathbf{u}^{(j)} = \mathbf{r}\{\mathbf{u}_{n+1}^{(j-1)}\}. \tag{2.78}$$

3. For each increment $n+1$, the guess for the value of the displacement fields is assumed to be the last converged value, $\mathbf{u}_{n+1}^{(0)} = \mathbf{u}_n$, and within each iteration (j) it is updated as:

$$\mathbf{u}_{n+1}^{(j)} = \mathbf{u}_{n+1}^{(j-1)} + \Delta\mathbf{u}^{(j)}, \tag{2.79}$$

4. The residual vector is updated by:

$$\mathbf{r}\{\mathbf{u}_{n+1}^{(j-1)}\} = \mathbf{f}^{\text{int}}\{\mathbf{u}_{n+1}^{(j-1)}\} - \mathbf{f}_{n+1}^{\text{ext}} \tag{2.80}$$

5. This iterative process occurs until a convergence criterion is satisfied i.e. $\dfrac{\| \mathbf{r} \|}{\| \mathbf{f}^{\text{ext}} \|} <$ tol. If the criterion isn't verified a new iteration will occur, startin again in the step (i).

Chapter 3

Fundamentals of Multi-Scale Models

On the previous section the fundamentals of continuum mechanics and of the finite element method were introduced. It has been already stated that, in continuum mechanics one considers that a certain body can be characterized as a set of particles on which the material is assumed to be homogeneous. However, the behaviour and the properties of any material are directly related to its microstructure, being this dependence even more severe when the material is subdue to harsh requests where the singularities and heterogeneities of the microstructure have an important role in the material's response. Therefore, when a high level of precision is required in terms of the material's response the macroscopic models that rely on continuum mechanics can present some limitations once that they cannot replicate the microstructural behaviour.

Aiming to incorporate the microstructural behaviour in the material's global response some models and different approaches have been developed. One of this methods is the *Coupled Multi-Scale Method*. This method has its key feature in the simultaneously analysis of two scales. Therefore, the macro-scale problem is said to be coupled with the micro-scale one, which is related to the material's microstructure.

In this approach it is utilised a RVE (Representative Volume Element) that aims to define the micro-scale of the problem as it must contain enough information about the microstructure of the material. This method relies on applying the macroscopic deformation gradient, which comes from the macro-scale properties (geometry, loading, etc.), to a RVE and to solve a micro-scale equilibrium problem resulting in a microscopic stress field which is later homogenized resulting in a macroscopic stress tensor. In this method one assigns a RVE to each integration point of the macroscopic finite element mesh in order to solve the micro-scale problem. Thus, this method is referred as Coupled Multi-Scale analysis.

In this chapter Multi-Scale models are going to be described, namely one will introduce the concept of RVE, the principle of separation of scales, the numerical homogenization method (first-order computational scheme and a brief description of the second-order one) and the classic boundary conditions. The finite element implementation that leads to obtaining the solution of the micro-scale problem is also going to be briefly discussed. In this chapter the

topics discussed above are going to be introduced having into account the work of Neto and Feijoo (2006) and Kouznetsova (2002).

3.1 Representative Volume Element

The concept of a *Representative Volume Element* (RVE) was introduced by Hill (1963) with the aim to characterize the microstructure of a material by means of a representative sub-region. In the macroscopic domain, the RVE is said to be associated with a macro point and it is said that it only represents the microstructure in a proper way if it is statistically representative i.e. the RVE must have such a size that includes the biggest number of heterogeneities that represent the material's microstructure. In Figure 3.1 it is represented a RVE with voids which domain is represented by Ω_ν^v and boundary $\partial\Omega_\nu^v$ as well as inclusions which domain is represented by Ω_ν^i and boundary $\partial\Omega_\nu^i$.

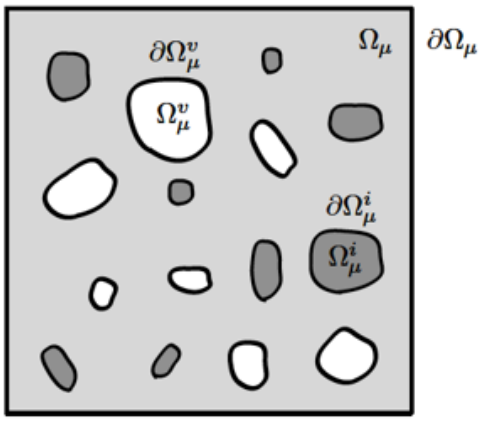

Figure 3.1: Representative volume element scheme. Adapted from Carvalho (2015).

.

In multi-scale models, where the constitutive model of the material is influenced by two different scales, the RVE's characteristic length is an important parameter. Thus, the RVE's characteristic length, L_{RVE} must be much bigger than the characteristic length of the heterogeneities, L_{het}, and must be much smaller than the macroscopic domain characteristic length, L_{macro}, this is:

$$L_{\text{het}} \ll L_{\text{RVE}} \ll L_{\text{macro}}. \tag{3.1}$$

Equation (3.1) is known as the *Principle of Separation of Scales* and it has been introduced by Hashin (1983).

As the main focus of this work is to determine the characteristic length that breaks this principle and its influence in the results that are obtained. It is important to state that in a first-order computational scheme the characteristic length of the RVE does not have influence on the results obtained at the micro-scale, while in a second-order one the RVE's characteristic length

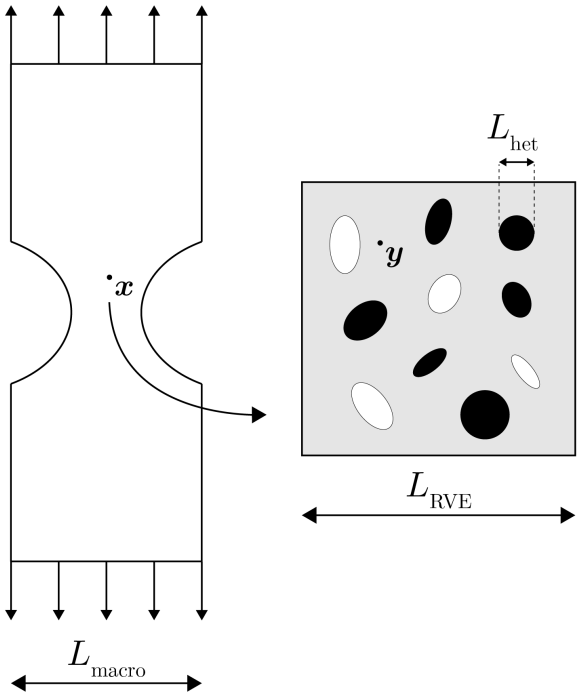

Figure 3.2: Macro and microscales and respective sizes. Adapted from Neto and Feijoo (2006).

is expected to influence the results that are going to be obtained. In terms of mathematical description, both the first-order computational scheme and the second-order one are going to be introduced. For a more detailed study about the second-order homogenization one should read the aforementioned reference, Kouznetsova (2002).

It is also important to note that while the normally used constitutive laws may not be able to reproduce the macroscopic behaviour of a material that has a complex microstructure, they can be used to predict the micro-scale behaviour as it is considered that each microstructural constituent behaves as a continuum matter at the micro-scale.

3.2 Scale Transition Theory

As stated before, the RVE's characteristic length must be much bigger than the characteristic length of the heterogeneities and much smaller than the macrosctructure size so taht the homogenization of the stress and strain fields can be made.

In the following sections the notation that is going to be used if briefly explained. In the previous chapter, $\boldsymbol{x}$ and $\boldsymbol{X}$ were used to characterize an infinitesimal point of the macro-scale in the deformed and undeformed configuration, respectively. So, in this chapter one will use $\boldsymbol{y}$ and $\boldsymbol{Y}$ to characterize an infinitesimal point of the micro-scale in its deformed and undeformed configuration, respectively.

3.2.1 Numerical Homogenization

The homogenization process is one of the base concepts of the multi-scale models as it allows the determination of the macroscopic fields through the volumetric average of the correspondent microscopic ones. Taking into consideration a generic tensorial field at the micro-scale, $\boldsymbol{A}\{\boldsymbol{y}\}$, one can express its correspondent homogenized tensor at the macro-scale as:

$$\boldsymbol{A}\{\boldsymbol{x}\} = \frac{1}{V_\mu} \int_{\Omega_\mu} \boldsymbol{A}\{\boldsymbol{y}\} \, \mathrm{d}V, \tag{3.2}$$

where Ω_μ is the undeformed domain of the RVE and V_μ is its volume on the reference configuration.

3.3 Microscale Equilibrium Problem

The procedure to solve microscale equilibrium problem is going to be presented in the following subsections by the following order:

1. Determination of the microscopic deformation gradient;
2. Definition of the admissible microscopic displacement field;
3. Description of the RVE equilibrium;
4. Presentation of the *Hill-Mandel* principle;
5. Homogenization of the first Piola-Kirchhoff stress tensor.

So, one can state that, by solving the microscale equilibrium problem, one will obtain the microscale stress field which is then going to be homogenized. This problem will be present edtaking into account the *large strain* theory, being the deformation gradient, $\boldsymbol{F}$, utilized to express the prescribed strains and once that the homogenization method is utilised taking into account the undeformed configuration, one will obtain the first Piola-Kirchhoff after the homogenization process is made.

3.3.1 Microscopic Deformation Gradient

Considering a finite strain formulation, the RVE's deformation is prescribed by the deformation gradient. Thus, the macroscopic deformation gradient for a general point, $\boldsymbol{x}$, at a general time instant t, is going to be equal to the homogenized microscopic deformation gradient, this is:

$$\boldsymbol{F}\{\boldsymbol{x}, t\} = \frac{1}{V_\mu} \int_{\Omega_\mu} \boldsymbol{F}\{\boldsymbol{y}, t\} \, \mathrm{d}V, \tag{3.3}$$

where the microscopic deformation gradient, $\boldsymbol{F}\{\boldsymbol{y}, t\}$, can be expressed as,

$$\boldsymbol{F}\{\boldsymbol{y}, t\} = \boldsymbol{I} + \nabla_X \, \boldsymbol{u}\{\boldsymbol{y}, t\}, \tag{3.4}$$

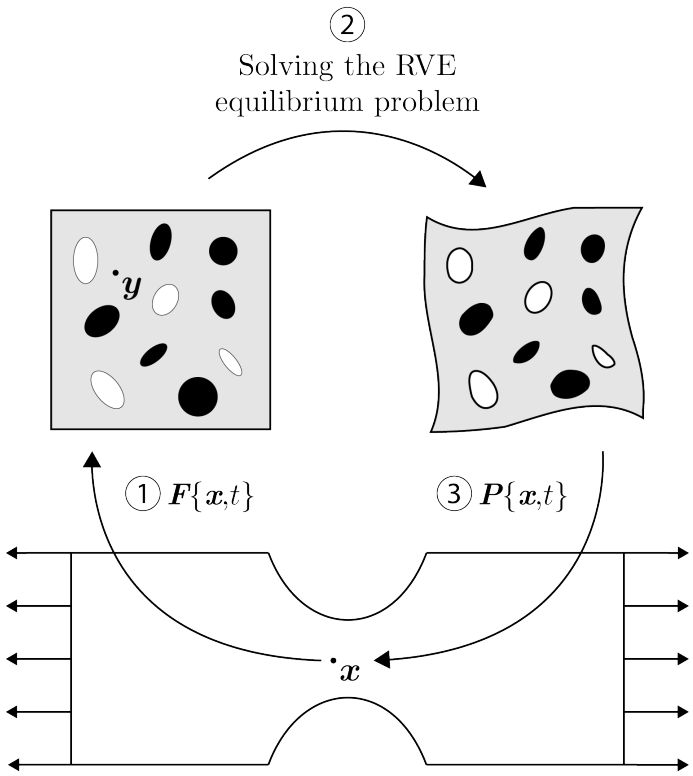

Figure 3.3: Representation of the stages to solve a multi-scale problem. Adapted from Neto and Feijoo (2006).

where ∇_X is the gradient operator in material description. As a result, Equation (3.3) can be rewritten as:

$$\boldsymbol{F}\{\boldsymbol{x},t\} = \boldsymbol{I} + \frac{1}{V_\mu}\int_{\Omega_\mu} \nabla_X \ \boldsymbol{u}\{\boldsymbol{y},t\}\ \mathrm{d}V. \tag{3.5}$$

The application of a deformation gradient to the RVE results in a microscopic displacement field, $\boldsymbol{u}\{\boldsymbol{y},t\}$, which can be expressed as the sum of its linear part with the displacement fluctuation field, resulting in

$$\boldsymbol{u}\{\boldsymbol{y},t\} = (\boldsymbol{F}\{\boldsymbol{x},t\} - \boldsymbol{I})\,\boldsymbol{Y} + \tilde{\boldsymbol{u}}\{\boldsymbol{y},t\}, \tag{3.6}$$

being that the linear part of the microscopic displacement field, $(\boldsymbol{F}\{\boldsymbol{x},t\}-\boldsymbol{I})\boldsymbol{Y}$, is dependent on the applied deformation gradient and the displacement fluctuation field, $\tilde{\boldsymbol{u}}\{\boldsymbol{y},t\}$, the unknown variable of the microscopic equilibrium problem.

Thus, one can rewrite the microscopic deformation gradient in terms of its macroscopic

correspondent deformation gradient and the displacement fluctuation field, resulting in:

$$\begin{aligned}\boldsymbol{F}\{\boldsymbol{y},t\} &= \boldsymbol{I} + \nabla_X\ \boldsymbol{u}\{\boldsymbol{y},t\} \\ &= \boldsymbol{I} + \nabla_X\ \left[(\boldsymbol{F}\{\boldsymbol{x},t\} - \boldsymbol{I})\,\boldsymbol{Y} + \tilde{\boldsymbol{u}}\{\boldsymbol{y},t\}\right] \\ &= \boldsymbol{F}\{\boldsymbol{x},t\} + \nabla_X\ \tilde{\boldsymbol{u}}\{\boldsymbol{y},t\}.\end{aligned} \tag{3.7}$$

3.3.2 Admissible Microscopic Displacement Field

Taking into account the expression of the macroscopic deformation gradient, Equation (3.3) and the expression of the microscopic displacement field, Equation (3.6), one can write:

$$\boldsymbol{F}\{\boldsymbol{x},t\} = \boldsymbol{F}\{\boldsymbol{x},t\} + \frac{1}{V_\mu}\int_{\Omega_\mu} \nabla_X\ \tilde{\boldsymbol{u}}\{\boldsymbol{y},t\}\ \mathrm{d}V. \tag{3.8}$$

Applying the Gauss theorem one can rewrite Equation (3.8) as:

$$\int_{\Omega_\mu} \nabla_X\ \tilde{\boldsymbol{u}}\{\boldsymbol{y},t\}\ \mathrm{d}V = \int_{\partial\Omega_\mu} \tilde{\boldsymbol{u}}\{\boldsymbol{y},t\} \otimes \boldsymbol{N}\{\boldsymbol{Y}\}\ \mathrm{d}A = \boldsymbol{0}, \tag{3.9}$$

which defines the *minimal kinematical admissible constraint*, which defines the space of the admissible displacement fluctuation,

$$\tilde{\mathscr{K}} \equiv \left\{ \tilde{\boldsymbol{u}},\ \text{sufficiently regular} \mid \int_{\partial\Omega_\mu} \tilde{\boldsymbol{u}}\{\boldsymbol{y},t\} \otimes \boldsymbol{N}\{\boldsymbol{Y}\}\ \mathrm{d}A = \boldsymbol{0} \right\}, \tag{3.10}$$

where $\boldsymbol{N}\{\boldsymbol{Y}\}$ is the outward unit vector normal to the boundary of the undeformed configuration of the RVE, $\partial\Omega_\mu$.

3.3.3 RVE Equilibrium

As it has already been stated, at the micro-scale one can consider that each microstructural constituent behaves as a continuum medium, thus, the theory of *Continuum Mechanics* that has been presented in Chapter 2 can be applied at the at the micro-scale model to solve the equilibrium problem.

Despite that the homogenization of the stress field is made taking into account the material description, the equilibrium problem is solved considering the spatial description being the strong form of the equilibrium equations for the RVE expressed as:

$$\begin{cases} \mathrm{div}_x\ \boldsymbol{\sigma}\{\boldsymbol{y},t\} + \boldsymbol{b}_\mu\{\boldsymbol{y},t\} = \boldsymbol{0} & ,\text{in } \varphi(\Omega_\mu), \\ \boldsymbol{t}_\mu\{\boldsymbol{y},t\} = \boldsymbol{\sigma}\{\boldsymbol{y},t\}\ \boldsymbol{n}\{\boldsymbol{y}\} & ,\text{on } \varphi(\partial\Omega_\mu), \end{cases} \tag{3.11}$$

where $\boldsymbol{b}_\mu\{\boldsymbol{y},t\}$ represents the volume forces in the deformed configuration of the RVE, $\boldsymbol{t}_\mu\{\boldsymbol{y},t\}$ the applied boundary traction vector field and $\boldsymbol{n}\{\boldsymbol{y}\}$ is the outward unit vector normal to the deformed boundary of the RVE, $\varphi(\partial\Omega_\mu)$.

The microscopic equilibrium problem, to be solved, needs to be presented in its weak form as the solution is obtained by means of the *Finite Element Method*. Applying the *Virtual Work Principle* to Equation (3.11) one can write:

$$\int_{\varphi(\Omega_\mu)} [\boldsymbol{\sigma}\{\boldsymbol{y},t\} : \nabla_x \tilde{\boldsymbol{\eta}} - \boldsymbol{b}_\mu\{\boldsymbol{y},t\} \cdot \tilde{\boldsymbol{\eta}}] \, \mathrm{d}V - \int_{\varphi(\partial\Omega_\mu)} \boldsymbol{t}_\mu\{\boldsymbol{y},t\} \cdot \tilde{\boldsymbol{\eta}} \, \mathrm{d}A = 0, \qquad \forall \tilde{\boldsymbol{\eta}} \in \mathscr{V}. \tag{3.12}$$

3.3.4 Hill-Mandel Principle

Hill-Mandel's principle allows one to establish the connection between the two scales having as its basis an energetic balance. It states that the macroscopic stress power needs to be equal to the average of its micro-scale counterpart. Taking into account a material formulation, one can write the Hill-Mandel principle as:

$$\boldsymbol{P}\{\boldsymbol{x},t\} : \dot{\boldsymbol{F}}\{\boldsymbol{x},t\} = \frac{1}{V_\mu} \int_{\Omega_\mu} \boldsymbol{P}\{\boldsymbol{y},t\} : \dot{\boldsymbol{F}}\{\boldsymbol{y},t\} \, \mathrm{d}V. \tag{3.13}$$

where $\dot{\boldsymbol{F}}\{\cdot\}$ is the time derivative of the deformation gradient. The time derivative of the microscopic deformation gradient can be written by taking into consideration Equation (3.7), resulting in:

$$\dot{\boldsymbol{F}}\{\boldsymbol{y},t\} = \dot{\boldsymbol{F}}\{\boldsymbol{x},t\} + \nabla_X \, \dot{\tilde{\boldsymbol{u}}}\{\boldsymbol{y},t\}. \tag{3.14}$$

Combining Equation (3.13) with Equation (3.14) one can rewrite the Hill-Mandel principle as:

$$\int_{\Omega_\mu} \boldsymbol{P}\{\boldsymbol{y},t\} : \nabla_X \, \dot{\tilde{\boldsymbol{u}}}\{\boldsymbol{y},t\} \, \mathrm{d}V = 0. \tag{3.15}$$

Taking into account the hypothesis that $\dot{\tilde{\boldsymbol{u}}} \in \mathscr{V}$ and the material version of the Expression (3.12), it results that:

$$\int_{\Omega_\mu} \bar{\boldsymbol{b}}_\mu\{\boldsymbol{y},t\} \cdot \tilde{\boldsymbol{\eta}} \, \mathrm{d}V = 0, \qquad \forall \tilde{\boldsymbol{\eta}} \in \mathscr{V}, \tag{3.16}$$

$$\int_{\partial\Omega_\mu} \bar{\boldsymbol{t}}_\mu\{\boldsymbol{y},t\} \cdot \tilde{\boldsymbol{\eta}} \, \mathrm{d}A = 0, \qquad \forall \tilde{\boldsymbol{\eta}} \in \mathscr{V}. \tag{3.17}$$

Analysing the expressions presented above, one can conclude that the body and traction forces are reactive forces related to the kinematical constraints applied to the displacement fluctuation field on the RVE. This statements allow one to simplify the equilibrium equation, resulting in, for the material configuration:

$$\int_{\Omega_\mu} \boldsymbol{P}\{\boldsymbol{y},t\} : \nabla_X \tilde{\boldsymbol{\eta}} \, \mathrm{d}V = 0, \qquad \forall \tilde{\boldsymbol{\eta}} \in \mathscr{V}, \tag{3.18}$$

or, for the spatial configuration,

$$\int_{\varphi(\Omega_\mu)} \boldsymbol{\sigma}\{\boldsymbol{y},t\} : \nabla_x \tilde{\boldsymbol{\eta}} \, \mathrm{d}V = 0, \qquad \forall \tilde{\boldsymbol{\eta}} \in \mathscr{V}. \tag{3.19}$$

3.3.5 Homogenized Stress Tensor

The homogenized first Piola-Kirchhoff stress tensor, $\boldsymbol{P}\{\boldsymbol{x},t\}$, is written as:

$$\begin{aligned}\boldsymbol{P}\{\boldsymbol{x},t\} &= \frac{1}{V_\mu}\int_{\Omega_\mu} \boldsymbol{P}\{\boldsymbol{y},t\}\ \mathrm{d}V \\ &= \frac{1}{V_\mu}\int_{\partial\Omega_\mu} \bar{\boldsymbol{t}}_\mu\{\boldsymbol{y},t\}\otimes\boldsymbol{Y}\mathrm{d}A - \frac{1}{V_\mu}\int_{\Omega_\mu}\bar{\boldsymbol{b}}_\mu\{\boldsymbol{y},t\}\otimes\boldsymbol{Y}\mathrm{d}V\end{aligned} \tag{3.20}$$

3.4 Admissible Kinematical Boundary Conditions

It has been mentioned in Section 3.3.1, that the unknown variable in a microscopic equilibrium problem is the displacement fluctuation field $\tilde{\boldsymbol{u}}\{\boldsymbol{y},t\}$.

In order to solve the equilibrium equations, and therefore to obtain the value of the displacement fluctuation field, one needs to set the admissible kinematical boundary conditions. The effects that the boundary conditions have on the results are of great importance, hence one needs to choose the boundary condition that suits better for the type of problem that is to be studied so that it can replicate the real behaviour of the solid.

In order to characterize the different boundary conditions one must bear in mind that they must respect the kinematical restraints, presented in Equation (3.9), and the Hill-Mandel principle, presented in Equation (3.15). Commonly in the literature there are a different set of boundary conditions that can be named as:

1. The Taylor Hypothesis;
2. Linear Boundary Condition;
3. Periodic Boundary Condition;
4. Uniform Traction Boundary Condition.

On the following sections, the different kinds of boundary conditions are going to be introduced.

3.4.1 The Taylor Hypothesis

The Taylor Hypothesis the the simplest type of boundary condition states that the microscopic displacement field is a linear function of $\boldsymbol{Y}$, resulting in:

$$\boldsymbol{u}\{\boldsymbol{y},t\} = (\boldsymbol{F}\{\boldsymbol{x},t\} - \boldsymbol{I})\,\boldsymbol{Y}, \tag{3.21}$$

implying that the displacement fluctuation field is null,

$$\tilde{\boldsymbol{u}}\{\boldsymbol{y},t\} = \boldsymbol{0}, \tag{3.22}$$

and, as a consequence, the microscopic deformation gradient is equivalent to its correspondent macroscopic deformation gradient,

$$\boldsymbol{F}\{\boldsymbol{y},t\} \equiv \boldsymbol{F}\{\boldsymbol{x},t\}. \tag{3.23}$$

It is the most restrictive boundary condition, which results to an overestimation of the stiffness of heterogeneous materials.

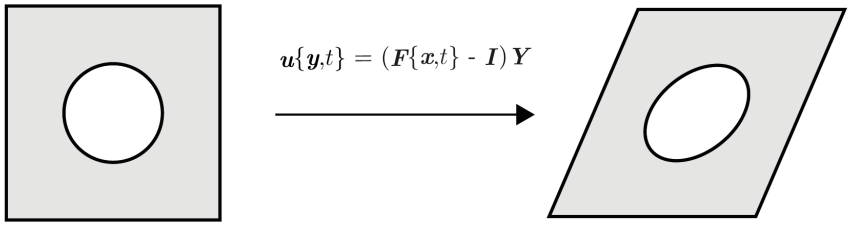

Figure 3.4: Representation of the Taylor Hypothesis boundary condition. Adapted from Neto and Feijoo (2006).

3.4.2 Linear Boundary Condition

The Linear Boundary condition states that the displacement field on the RVE's boundaries are linear in $\boldsymbol{Y}$, this is:

$$\boldsymbol{u}\{\boldsymbol{y},t\} = (\boldsymbol{F}\{\boldsymbol{x},t\} - \boldsymbol{I})\,\boldsymbol{Y}, \tag{3.24}$$

resulting in the fact that the displacements fluctuation field is null at the boundary of the RVE,

$$\tilde{\boldsymbol{u}}\{\boldsymbol{y},t\} = \boldsymbol{0}, \qquad \forall \boldsymbol{y} \in \partial\Omega_\mu. \tag{3.25}$$

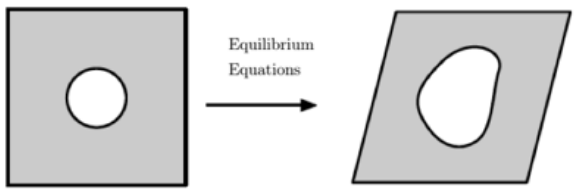

Figure 3.5: Representation of the linear boundary condition. Adapted from Neto and Feijoo (2006).

The expression presented above satisfies both Expressions (3.9) and (3.17). However, the Expression (3.16) is only verified in the absence of body forces and accelerations.

3.4.3 Periodic Boundary Condition

The Periodic Boundary Condition is one of the most used by the scientific community since has an excellent ability to reproduce the behaviour of materials that present a periodic microstructure, this is, the microstructure would be seen as a periodic repeated pattern of the RVE. Although the microstructure is said to be periodic, the heterogeneities of the RVE are not required to be periodic.

Once that the microstructure is seen as a periodic pattern of the RVE, the displacements of opposing boundary sides must be consistent.

This condition establishes that the boundary that limits the RVE can be divided in a set of positive and negative parts, this is, $\partial\Omega_\mu^+$ and $\partial\Omega_\mu^-$, respectively, such that:

$$\partial\Omega_\mu = \partial\Omega_\mu^+ \cup \partial\Omega_\mu^-. \tag{3.26}$$

One must also consider the outward unit vectors $\boldsymbol{n}^+$ and $\boldsymbol{n}^-$, normal to $\partial\Omega_\mu^+$, and to $\partial\Omega_\mu^-$, respectively, and that both present the following relation:

$$\boldsymbol{n}^- = -\boldsymbol{n}^+. \tag{3.27}$$

Taking the information presented above, one can state that this condition presents a periodic fluctuation field and an anti-periodic traction field that can be expressed as:

$$\tilde{\boldsymbol{u}}\{\boldsymbol{y}^+, t\} = \tilde{\boldsymbol{u}}\{\boldsymbol{y}^-, t\}, \tag{3.28}$$

$$\bar{\boldsymbol{t}}_\mu\{\boldsymbol{y}^+, t\} = -\bar{\boldsymbol{t}}_\mu\{\boldsymbol{y}^-, t\}, \tag{3.29}$$

where $\boldsymbol{y}^+ \in \partial\Omega_\mu^+$ and $\boldsymbol{y}^- \in \partial\Omega_\mu^-$, correspond to similar points in opposite sides of the RVE.

In the same way that the *Linear* boundary condition, this condition satisfies both Equations (3.9) and (3.17), but Equation (3.16) is only verified in the absence of body forces and accelerations.

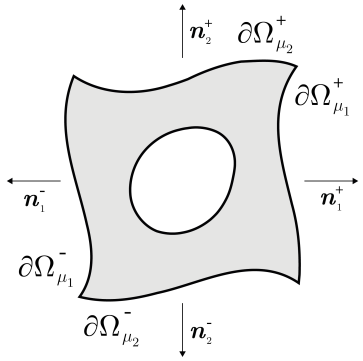

Figure 3.6: Boundaries of the RVE in the *Periodic* boundary condition. Adapted from Neto and Feijoo (2006).

3.4.4 Uniform Traction Boundary Condition

The Uniform Traction Boundary Condition only reproduces the *minimal kinematical admissible constraint* which is expressed by Equation (3.9) in Section 3.3.2:

$$\int_{\partial\Omega_\mu} \tilde{\boldsymbol{u}}\{\boldsymbol{y},t\} \otimes \boldsymbol{N}\{\boldsymbol{Y}\}\, \mathrm{d}A = \boldsymbol{0}, \tag{3.30}$$

leading into an uniform traction field on the RVE's boundaries. Once again, the Hill-Mandel principle that is associated with body forces, Equation (3.16), is only satisfied if the body forces are absent. Furthermore, taking into account the Hill-Mandel principle one it is able to prove that the traction on the RVE border is uniform and equal to:

$$\boldsymbol{P}\{\boldsymbol{y},t\}\boldsymbol{N}\{\boldsymbol{y},t\} = \boldsymbol{P}\{\boldsymbol{x},t\}\boldsymbol{N}\{\boldsymbol{x},t\}, \tag{3.31}$$

according to Neto and Feijoo (2006).

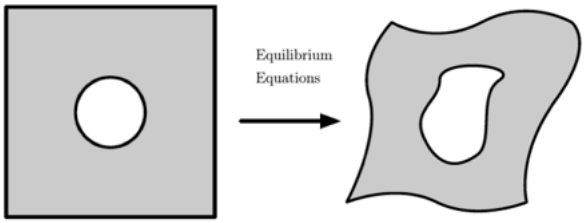

Figure 3.7: Representation of the linear boundary condition. Adapted from Neto and Feijoo (2006).

3.4.5 Remarks on the Different Boundary Conditions

The boundary conditions that have been presented in the last sections, can be ordered by their "level" of constraint to the solid. Hence, starting from the least constraint to the most constraint one, results the following order which starts with the *Uniform Traction* boundary condition, followed by the *Periodic* boundary condition and finally the *Linear* boundary condition and the *Taylor Hypothesis*. It is of great importance to state that, from this boundary conditions, the one that is most used is the *Periodic* boundary condition, since some authors claim that it is the condition that converges faster to the theoretical solution i.e. for the same RVE characteristic length, the *Periodic* boundary condition results in a solution that is closest to the effective value.

It is also important to note that, for the *Uniform Traction* boundary condition, since it is the least constraint since it is based on the *minimal kinematical admissible constraint*, when large deformations are applied to the RVE, the results that are obtained with this boundary

condition can be unrealistic since it can occur spurious effects as reported by Coenen et al. (2012).

3.5 Second-Order Homogenisation

The second-order homogenisation requires both the deformation gradient as well as of its gradient. This is, for such computational model can be obtained one needs the second-order displacements gradient, which can be expressed as:

$$\mathbf{G} = \nabla_X \ \boldsymbol{F} = \nabla_X \left(\nabla_X \boldsymbol{u}\right) \Rightarrow G_{ijk} = \frac{\partial u_i}{\partial X_j \partial X_k}, \tag{3.32}$$

3.5.1 Micro-Scale Kinematics

According to Kouznetsova (2002), considering a second-order homogenisation both the first-order deformation gradient and the second-order one are applied to the RVE leading to a displacement field $\boldsymbol{u}\{\boldsymbol{y}, t\}$ which can be expressed as a sum of its linear, quadratic and a displacement fluctuation field, respectively, resulting in:

$$\boldsymbol{u}\{\boldsymbol{y}, t\} = (\boldsymbol{F}(\boldsymbol{x}, t) - \boldsymbol{I})\boldsymbol{Y} + \frac{1}{2}\mathbf{G} : (\boldsymbol{Y} \otimes \boldsymbol{Y}) + \tilde{\boldsymbol{u}}. \tag{3.33}$$

Without loss of generality it is conveniently deemed that the origin of the micro-scale coordinate system is located at the geometric center of the RVE, resulting in:

$$\int_{\Omega_Y} \boldsymbol{Y} d\Omega_y = \mathbf{0}. \tag{3.34}$$

3.5.2 Periodic Boundary Condition

Kouznetsova (2002) states that the minimum admissible constraint can be expressed as:

$$\int_{\partial\Omega_Y} \left(\boldsymbol{N} \otimes \tilde{\boldsymbol{u}} \otimes \boldsymbol{Y} + \boldsymbol{Y} \otimes \tilde{\boldsymbol{u}} \otimes \boldsymbol{N}\right) dA = \mathbf{0}. \tag{3.35}$$

Kouznetsova (2002) also particularises this constraint for the case of generalised periodicity, arriving to

$$\int_{\partial\Omega_Y^i} \tilde{\boldsymbol{u}} dA = \mathbf{0}, \quad \text{for each RVE surface } i. \tag{3.36}$$

The minimal constraint, expressed by Equation (3.35) can be particularized for the case when periodic fluctuations are imposed on the RVE boundary, this is, $\tilde{\boldsymbol{u}}^+ = \tilde{\boldsymbol{u}}^-$.

3.6 LINKS Program

The program that was used in the scope of this thesis is a program called LINKS (Large Strain Implicit Non-Linear Finite Element Analysis of Solids Linking Scales) that has been developed

by the group CM2S (Computational Multi-Scale Modeling of Solids and Structures) which is led by Professor Francisco Pires, Phd. As the scope of this thesis is not a numerical implementation of the multi-scale theory the functioning principle of the program will not be addressed. This program deals with large strain formulation. For further understanding about the functioning of the program one should read Ferreira (2017).

3.7 Direct Numerical Simulation

Direct Numerical Simulation (DNS) consists in modelling the microstructure of a material explicitly in the macro-scale. The problem is then solved taking into consideration only the macro-scale, thus, the problem is solved by the conventional finite element method. The disadvantage of this type of models is that they can be very heavy at computational levels, requiring a lot of computational power, being this one of the reasons for the current interest in developing multi-scale models since they provide results in a faster and less heavy in terms of computational effort. For further details on this topic one should read the aforementioned references Bishop et al. (2015).

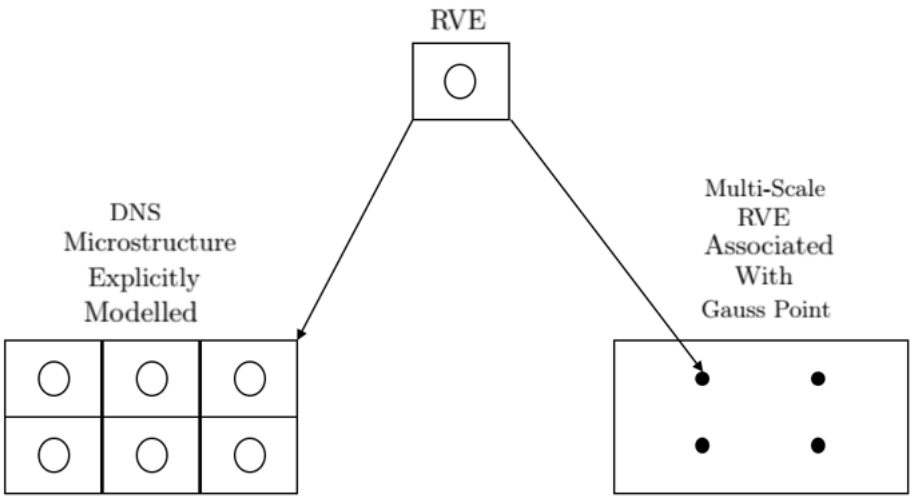

Figure 3.8: Differences between a DNS and multi-scale simulation.

Chapter 4

Assessment of the Principle of Separation of Scales of Specimens Under a Tensile Solicitation

As it has been stated in Chapter 3, the principle of separation of scales (PSS), Equation (3.1), depends mainly on the characteristic size of the RVE. However there may exist some cases, where the PSS can be violated depending on the type of solicitation that is applied to a generic solid (i.e. the PSS can also be related with the type and magnitude of the deformation gradient).Thus, this chapter aims to assess this principle in cases where a tensile solicitation is prescribed. One will analyse the PSS in two different types of micro-structures, being one a RVE with a central circular void and the other a RVE with a central elastic inclusion. Furthermore, one will analyse two different types of specimens, being one of them a specimen with a 4 mm notch and the other a 12 mm notch. This study aims to evaluate the PSS in cases where a higher and a lower stress concentration factor K_c takes place. The PSS will be analysed by comparing the solutions obtained by the DNS models and the coupled multi-scale ones.

Firstly, the case of the RVE with a circular void is presented, being described the geometry of the specimens that have been studied, the multi-scale model utilised (macro and micro-scale geometries and material), the DNS model that was utilised and the numerical simulations that were made as well as the results that were obtained. Lastly, some conclusions are withdrawn taking into account the results that have been obtained. The study mentioned above is identical for the 4 and 12 mm notch models.

For the case of the RVE with an elastic inclusion the same procedure is undertaken.

4.1 Traction Solicitation Utilising a RVE with a Circular Void

In this section one will assess the PSS where the micro-structure is represented by a RVE with a circular void.

4.1.1 Specimens' Characterization

The specimens that have been utilised in this study can be seen bellow as follows.

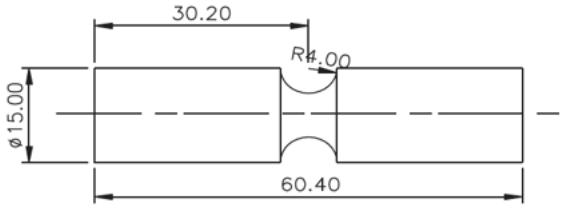

(a) The 4 mm notch specimen.

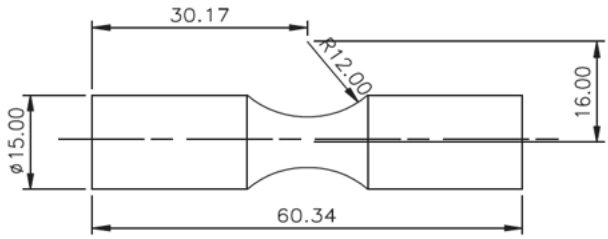

(b) The 12 mm notch specimen.

Figure 4.1: Specimens that were studied.

4.1.2 Material Definition

The material that was utilised was an aluminium alloy, commonly referred as 2024-T351 modelled with the Von Mises model. The selection of this material was made due to the fact that there are several experimental studies that have been made with this type of alloy. The elastic properties of this material were considered as in the studies made by Teng (2008):

Table 4.1: Elastic properties of the aluminium alloy 2024-T351.

Young Modulus	E	72.4 GPa
Poisson's Ratio	ν	0.3
Yield Stress	σ_y	352 MPa

Besides the elastic properties it is also required to know the material's hardening law. The calibrated hardening law of the aluminium alloy 2024-T531 can be seen in Figure 4.2.

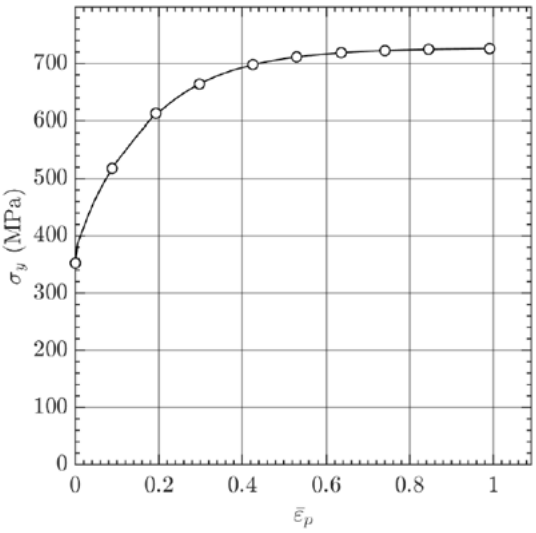

Figure 4.2: Calibrated hardening law for the aluminium alloy 2024-T351. Adapted from Ferreira (2017).

4.1.3 Multi-Scale (MS) Models

The multi-scale model can be divided into two distinct models. The macro-scale model and the micro-scale one. The multi-scale models that have been used are presented below.

4.1.3.1 Macro-Scale Meshes

The macro-scale meshes were obtained by means of pre-processing software, GiD®. The type of elements that were utilised were a 8-noded quadratic element with reduced integration. The macro-scale meshes can be found in Figure 4.3.

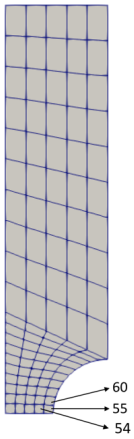

(a) The 4 mm notch specimen macro-scale mesh.

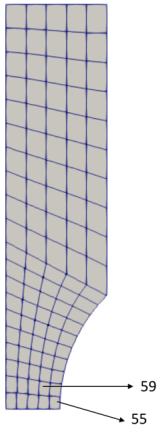

(b) The 12 mm notch specimen macro-scale mesh.

Figure 4.3: Macro-scales meshes of the specimens that have been studied. The highlighted elements were the ones utilised later for analysis.

A resume of the mesh properties can be found below in the following tables. It is important to note that the macro-scale mesh is independent of the micro-scale one, this is, the macro-scale meshes that were utilised were the same for all different kinds of RVEs.

Table 4.2: Macro-scale mesh properties for the 4 mm notch specimen.

Number of Elements	Number of Nodes
100	351

Table 4.3: Macro-scale mesh properties for the 12 mm notch specimen.

Number of Elements	Number of Nodes
100	351

4.1.3.2 Micro-Scale Mesh: Definition of the RVEs' Properties

Before presenting the micro-scale mesh, one must define some RVE's properties, namely its characteristic length, or, in this case, lengths and its void volume fraction, or damage ratio. In a general way, one can express the void volume fraction (f) as the ratio between the volume of the void (V_{void}) and the volume of solid part (V_{solid}). Hence, one can write:

$$\mathrm{f} = \frac{V_{void}}{V_{solid}}. \tag{4.1}$$

Taking into account a square configuration for the RVE and a circular configuration for the void one can rewrite the previous equation in order to solve the radius of the void (r_{void}) that

produces certain a void volume fraction (VVF), resulting in:

$$r_{void} = \sqrt{\frac{\text{f RVE}_L^2}{\pi}}, \tag{4.2}$$

being RVE_L the RVE's characteristic length.

In this report three different RVEs have been studied, being the only difference between them, their characteristic length. The RVEs that have been studied have 0.5, 1 and 2 millimetres of characteristic length. The mesh is equal for all types of RVEs and, in a logical way, the micro-scale mesh is equal for the 4 and 12 millimetres notch specimens. The micro-scale mesh is shown as follows:

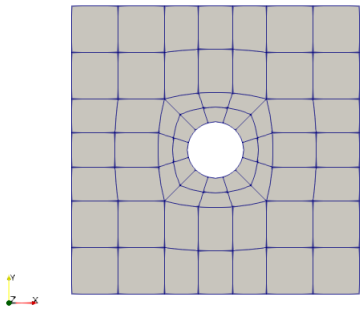

Figure 4.4: Micro-scale mesh of the specimens that have been sutdied.

The RVE's material is also the macro-scale material, this is, the aluminium alloy 2024-T351, presented in Section 4.1.2. The element type that was utilised was a 8-noded quadratic element. A resume of the mesh properties can be found in the table below.

Table 4.4: Micro-scale mesh properties.

Number of Elements	Number of Nodes
64	232

4.1.4 DNS Models

Having introduced the specimens geometry and the micro-scale mesh it is now possible to define the DNS models that have been utilised. As it has already been stated in the introductory chapters of the present report, a DNS simulation requires an explicitly modelation of the microsctructure of the material. The models that are going to be presented were made with the aid of the software GiD® and are presented below, for the 4 and 12 mm notch specimens, respectively. The highlighted RVEs are the ones that were compared with results from the coupled multi-scale models.

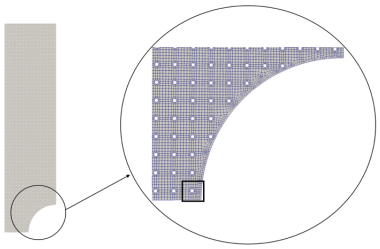

(a) Close up of the notch zone of the DNS model of the 4 mm notch specimen using a RVE_L =0.5 mm.

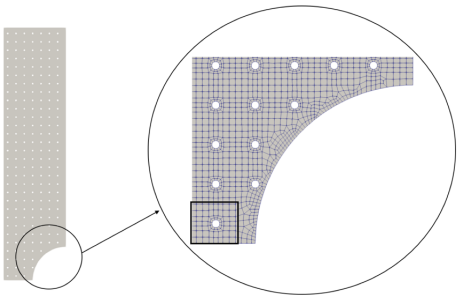

(b) Close up of the notch zone of the DNS model of the 4 mm notch specimen using a RVE_L =1 mm.

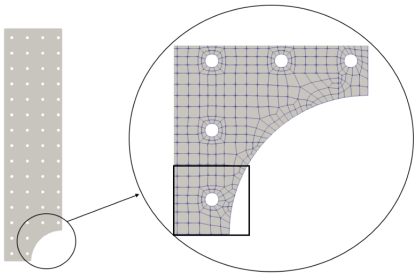

(c) Close up of the notch zone of the DNS model of the 4 mm notch specimen using a RVE_L =2 mm.

Figure 4.5: Close up of the notch zone of the different DNS models for the 4 mm notch specimen with a circular void.

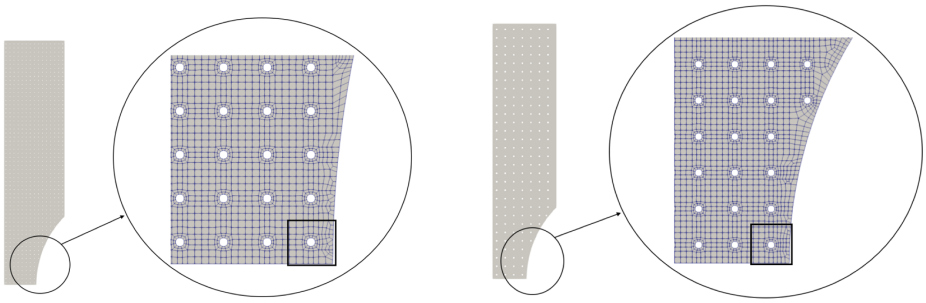

(a) Close up of the notch zone of the DNS model of the 12 mm notch specimen using a RVE_L =0.5 mm.

(b) Close up of the notch zone of the DNS model of the 12 mm notch specimen using a RVE_L =1 mm.

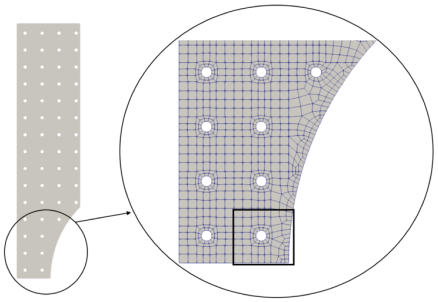

(c) Close up of the notch zone of the DNS model of the 12 mm notch specimen using a RVE_L =2 mm.

Figure 4.6: Close up of the notch zone of the different DNS models for the 12 mm notch specimen with a circular void.

A resume of the DNS mesh properties can be found below on the following tables.

Table 4.5: DNS meshes properties for the 4 mm notch specimen with a circular void.

RVE_L	Number of Elements	Number of Nodes
0.5	54875	175024
1	13546	43365
2	3516	11469

Table 4.6: DNS meshes properties for the 12 mm notch specimen with a circular void.

RVE_L	Number of Elements	Number of Nodes
0.5	52831	168524
1	12751	40897
2	3429	11195

4.1.5 Numerical Simulations

Having already defined the properties of the multi-scale models as of the DNS ones, one can define the numerical simulations parameters. For every numerical simulation, it was prescribed a nodal displacement of 2 mm in the top nodes of the macro-scale meshes as well as of the DNS ones. The prescribed displacement was divided in 20 increments. The boundary conditions that were applied at the macro-scale were only the symmetry boundary conditions. For the coupled multi-scale, the simulations were repeated for each micro-scale boundary condition (linear, periodic and uniform traction). All simulations were made considering a plane-strain case. All elements that were utilised are a 8-noded quadratic element and 4 GP for integration purposes.

4.1.6 Results Obtained

In the following section, the results that were obtained are going to be presented and then discussed. The presentation of the results is going to be made by separating the two scales, this is:

- Firstly, the results that are going to be compared are the results obtained at the macro-scale, this is, the reaction forces depending on the prescribed displacement. Thus, those curves are going to be presented taking into account the results provided by DNS model and the FE^2 ones (for each boundary condition) and for each RVE characteristic length;
- At the micro-scale one will present the Cauchy effective stress and the equivalent strain fields in the same conditions as above. It is important to note that this comparison has to be made in a qualitative way, once that it is cumbersome to directly relate a RVE in the DNS model to a RVE associated with a Gauss point in the FE^2 model.
- The results' analyses will be made until a representative displacement, this is, the displacement that occurred until the point where some elements became too deformed. For the 4 mm notch the representative displacement is of 0.2 mm and for the 12 mm notch it is of 0.5 mm. For the results at the macro-scale, the representative displacements are demonstrated by a vertical red line.

The results obtained as well as the comparison between them are demonstrated in the following sections for the 4 and 12 mm notch specimens.

Before demonstrating the results that were obtained, it is important to define the RVE's that were analysed. For the DNS models, the RVE that was considered can be found highlighted in Figure 4.5 for the 4 mm notch specimen and in Figure 4.6 for the 12 mm notch specimen.

For the multi-scale models, each RVE is associated to a Gauss point making that the choosing process has to be made by establishing the same criteria for all RVEs. As it is impossible to correspond the RVEs in the MS models to the RVEs presented in the DNS ones, the criteria that was established is that the RVE chosen at the MS models was the RVE which coordinates would be closer to the centroid of the RVE at the homologous DNS simulation. The elements

that were considered for this analysis can be found in Figure 4.3. For the 4 mm and 12 mm notch, respectively, the Gauss points that were considered are stated as follows, the first GP of the element number 51, the third GP of the element number 54, the second GP of the element number 60, the first and third Gauss points of the element number 55 and the first GP of the element number 59, each set of three Gauss points is for the cases of RVE_L =0.5, 1 and 2 mm, respectively.

4.1.6.1 4 mm Notch

RVE with a characteristic length of 0.5 mm

The results obtained at the macro-scale, the reaction forces, can be found bellow as follows.

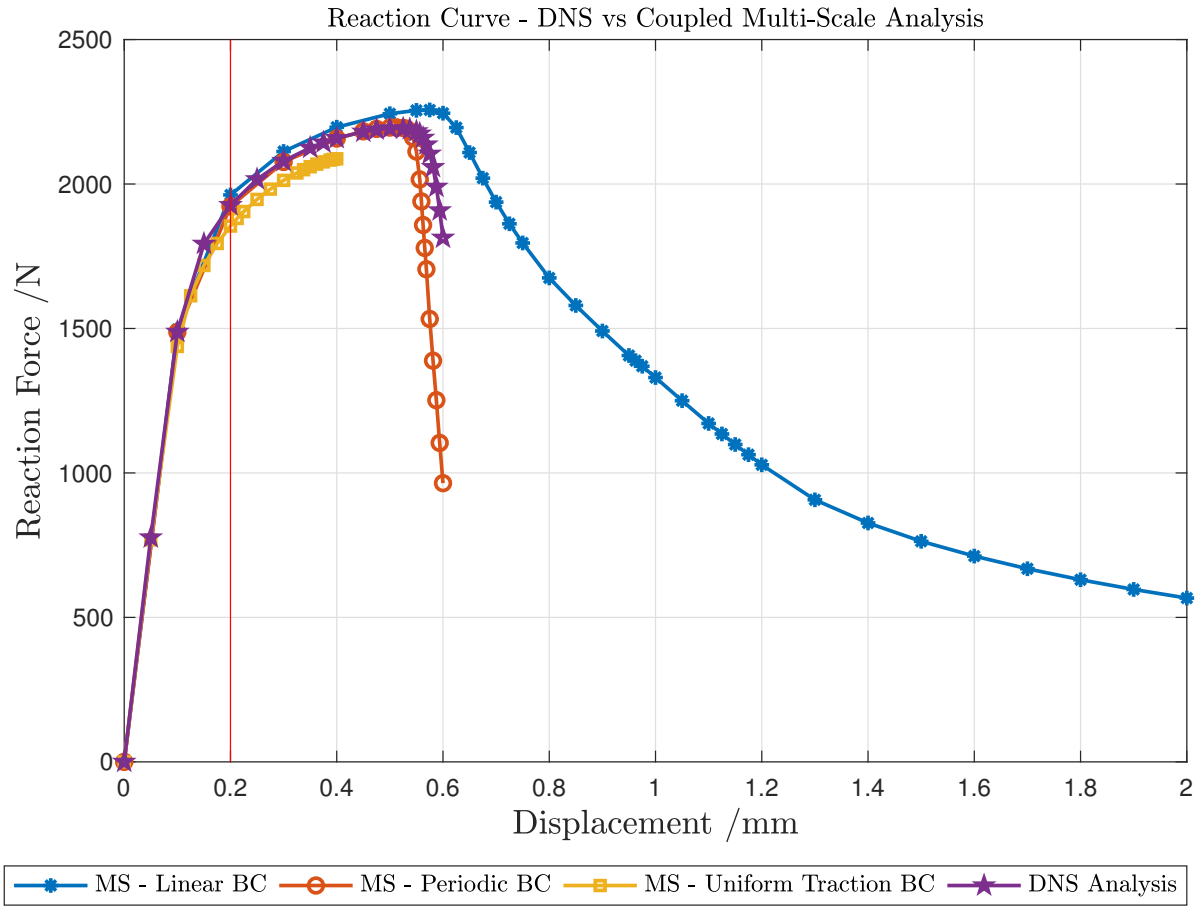

Figure 4.7: Reaction forces for the models with a RVE with a characteristic length of 0.5 mm with a circular void.

Having already defined the RVEs that were considered, the results that were obtained at the micro-scale can be found in the next figures in terms of the effective Cauchy stress and equivalent strain, respectively.

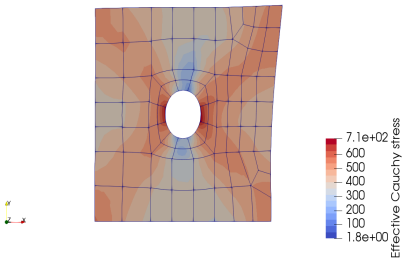

(a) Effective Cauchy stress field for the DNS model utilising a RVE_L =0.5 mm.

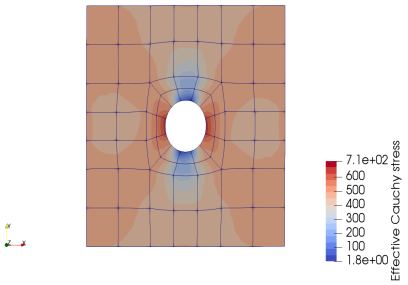

(b) Effective Cauchy stress field for the MS model utilising a RVE_L =0.5 mm considering a linear boundary condition at the micro-scale.

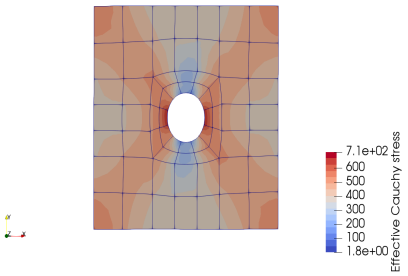

(c) Effective Cauchy stress field for the MS model utilising a RVE_L =0.5 mm considering a periodic boundary condition at the micro-scale.

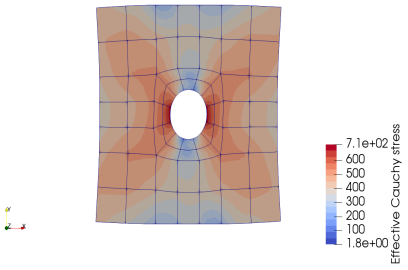

(d) Effective Cauchy stress field for the MS model utilising a RVE_L =0.5 mm considering a uniform traction boundary condition at the micro-scale.

Figure 4.8: Effective Cauchy stress field for the 4 mm notch specimen for a RVE_L =0.5 mm with a circular void.

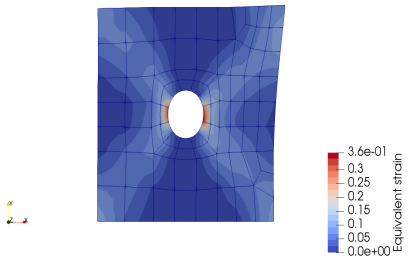

(a) Equivalent strain field for the DNS model utilising a RVE_L =0.5 mm.

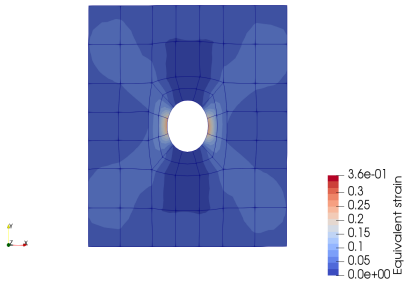

(b) Equivalent strain field for the MS model utilising a RVE_L =0.5 mm considering a linear boundary condition at the micro-scale.

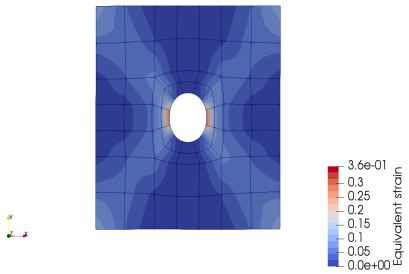

(c) Equivalent strain field for the MS model utilising a RVE_L =0.5 mm considering a periodic boundary condition at the micro-scale.

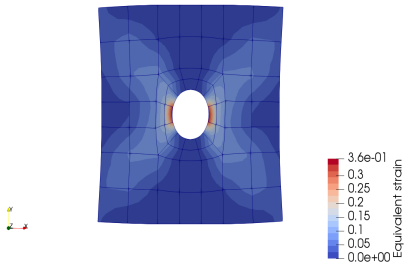

(d) Equivalent strain field for the MS model utilising a RVE_L =0.5 mm considering a uniform traction boundary condition at the micro-scale.

Figure 4.9: Equivalent strain field for the 4 mm notch specimen for a RVE_L =0.5 mm with a circular void.

RVE with a characteristic length of 1 mm

The results obtained at the macro-scale, the reaction forces, can be found bellow as follows.

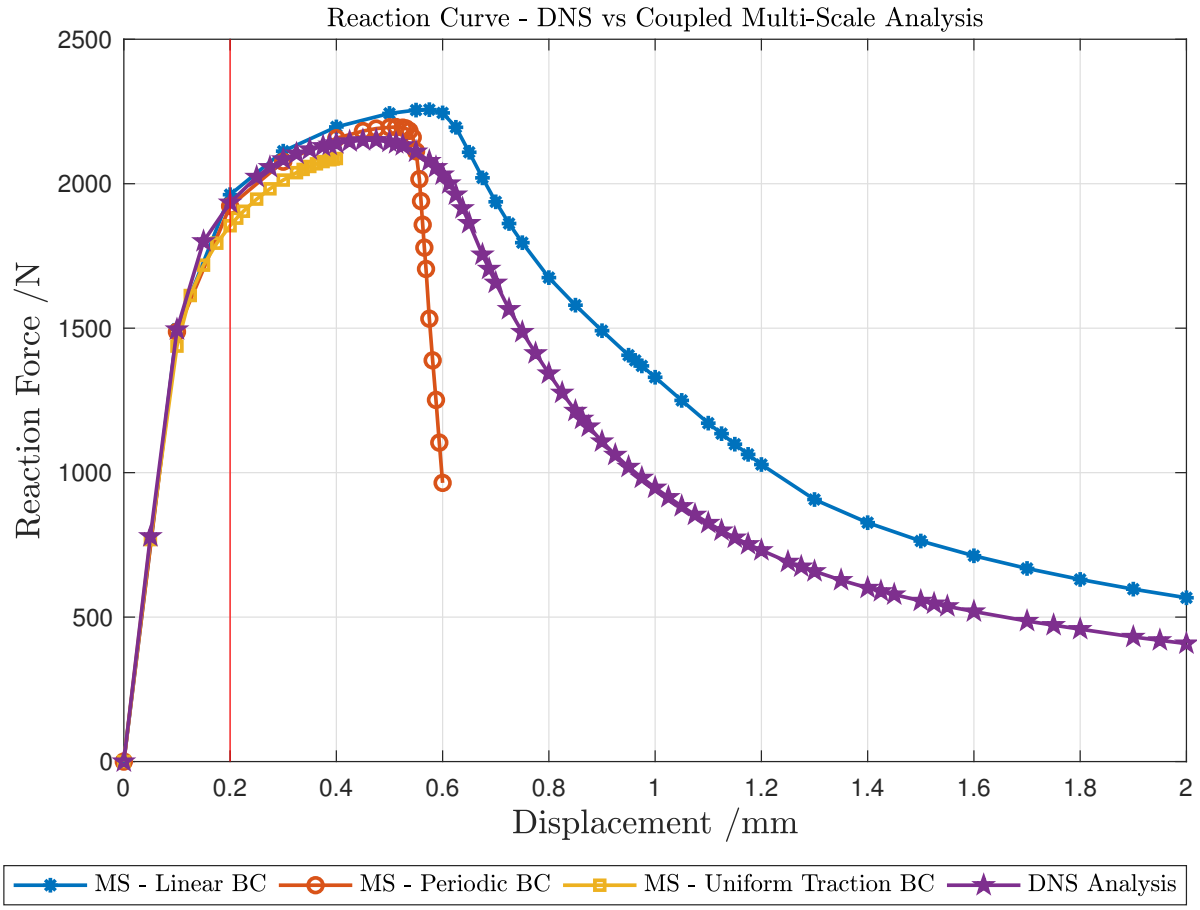

Figure 4.10: Reaction forces for the 4 mm notch specimen with a RVE with a characteristic length of 1 mm with a circular void.

Having already defined the RVEs that were considered, the results that were obtained at the micro-scale can be found in the next figures in terms of the effective Cauchy stress and equivalent strain fields, respectively.

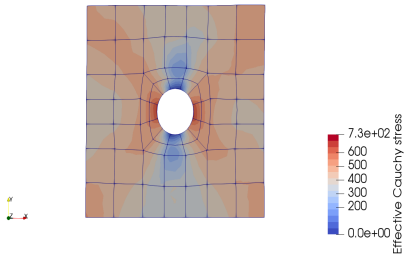

(a) Effective Cauchy stress field for the DNS model utilising a RVE_L =1 mm.

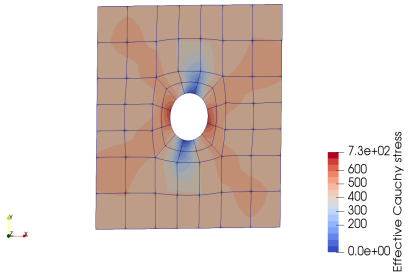

(b) Effective Cauchy stress field for the MS model utilising a RVE_L =1 mm considering a linear boundary condition at the micro-scale.

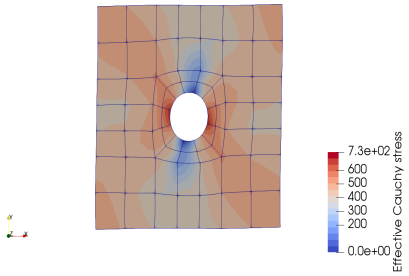

(c) Effective Cauchy stress field for the MS model utilising a RVE_L =1 mm considering a periodic boundary condition at the micro-scale.

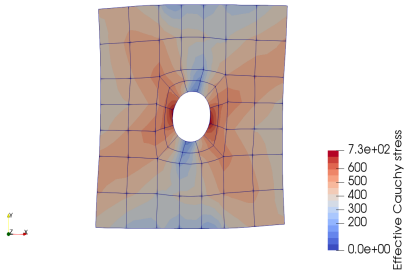

(d) Effective Cauchy stress field for the MS model utilising a RVE_L =1 mm considering a uniform traction boundary condition at the micro-scale.

Figure 4.11: Effective Cauchy stress field for the 4 mm notch specimen for a RVE_L =1 mm with a circular void.

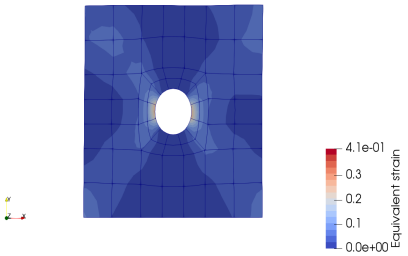

(a) Equivalent strain field for the DNS model utilising a RVE_L =1 mm.

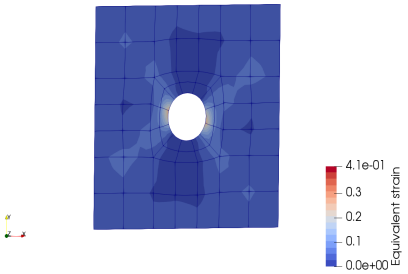

(b) Equivalent strain field for the MS model utilising a RVE_L =1 mm considering a linear boundary condition at the micro-scale.

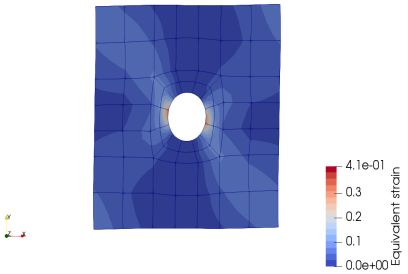

(c) Equivalent strain field for the MS model utilising a RVE_L =1 mm considering a periodic boundary condition at the micro-scale.

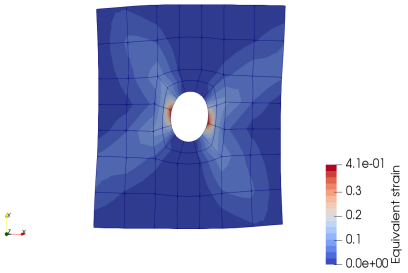

(d) Equivalent strain field for the MS model utilising a RVE_L =1 mm considering a uniform traction boundary condition at the micro-scale.

Figure 4.12: Equivalent strain field for the 4 mm notch specimen for a RVE_L =1 mm with a circular void.

RVE with a characteristic length of 2 mm

The results obtained at the macro-scale, the reaction forces, can be found bellow as follows.

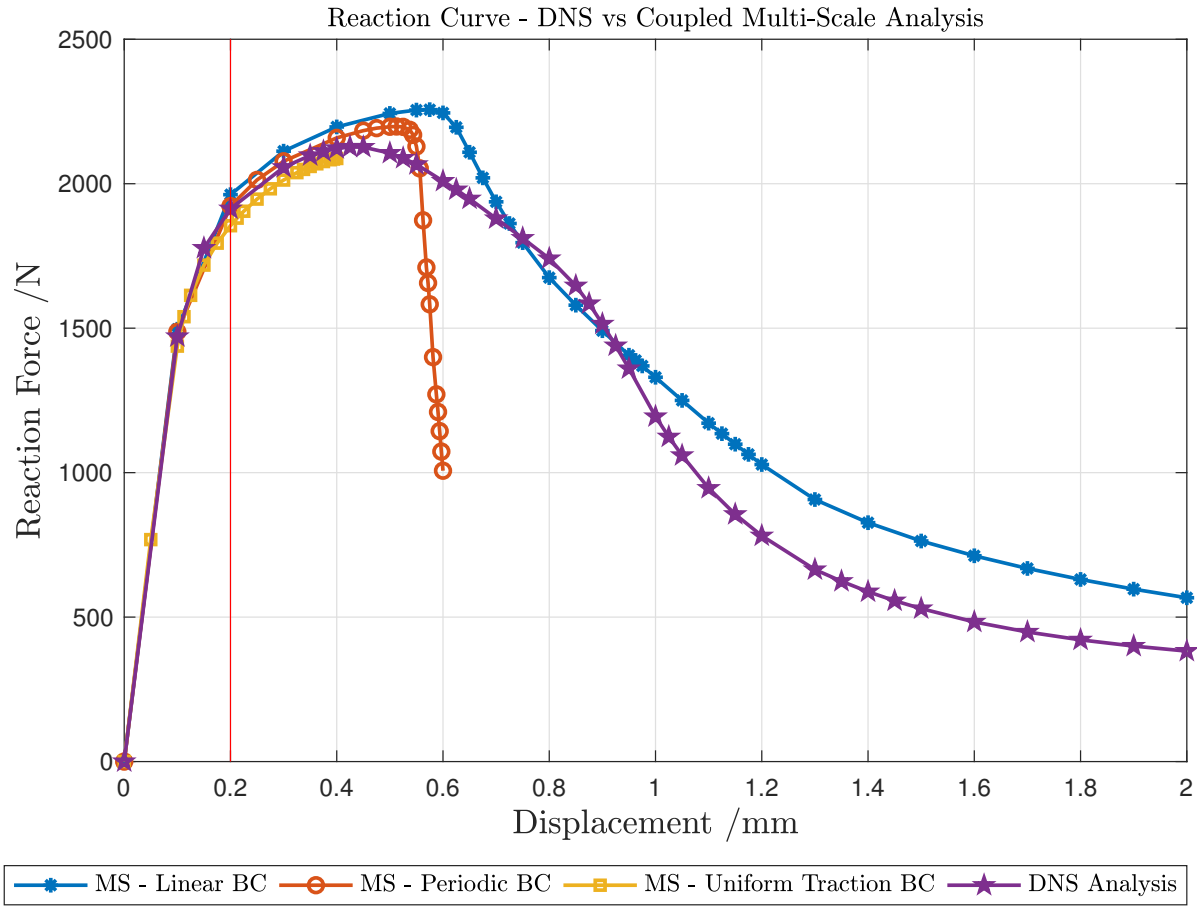

Figure 4.13: Reaction forces for the 4 mm notch specimen with a RVE with a characteristic length of 2 mm with a circular void.

Having already defined the RVEs that were considered, the results that were obtained at the micro-scale can be found in the next figures in terms of the effective Cauchy stress and equivalent strain, respectively.

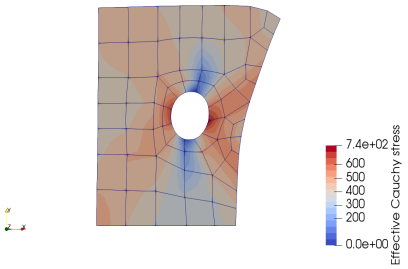

(a) Effective Cauchy stress field for the DNS model utilising a RVE_L =2 mm.

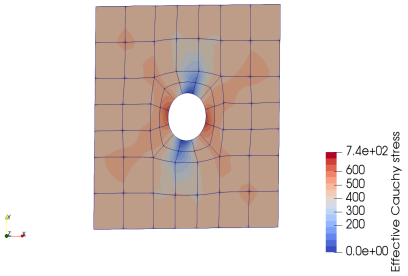

(b) Effective Cauchy stress field for the MS model utilising a RVE_L =2 mm considering a linear boundary condition at the micro-scale.

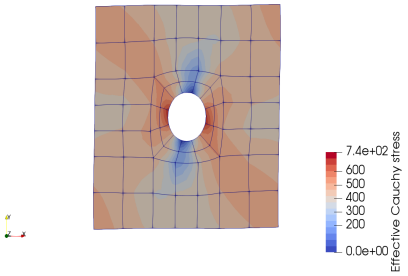

(c) Effective Cauchy stress field for the MS model utilising a RVE_L =2 mm considering a periodic boundary condition at the micro-scale.

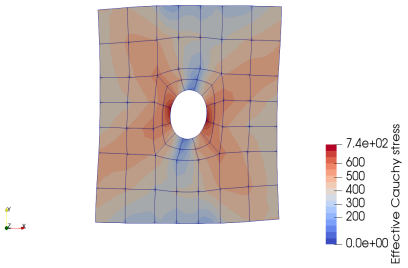

(d) Effective Cauchy stress field for the MS model utilising a RVE_L =2 mm considering a uniform traction boundary condition at the micro-scale.

Figure 4.14: Effective Cauchy stress field for the 4 mm notch specimen for a RVE_L =2 mm with a circular void.

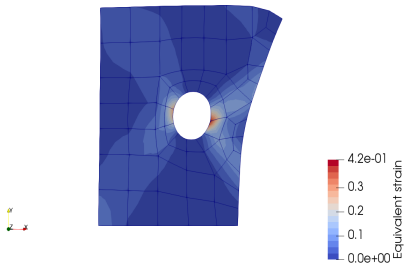

(a) Equivalent field for the DNS model utilising a RVE_L =2 mm.

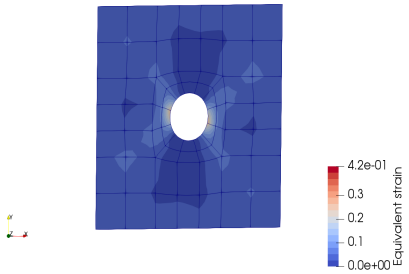

(b) Equivalent strain field for the MS model utilising a RVE_L =2 mm considering a linear boundary condition at the micro-scale.

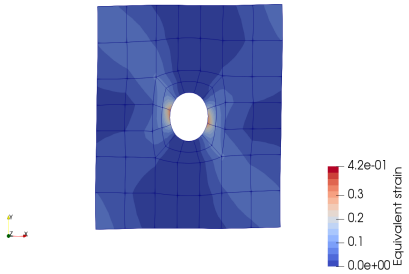

(c) Equivalent strain field for the MS model utilising a RVE_L =2 mm considering a periodic boundary condition at the micro-scale.

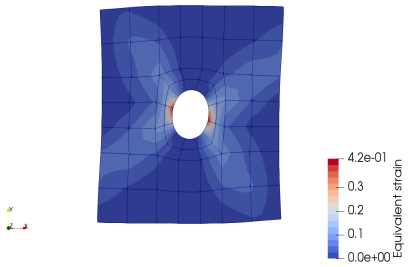

(d) Equivalent strain field for the MS model utilising a RVE_L =2 mm considering a uniform traction boundary condition at the micro-scale.

Figure 4.15: Effective Cauchy stress field for the 4 mm notch specimen for a RVE_L =2 mm with a circular void.

Since the periodic boundary condition is the one that provides more accurate results at the macro-scale, in the next figure is shown the obtained DNS solutions for the different RVEs characteristic lengths and the periodic boundary condition solution (since a first-order homogenisation method was utilised the results will be the same for each characteristic length).

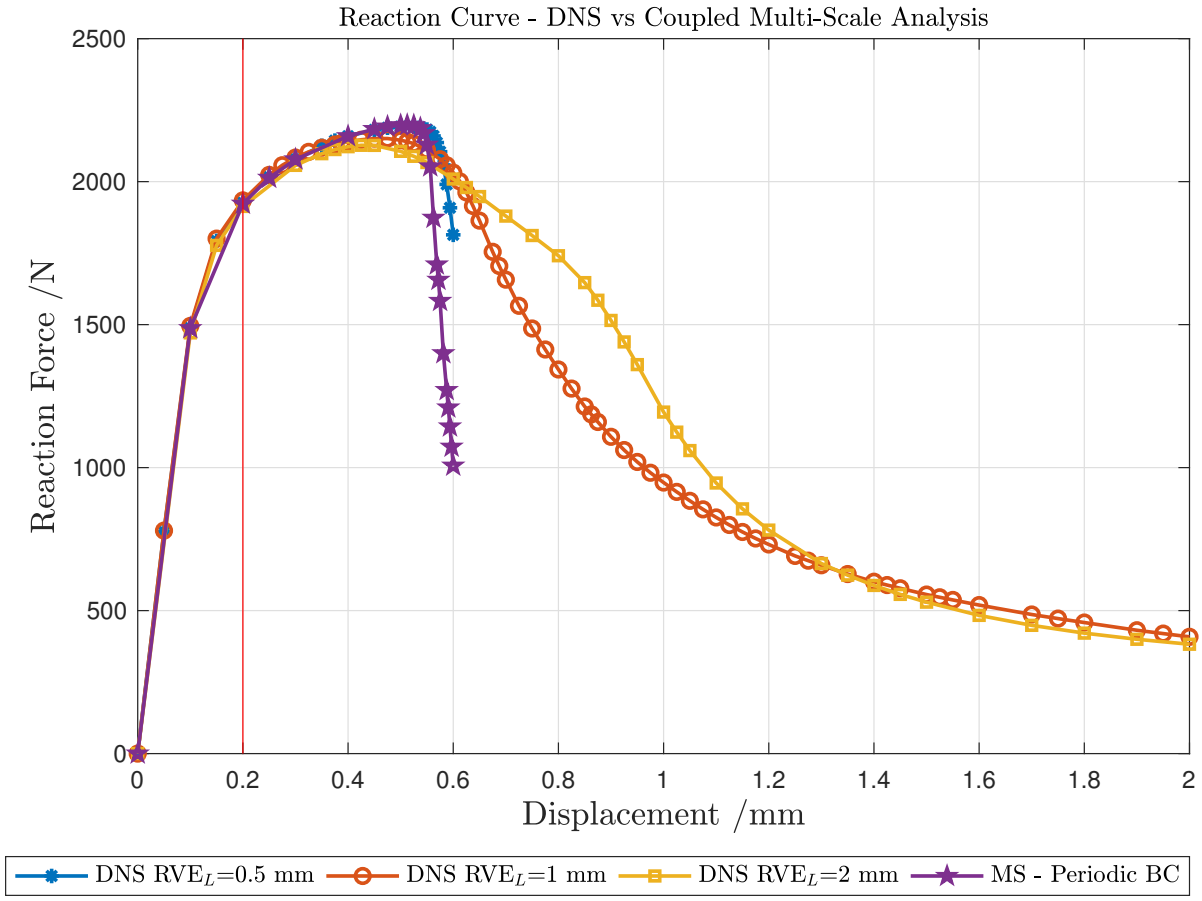

Figure 4.16: Reaction forces obtained for the different RVE characteristic lengths for the 4 mm notch specimen.

4.1.6.2 12 mm Notch

RVE with a characteristic length of 0.5 mm

The results obtained at the macro-scale, the reaction forces, can be found bellow as follows.

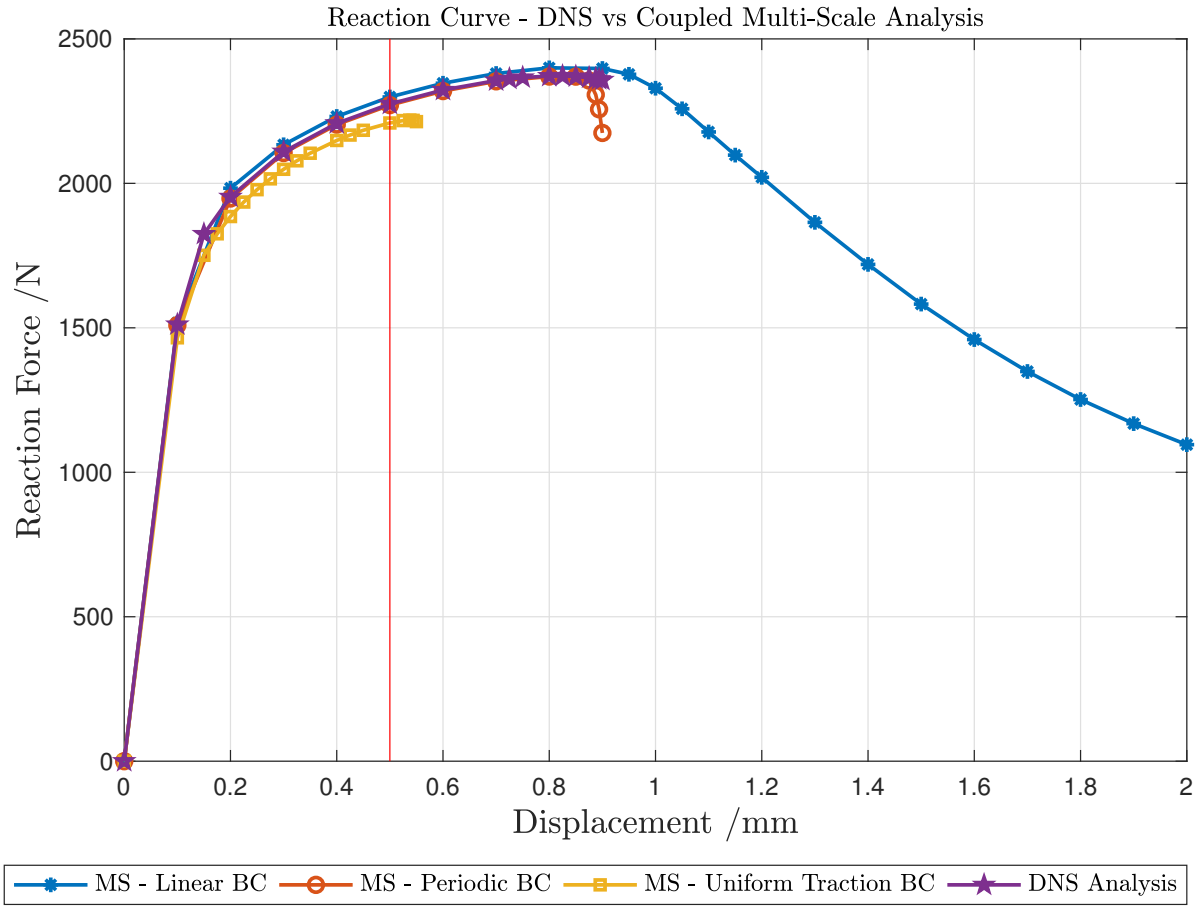

Figure 4.17: Reaction forces for the 12 mm notch specimen with a RVE with a characteristic length of 0.5 mm with a circular void.

Having already defined the RVEs that were considered, the results that were obtained at the micro-scale can be found in the next figures in terms of the effective Cauchy stress and equivalent strain, respectively.

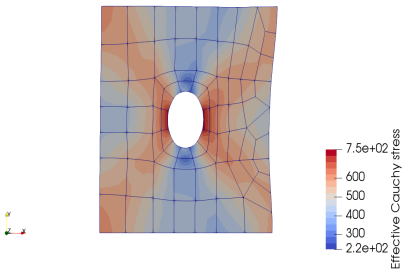

(a) Effective Cauchy stress field for the DNS model utilising a RVE_L =0.5 mm.

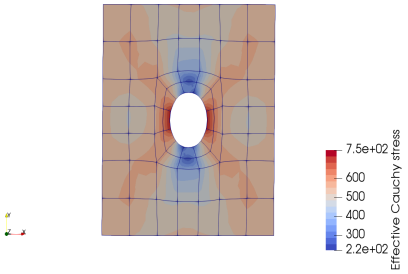

(b) Effective Cauchy stress field for the MS model utilising a RVE_L =0.5 mm considering a linear boundary condition at the micro-scale.

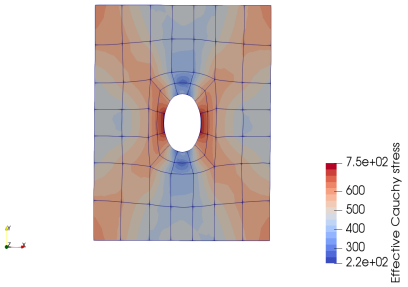

(c) Effective Cauchy stress field for the MS model utilising a RVE_L =0.5 mm considering a periodic boundary condition at the micro-scale.

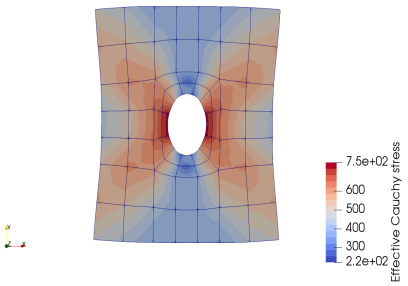

(d) Effective Cauchy stress field for the MS model utilising a RVE_L =0.5 mm considering a uniform traction boundary condition at the micro-scale.

Figure 4.18: Effective Cauchy stress field for the 12 mm notch specimen for a RVE_L =0.5 mm with a circular void.

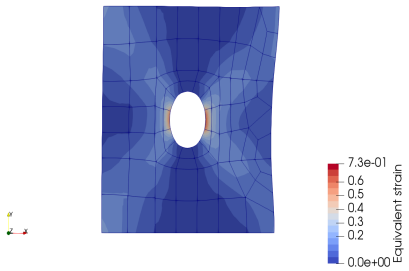

(a) Equivalent strain field for the DNS model utilising a RVE_L =0.5 mm.

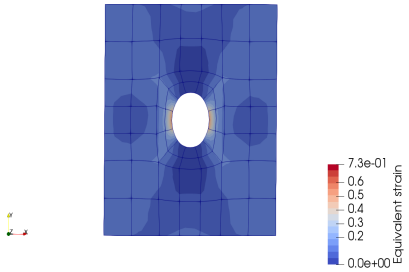

(b) Equivalent strain field for the MS model utilising a RVE_L =0.5 mm considering a linear boundary condition at the micro-scale.

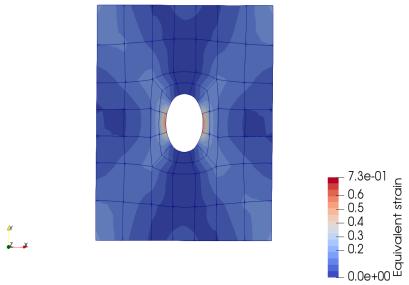

(c) Equivalent strain field for the MS model utilising a RVE_L =0.5 mm considering a periodic boundary condition at the micro-scale.

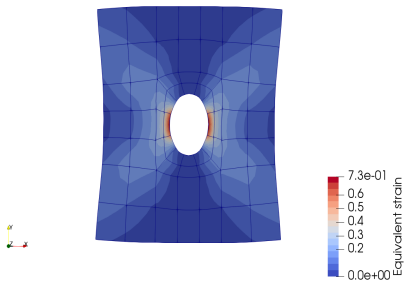

(d) Equivalent strain field for the MS model utilising a RVE_L =0.5 mm considering a uniform traction boundary condition at the micro-scale.

Figure 4.19: Equivalent strain field for the 12 mm notch specimen for a RVE_L =0.5 mm with a circular void.

RVE with a characteristic length of 1 mm

The results obtained at the macro-scale, the reaction forces, can be found bellow as follows.

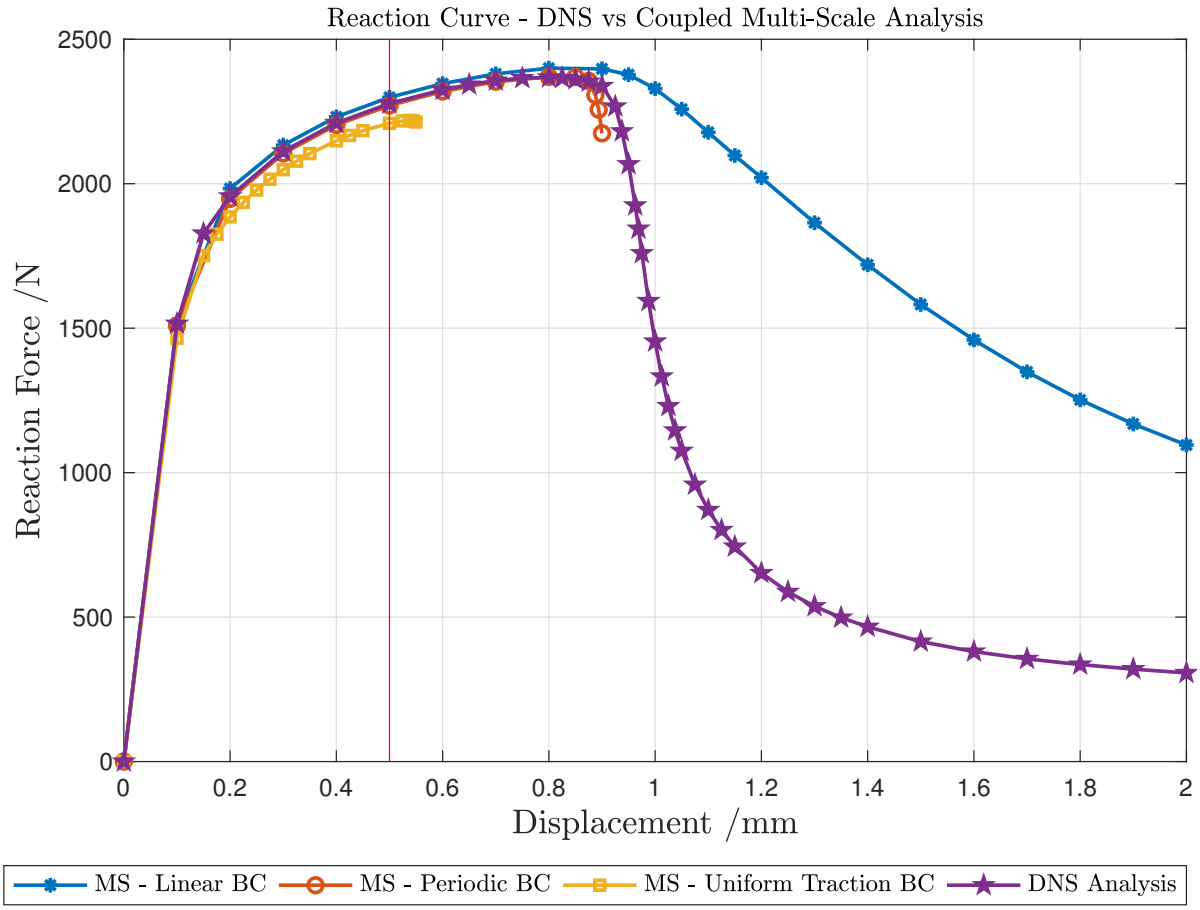

Figure 4.20: Reaction forces for the 12 mm specimen with a RVE with a characteristic length of 1 mm with a circular void.

Having already defined the RVEs that were considered, the results that were obtained at the micro-scale can be found in the next figures in terms of the effective Cauchy stress and equivalent strain fields, respectively.

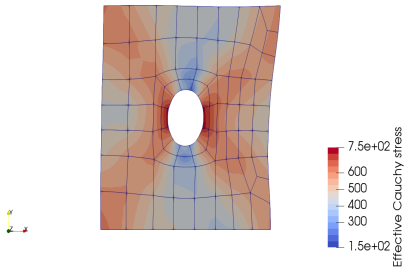

(a) Effective Cauchy stress field for the DNS model utilising a RVE_L =1 mm.

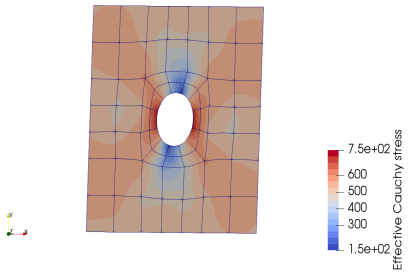

(b) Effective Cauchy stress field for the MS model utilising a RVE_L =1 mm considering a linear boundary condition at the micro-scale.

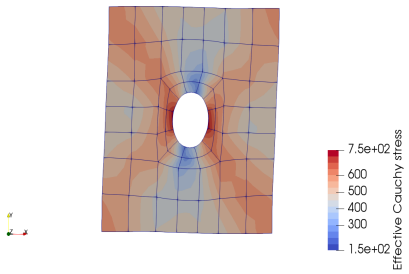

(c) Effective Cauchy stress field for the MS model utilising a RVE_L =1 mm considering a periodic boundary condition at the micro-scale.

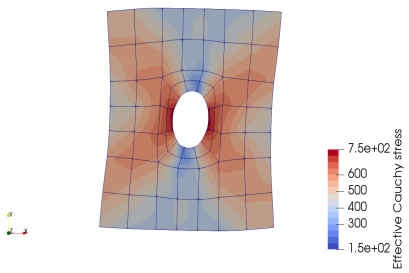

(d) Effective Cauchy stress field for the MS model utilising a RVE_L =1 mm considering a uniform traction boundary condition at the micro-scale.

Figure 4.21: Effective Cauchy stress field for the 12 mm notch specimen for a RVE_L =1 mm with a circular void.

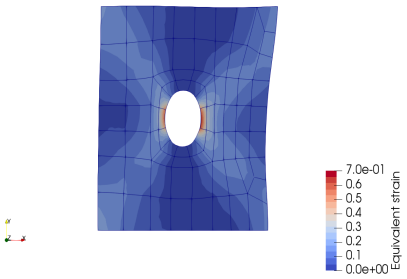

(a) Equivalent field for the DNS model utilising a RVE_L =1 mm.

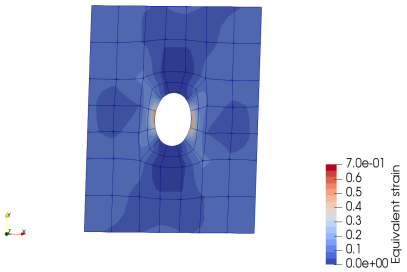

(b) Equivalent strain field for the MS model utilising a RVE_L =1 mm considering a linear boundary condition at the micro-scale.

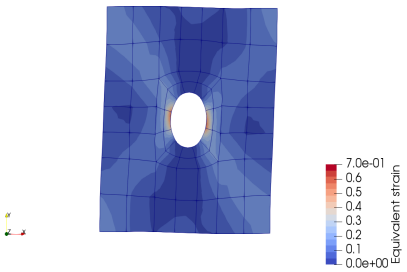

(c) Equivalent strain field for the MS model utilising a RVE_L =1 mm considering a periodic boundary condition at the micro-scale.

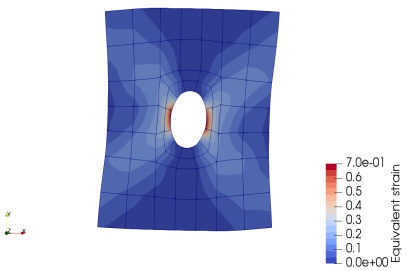

(d) Equivalent strain field for the MS model utilising a RVE_L =1 mm considering a uniform traction boundary condition at the micro-scale.

Figure 4.22: Equivalent strain field for the 12 mm notch specimen for a RVE_L =1 mm with a circular void.

RVE with a characteristic length of 2 mm

The results obtained at the macro-scale, the reaction forces, can be found bellow as follows.

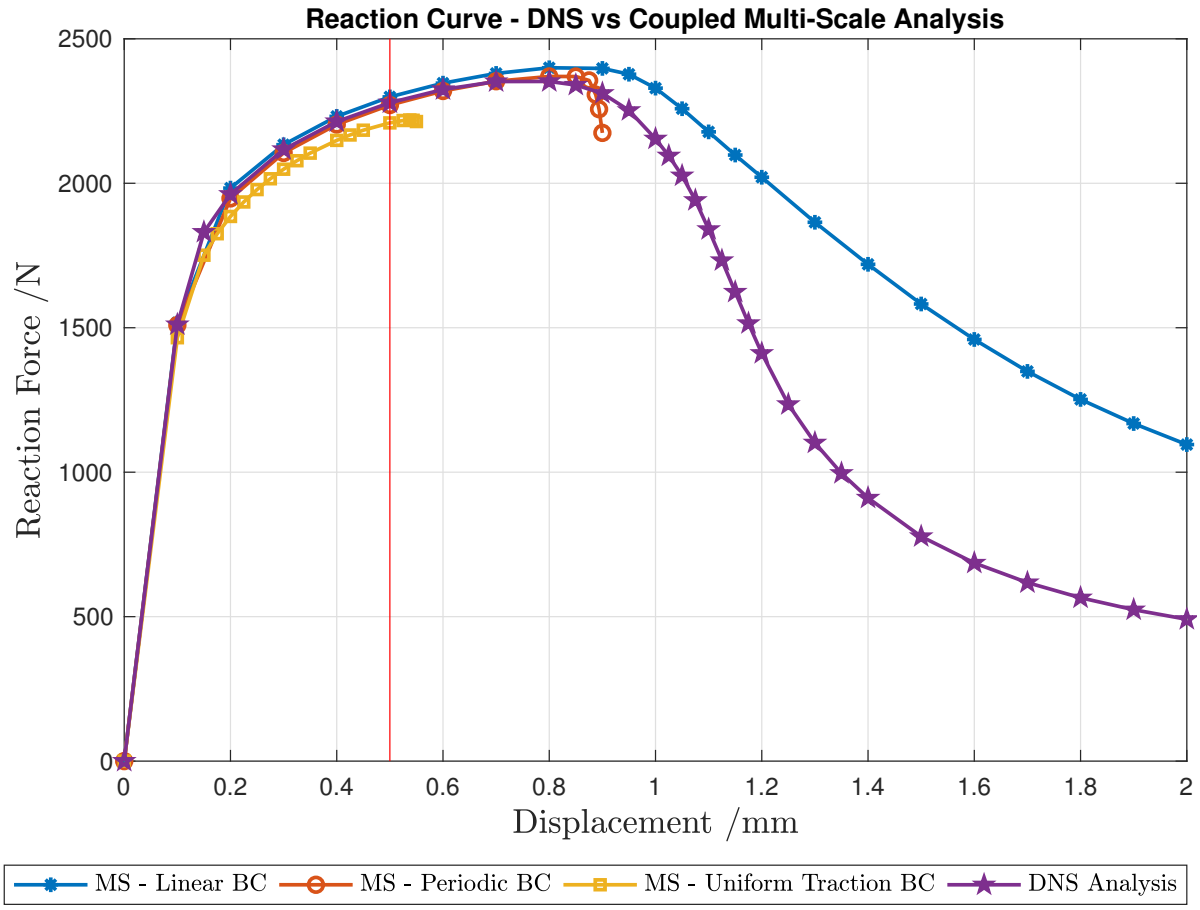

Figure 4.23: Reaction forces for the 12 mm notch specimen with a RVE with a characteristic length of 2 mm with a circular void.

Having already defined the RVEs that were considered, the results that were obtained at the micro-scale can be found in the next figures in terms of the effective Cauchy stress and equivalent strain fields, respectively.

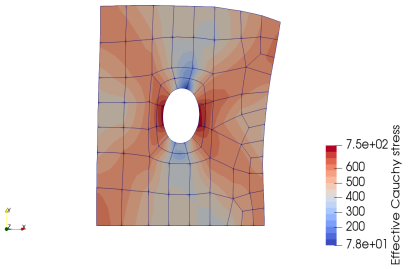

(a) Effective Cauchy stress field for the DNS model utilising a RVE_L =2 mm.

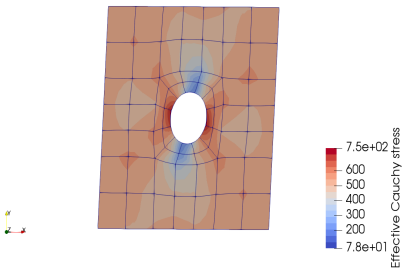

(b) Effective Cauchy stress field for the MS model utilising a RVE_L =2 mm considering a linear boundary condition at the micro-scale.

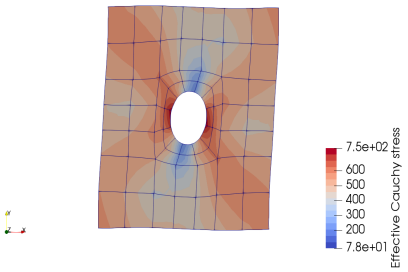

(c) Effective Cauchy stress field for the MS model utilising a RVE_L =2 mm considering a periodic boundary condition at the micro-scale.

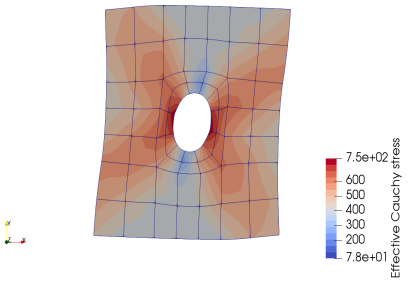

(d) Effective Cauchy stress field for the MS model utilising a RVE_L =2 mm considering a uniform traction boundary condition at the micro-scale.

Figure 4.24: Effective Cauchy stress field for the 12 mm notch specimen for a RVE_L =2 mm with a circular void.

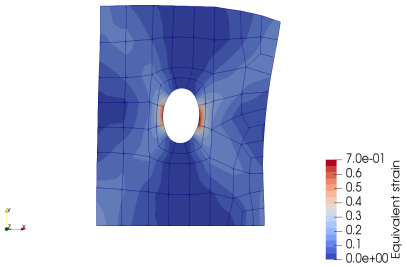

(a) Equivalent field for the DNS model utilising a RVE_L =2 mm.

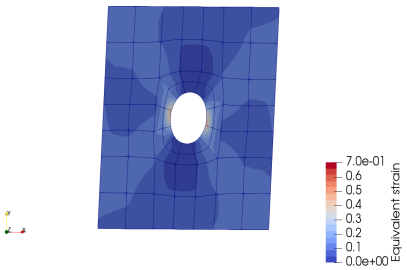

(b) Equivalent strain field for the MS model utilising a RVE_L =2 mm considering a linear boundary condition at the micro-scale.

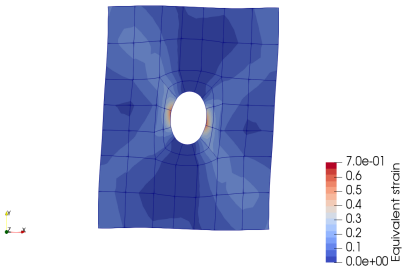

(c) Equivalent strain field for the MS model utilising a RVE_L =2 mm considering a periodic boundary condition at the micro-scale.

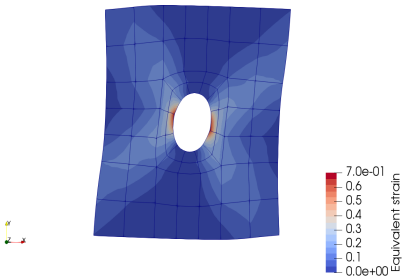

(d) Equivalent strain field for the MS model utilising a RVE_L =2 mm considering a uniform traction boundary condition at the micro-scale.

Figure 4.25: Equivalent strain field for the 12 mm notch specimen for a RVE_L =2 mm with a circular void.

Since the periodic boundary condition is the one that provides more accurate results at the macro-scale, in the next figure is shown the obtained DNS solutions for the different RVEs characteristic lengths and the periodic boundary condition solution (since a first-order homogenisation method was utilised the results will be the same for each characteristic length).

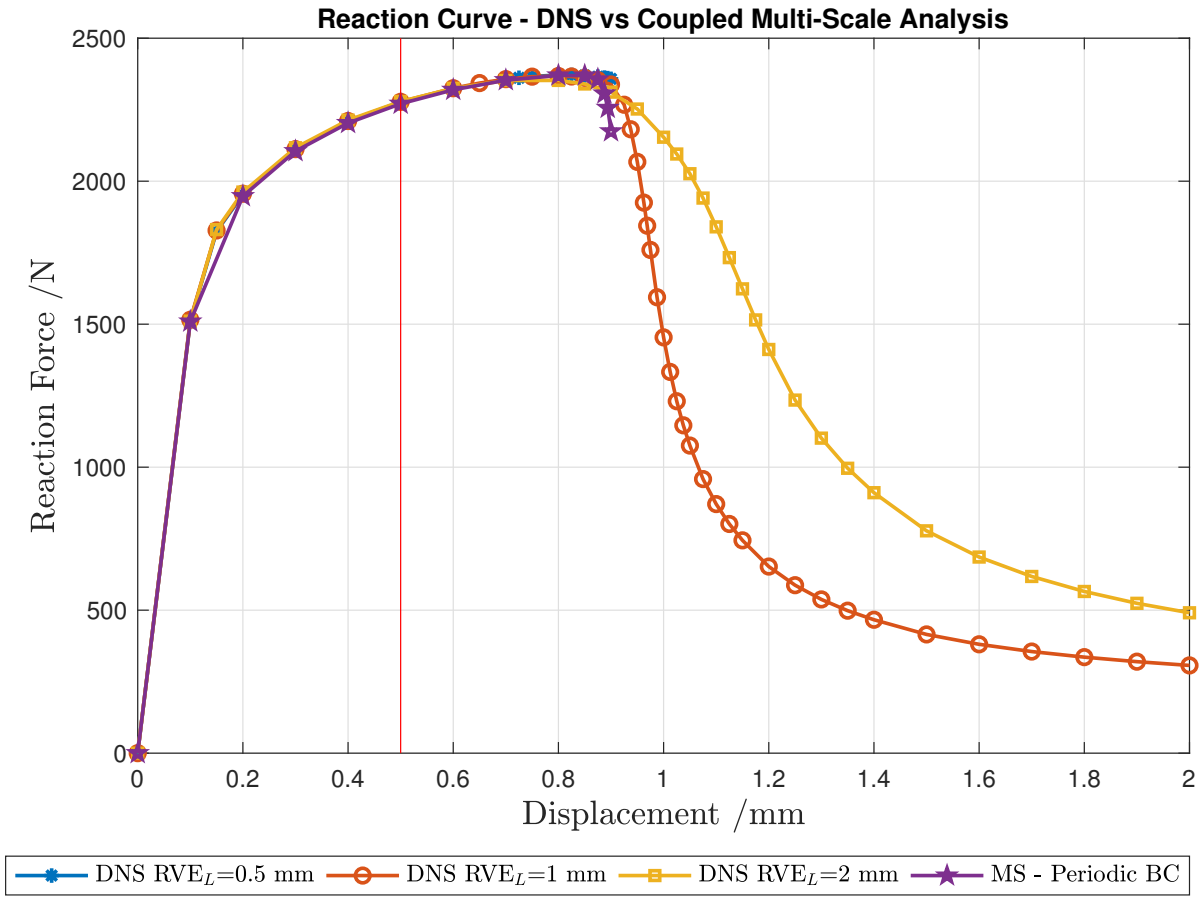

Figure 4.26: Reaction forces obtained for the different RVE characteristic lengths for the 12 mm notch specimen.

4.1.7 Results Analysis

Taking into account the results that have been obtained at the macro-scale (curves of reaction forces) for the 4 mm notch it can be concluded that, both in the elastic and plastic domain, the curve that corresponds to solution of the MS model with periodic boundary condition, fits the solution obtained by the DNS model, for every RVE characteristic length that has been studied. The curves corresponding to the solutions obtained by the MS models with linear and uniform traction boundary conditions, fit above and below , respectively, the reference curve (DNS solution) and this can be explained by the fact that this boundary conditions are the most and least restrictive ones. As it has been stated the curve that fits the best way to the DNS solution is the result of the MS model with the periodic boundary condition. This can be explained by the fact that the microsctructure that has been modelled in the DNS model is periodic. Until the representative displacement, the curves fit almost exactly leading to the fact that, in this case, the principle of separation of scales isn't broken. Despite that, it can be seen that, for the RVEs with bigger characteristic lengths, the periodic MS solution and the DNS one tend to separate themselves right before the softening regime takes place. The separation of the curves takes place approximately for a prescribed displacement of 0.55 mm for the RVE_L =0.5 mm, for a prescribed displacement of 0.40 mm for the RVE_L =1 mm and for a prescribed displacement of 0.2 mm for the RVE_L =2 mm.

In terms of the micro-structural results one can state that all solutions provided by first-order computational homogenization procedure are close to the ones that have been obtained by the DNS analysis, in terms of effective Cauchy stress and equivalent strain fields, for all RVE characteristic lengths being once again the periodic boundary condition the one who seems to "fit" better to the solution provided by the DNS analysis. Hence, a second-order computational homogenization procedure isn't needed since that a first-order one already can depict the micro-structural deformation phenomenon in a proper way.

For the 12 mm notch, the same conclusions can be made, in a general way. As it was expected, for this type of notch, which is less pronounced, the reaction force curves tend to fit with each other for a bigger imposed displacement. The separation of the curves provided by the DNS analysis and the MS analysis only occurs approximately for a prescribed displacement of 0.8 mm for all RVE sizes. In terms of microstructural results (effective Cauchy stress and equivalent strain) fields for all RVE characteritic sizes the solutions provided by the MS models are similar to the ones obtained by the corresponding DNS model being the periodic boundary condition, once again, the ones that produces "better" results.

4.2 Traction Solicitation Utilising a RVE with an Elastic Inclusion

In this section one will assess the PSS where the micro-structure is represented by a RVE with an elastic inclusion.

4.2.1 Multi-Scale (MS) Models

The multi-scale model can be divided into two distinct models. The macro-scale model and the micro-scale one. The multi-scale models that have been used are presented below.

4.2.1.1 Macro-Scale Meshes

The macro-scale meshes that were utilised are identical to the ones defined in subsubsection 4.1.3.1. The material that was utilised at the macro-scale level is the aluminium alloy 2024-T351, having it been already introduced in Section 4.1.2.

4.2.1.2 Micro-Scale Mesh: Definition of the RVEs' Properties

The RVE that was modelled at the micro-scale is equal to the one (in terms of size and volume fraction) presented in subsubsection 4.1.3.2. The difference that occurs is that instead of a void, the RVE is composed by an elastic inclusion and its model can be seen below.

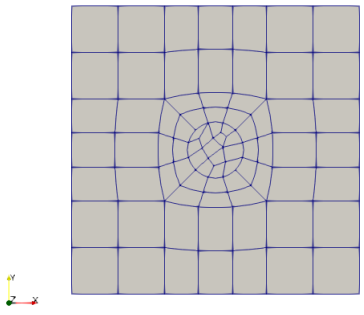

Figure 4.27: Micro-scale mesh of the speicmens that have been studied.

The RVE's material remains the same as mentioned in subsubsection 4.1.3.2 being the elastic material that constitutes the inclusion Boron. Its properties can be found in the following table.

Table 4.7: Elastic properties of the Boron inclusion. Taken from Ghosh et al. (1995).

Young Modulus	E	400 GPa
Poisson's Ratio	ν	0.3

The micro-scale mesh properties (number of nodes and elements) can be found in the following table. The type of element that was utilised was once again a 8-noded quadratic element.

Table 4.8: Micro-scale mesh properties for the 4 mm notch specimen with an elastic inclusion.

Number of Elements	Number of Nodes
78	263

4.2.2 DNS Models

Having introduced the specimens geometry and the micro-scale mesh it is now possible to define the DNS models that have been utilised. As it has already been stated in the introductory chapters of the present report, a DNS simulation requires an explicitly modelation of the microsctructure of the material. The process of modelling the specimens was identical to the one presented in Section 4.1.4 and they are presented below, for the 4 and 12 mm notch specimens, respectively. The highlighted RVEs are the ones that were analysed further in this chapter.

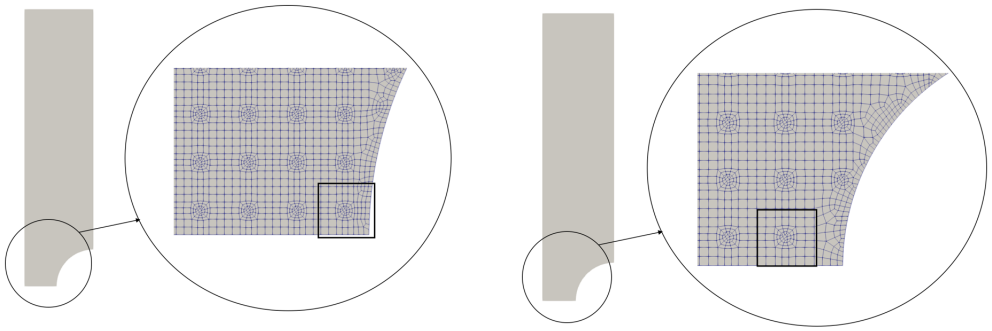

(a) Close up of the notch zone of the DNS model of the 4 mm notch specimen using a RVE_L =0.5 mm with an elastic inclusion.

(b) Close up of the notch zone of the DNS model of the 4 mm notch specimen using a RVE_L =1 mm with an elastic inclusion..

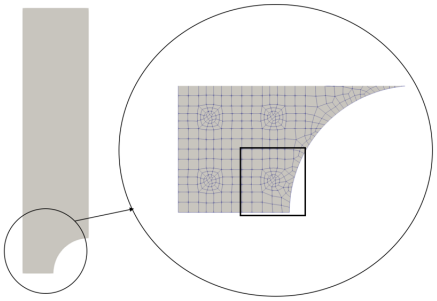

(c) Close up of the notch zone of the DNS model of the 4 mm notch specimen using a RVE_L =2 mm with an elastic inclusion.

Figure 4.28: Close up of the notch zone of the different DNS models for the 4 mm notch specimen with an elastic inclusion.

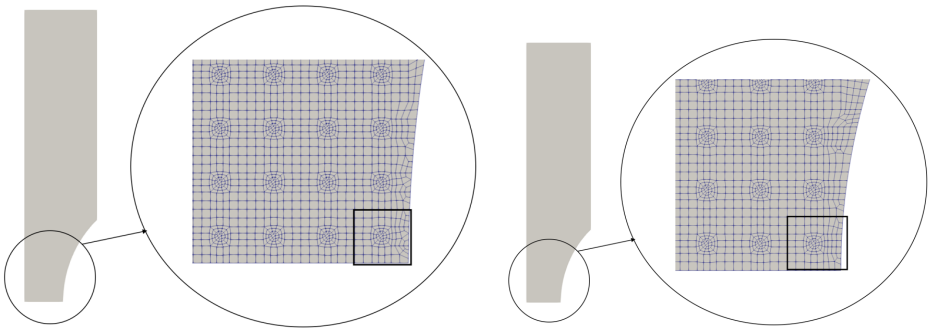

(a) Close up of the notch zone of the DNS model of the 12 mm notch specimen using a RVE_L =0.5 mm with an elastic inclusion.

(b) Close up of the notch zone of the DNS model of the 12 mm notch specimen using a RVE_L =1 mm with an elastic inclusion.

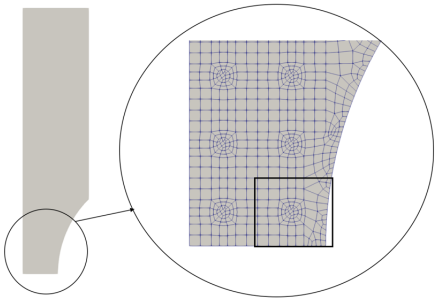

(c) Close up of the notch zone of the DNS model of the 12 mm notch specimen using a RVE_L =2 mm with an elastic inclusion.

Figure 4.29: Close up of the notch zone of the different DNS models for the 12 mm notch specimen with an elastic inclusion.

A resume of the DNS mesh properties can be found below on the following tables.

Table 4.9: DNS meshes properties for the 4 mm notch specimen with an elastic inclusion.

RVE_L	Number of Elements	Number of Nodes
0.5	66747	201312
1	16318	49503
2	4300	13205

Table 4.10: DNS meshes properties for the 12 mm notch specimen with an elastic inclusion.

RVE_L	Number of Elements	Number of Nodes
0.5	64246	193815
1	15472	46937
2	4248	13069

4.2.3 Numerical Simulations

Having already defined the properties of the multi-scale models as of the DNS ones, one can define the numerical simulations parameters. For every numerical simulation, it was prescribed a nodal displacement of 2 mm in the top nodes of the macro-scale meshes as well as of the DNS ones. The prescribed displacement was divided in 20 increments. The boundary conditions that were applied were only the symmetry boundary conditions. For the coupled multi-scale, the simulations were repeated for each micro-scale boundary condition (linear, periodic and uniform traction). As it has already been stated the type of elements that were utilised is a 8-noded quadratic element and the integration was made with 4 Gauss points.

4.2.4 Results Obtained

In the following section, the results that were obtained are going to be presented and then discussed. The presentation of the results is going to be made in an identical way that was made in Section 4.1.6. The results obtained as well as the comparison between them are demonstrated in the following sections for the 4 and 12 mm notch specimens.

The procedure of analysis was the same that is defined at Section 4.1.6. For the DNS models, the RVE that was considered can be found highlighted in Figure 4.28 for the 4 mm notch specimen and in Figure 4.29 for the 12 mm notch specimen.

For the multi-scale models, each RVE is associated to a Gauss point making that the choosing process has to be made by establishing the same criteria for all RVEs. As it is impossible to correspond the RVEs in the MS models to the RVEs presented in the DNS ones, the criteria that was established is that the RVE chosen at the MS models was the RVE which coordinates would be closer to the centroid of the RVE at the homologous DNS simulation. The elements that were considered for this analysis are the same that were considered in Section 4.1.6.

4.2.4.1 4 mm Notch

RVE with a characteristic length of 0.5 mm

The results obtained at the macro-scale, the reaction forces, can be found bellow as follows.

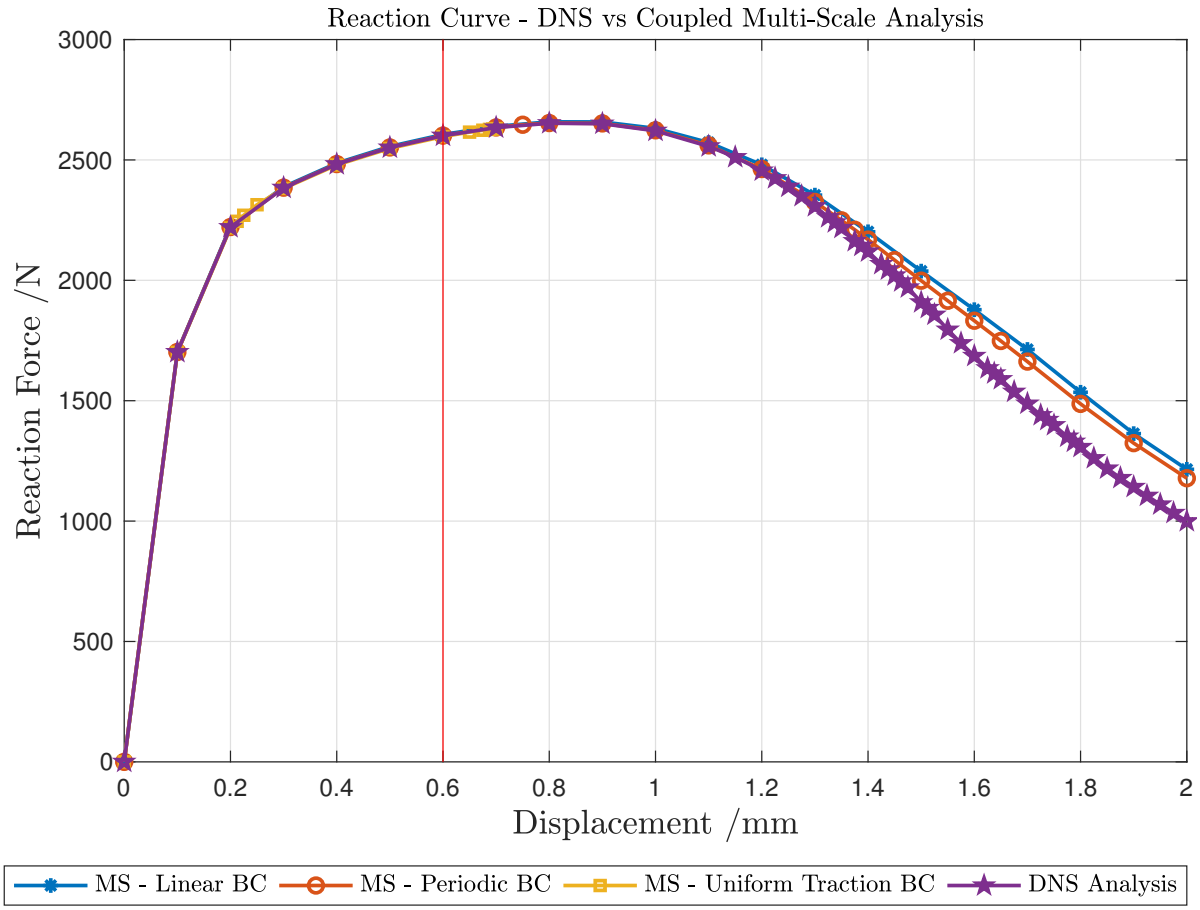

Figure 4.30: Reaction forces for the 4 mm notch specimen with a RVE with a characteristic length of 0.5 mm with an elastic inclusion.

Having already defined the RVEs that were considered, the results that were obtained at the micro-scale can be found in the next figures in terms of the effective Cauchy stress and equivalent strain fields, respectively.

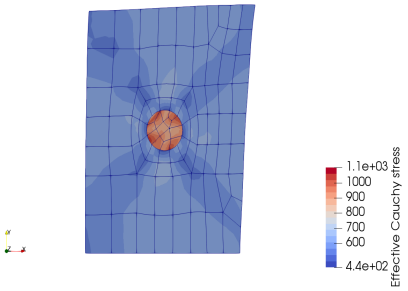

(a) Effective Cauchy stress field for the DNS model utilising a RVE_L =0.5 mm.

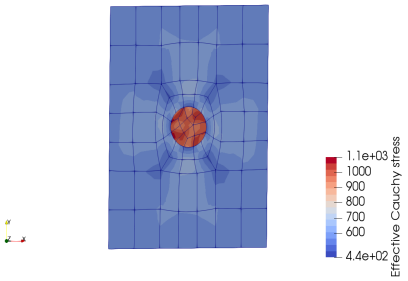

(b) Effective Cauchy stress field for the MS model utilising a RVE_L =0.5 mm considering a linear boundary condition at the micro-scale.

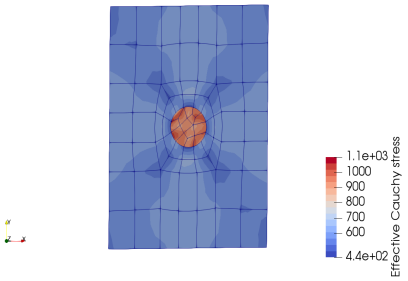

(c) Effective Cauchy stress field for the MS model utilising a RVE_L =0.5 mm considering a periodic boundary condition at the micro-scale.

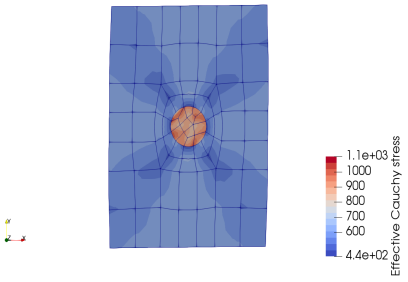

(d) Effective Cauchy stress field for the MS model utilising a RVE_L =0.5 mm considering a uniform traction boundary condition at the micro-scale.

Figure 4.31: Effective Cauchy stress field for the 4 mm notch specimen for a RVE_L =0.5 mm with an elastic inclusion.

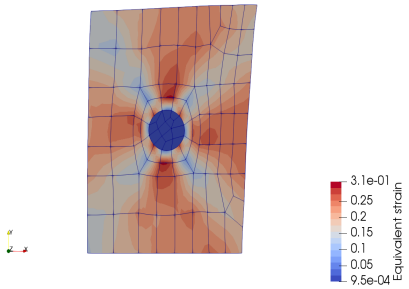

(a) Equivalent strain field for the DNS model utilising a RVE_L =0.5 mm.

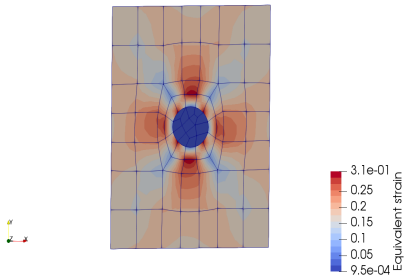

(b) Equivalent strain field for the MS model utilising a RVE_L =0.5 mm considering a linear boundary condition at the micro-scale.

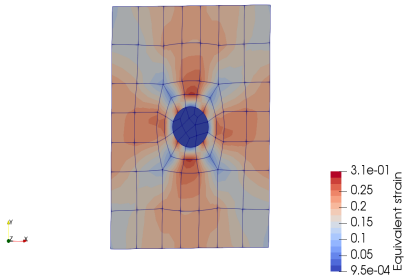

(c) Equivalent strain field for the MS model utilising a RVE_L =0.5 mm considering a periodic boundary condition at the micro-scale.

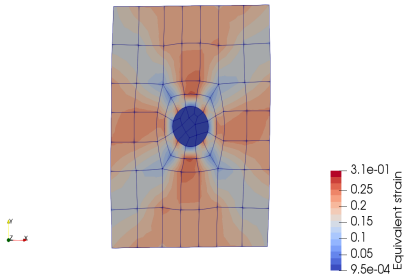

(d) Equivalent strain field for the MS model utilising a RVE_L =0.5 mm considering a uniform traction boundary condition at the micro-scale.

Figure 4.32: Equivalent strain field for the 4 mm notch specimen for a RVE_L =0.5 mm with an elastic inclusion.

RVE with a characteristic length of 1 mm

The results obtained at the macro-scale, the reaction forces, can be found bellow as follows.

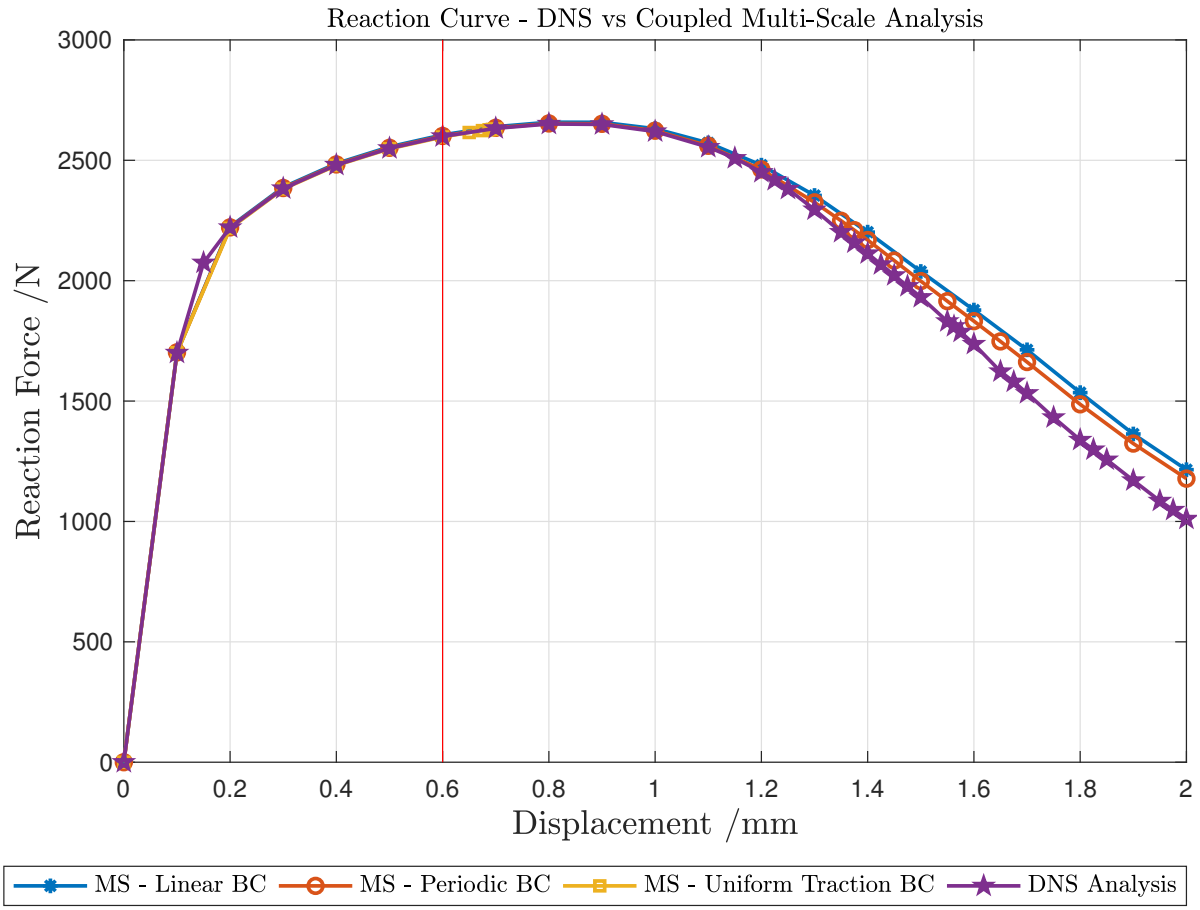

Figure 4.33: Reaction forces for the 4 mm notch specimen with a RVE with a characteristic length of 1 mm with an elastic inclusion.

Having already defined the RVEs that were considered, the results that were obtained at the micro-scale can be found in the next figures in terms of the effective Cauchy stress and equivalent strain fields, respectively.

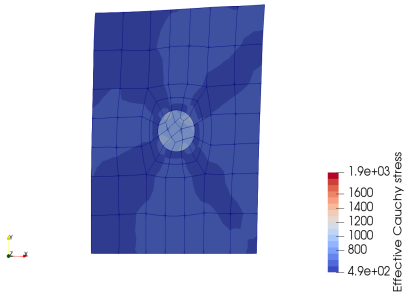

(a) Effective Cauchy stress field for the DNS model utilising a RVE_L =1 mm.

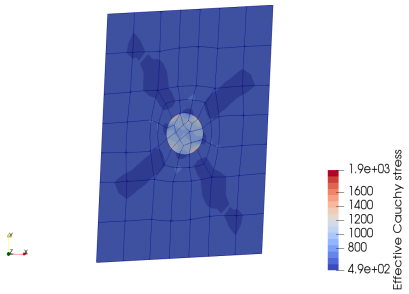

(b) Effective Cauchy stress field for the MS model utilising a RVE_L =1 mm considering a linear boundary condition at the micro-scale.

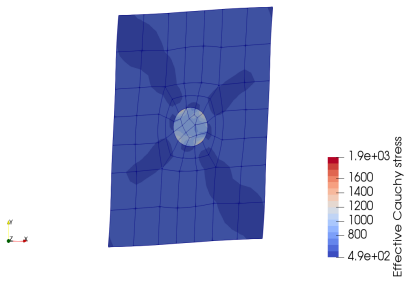

(c) Effective Cauchy stress field for the MS model utilising a RVE_L =1 mm considering a periodic boundary condition at the micro-scale.

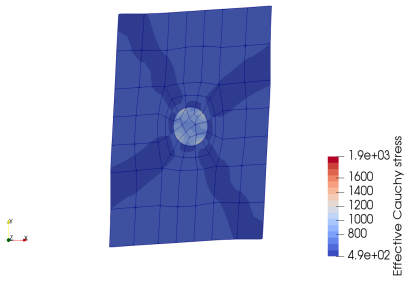

(d) Effective Cauchy stress field for the MS model utilising a RVE_L =1 mm considering a uniform traction boundary condition at the micro-scale.

Figure 4.34: Effective Cauchy stress field for the 4 mm notch specimen for a RVE_L =1 mm with an elastic inclusion.

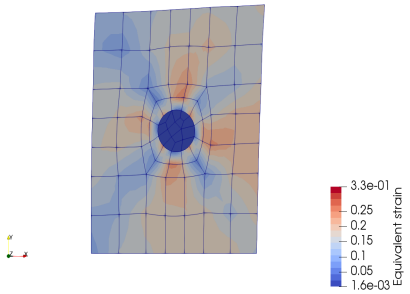

(a) Equivalent strain field for the DNS model utilising a RVE_L =1 mm.

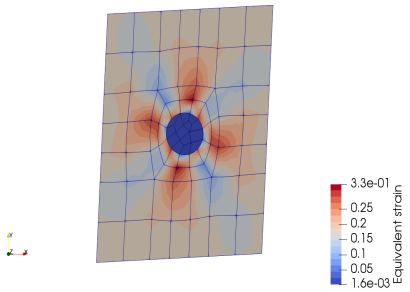

(b) Equivalent strain field for the MS model utilising a RVE_L =1 mm considering a linear boundary condition at the micro-scale.

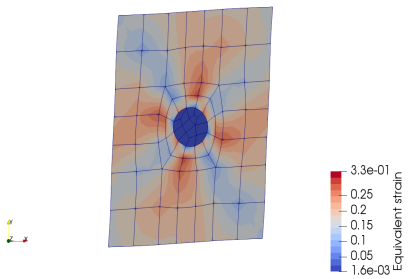

(c) Equivalent strain field for the MS model utilising a RVE_L =1 mm considering a periodic boundary condition at the micro-scale.

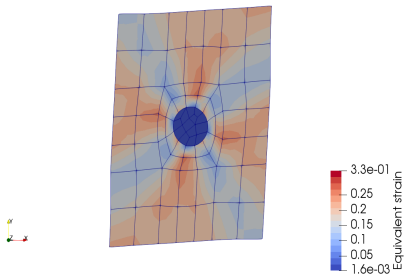

(d) Equivalent strain field for the MS model utilising a RVE_L =1 mm considering a uniform traction boundary condition at the micro-scale.

Figure 4.35: Equivalent strain field for the 4 mm notch specimen for a RVE_L =1 mm with an elastic inclusion.

RVE with a characteristic length of 2 mm

The results obtained at the macro-scale, the reaction forces, can be found bellow as follows.

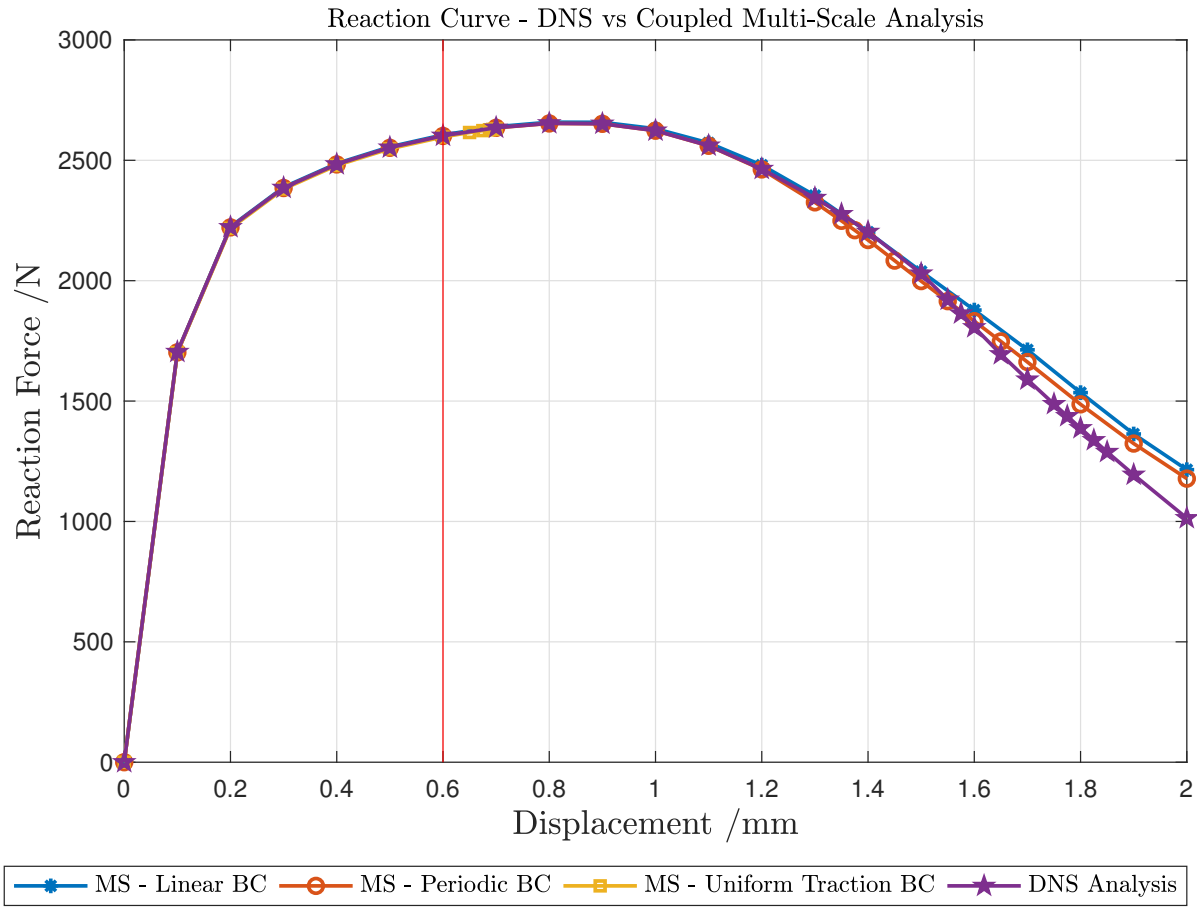

Figure 4.36: Reaction forces for the 4 mm notch specimen with a RVE with a characteristic length of 2 mm with an elastic inclusion.

Having already defined the RVEs that were considered, the results that were obtained at the micro-scale can be found in the next figures in terms of the effective Cauchy stress and equivalent strain fields, respectively.

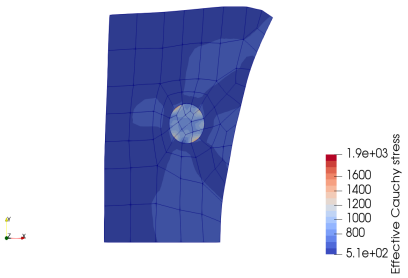

(a) Effective Cauchy stress field for the DNS model utilising a RVE_L =2 mm with an elastic inclusion.

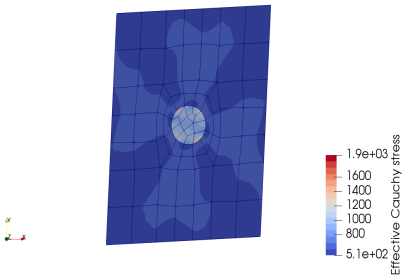

(b) Effective Cauchy stress field for the MS model utilising a RVE_L =2 mm considering a linear boundary condition at the micro-scale.

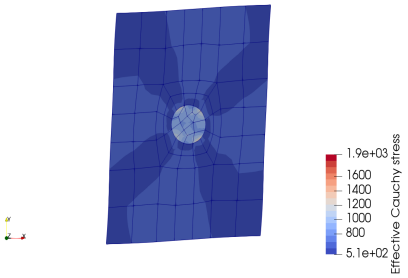

(c) Effective Cauchy stress field for the MS model utilising a RVE_L =2 mm considering a periodic boundary condition at the micro-scale.

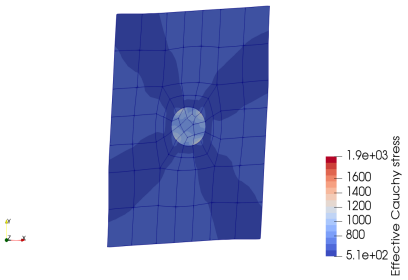

(d) Effective Cauchy stress field for the MS model utilising a RVE_L =2 mm considering a uniform traction boundary condition at the micro-scale.

Figure 4.37: Effective Cauchy stress field for the 4 mm notch specimen for a RVE_L =2 mm with an elastic inclusion.

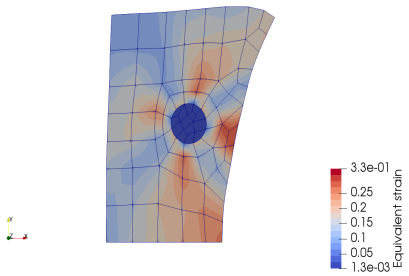

(a) Equivalent field for the DNS model utilising a RVE_L =2 mm.

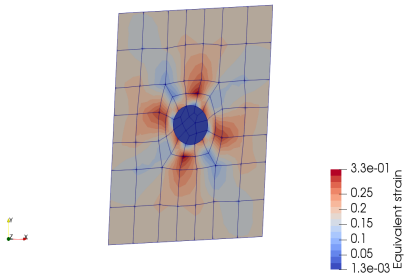

(b) Equivalent strain field for the MS model utilising a RVE_L =2 mm considering a linear boundary condition at the micro-scale.

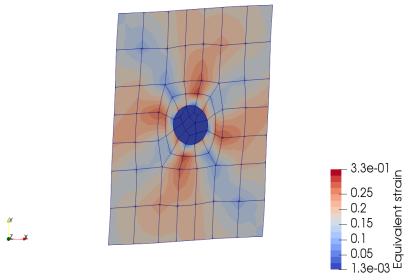

(c) Equivalent strain field for the MS model utilising a RVE_L =2 mm considering a periodic boundary condition at the micro-scale.

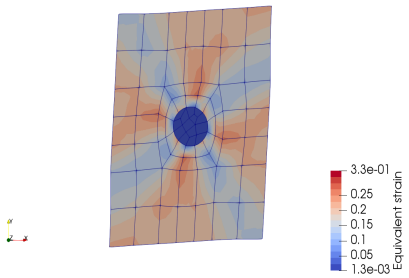

(d) Equivalent strain field for the MS model utilising a RVE_L =2 mm considering a uniform traction boundary condition at the micro-scale.

Figure 4.38: Equivalent strain field for the 4 mm notch specimen for a RVE_L =2 mm with an elastic inclusion.

Since the periodic boundary condition is the one that provides more accurate results at the macro-scale, in the next figure is shown the obtained DNS solutions for the different RVEs characteristic lengths and the periodic boundary condition solution (since a first-order homogenisation method was utilised the results will be the same for each characteristic length).

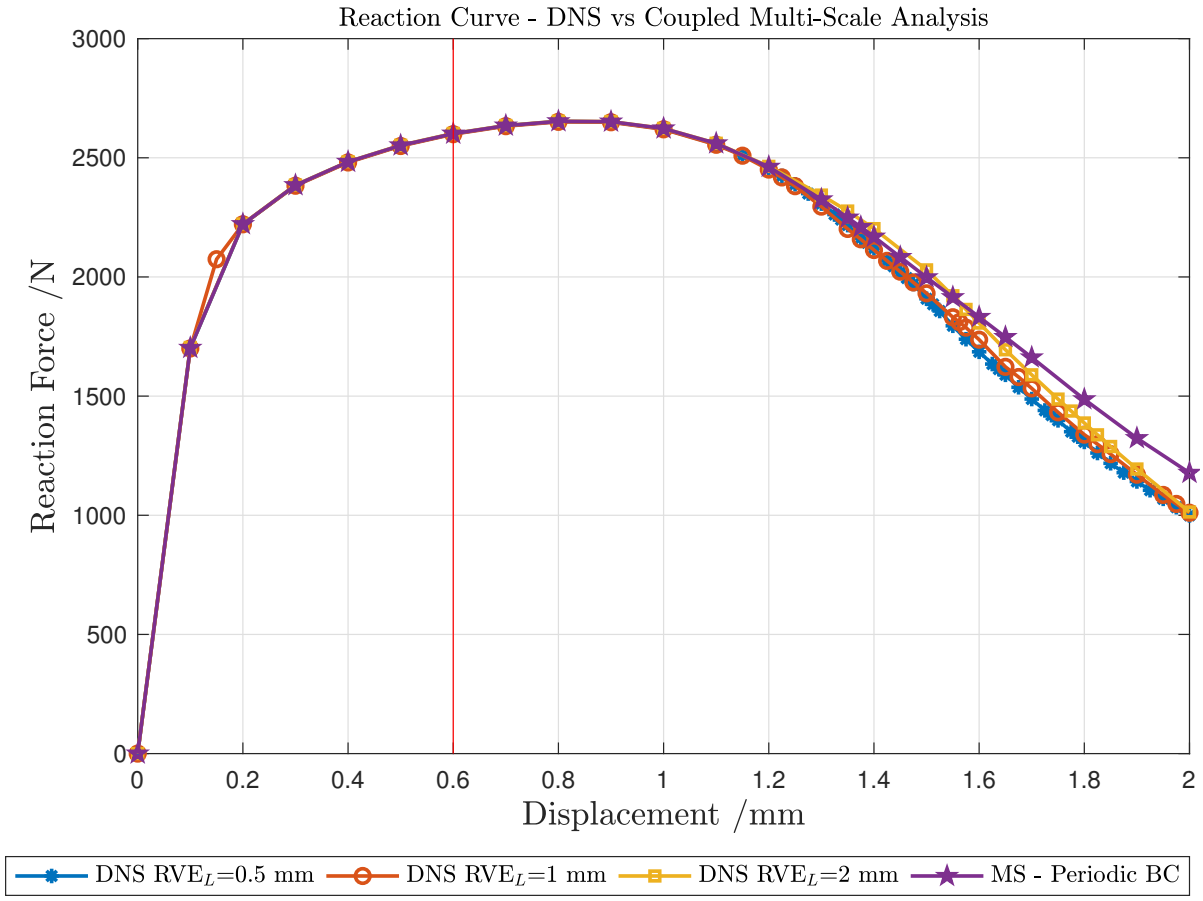

Figure 4.39: Reaction forces obtained for the different RVE characteristic lengths for the 4 mm notch specimen.

4.2.4.2 12 mm Notch

RVE with a characteristic length of 0.5 mm

The results obtained at the macro-scale, the reaction forces, can be found bellow as follows.

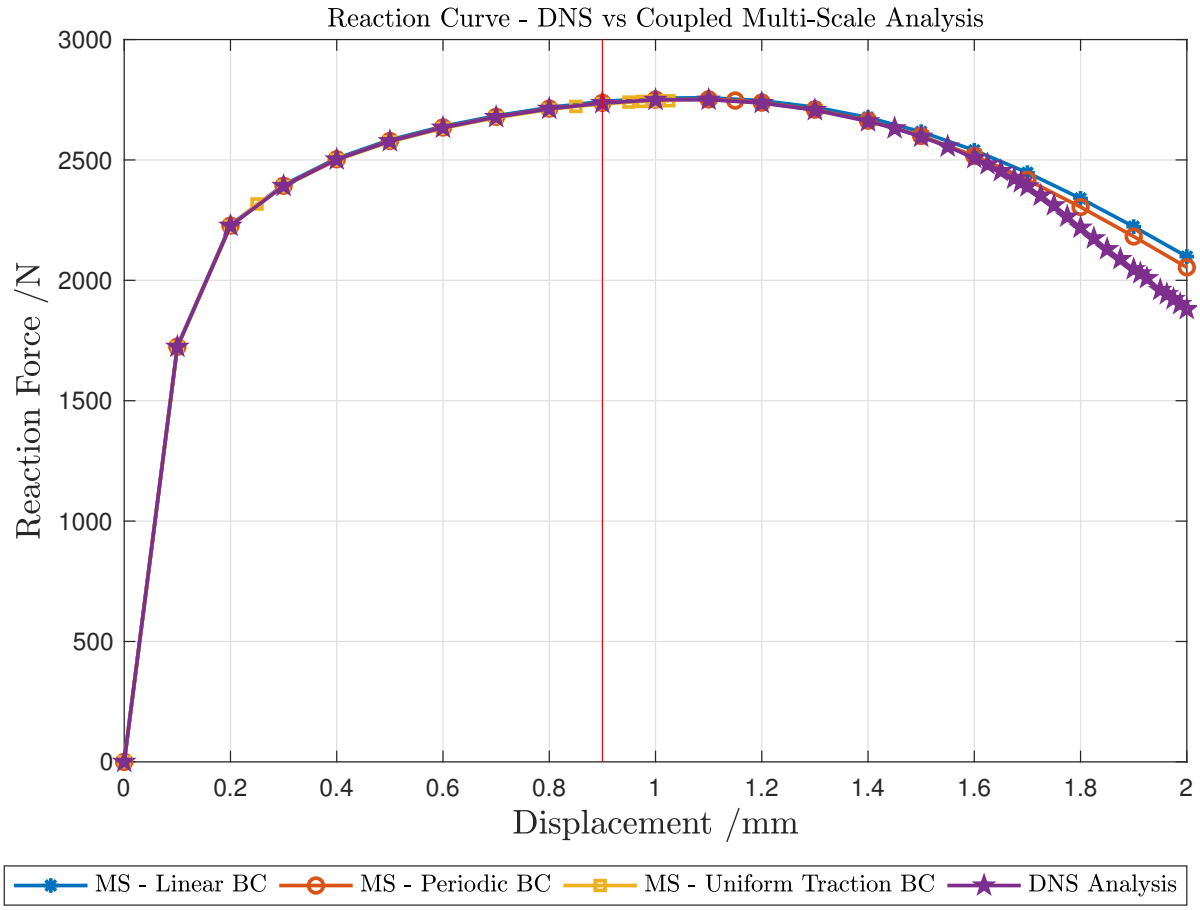

Figure 4.40: Reaction forces for the 12 mm notch specimen with a RVE with a characteristic length of 0.5 mm with an elastic inclusion.

Having already defined the RVEs that were considered, the results that were obtained at the micro-scale can be found in the next figures in terms of the effective Cauchy stress and equivalent strain fields, respectively.

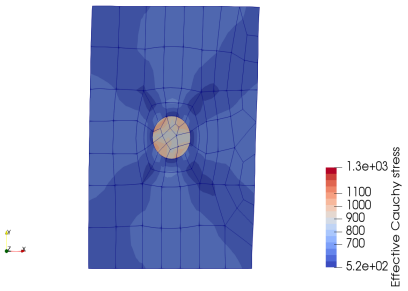

(a) Effective Cauchy stress field for the DNS model utilising a RVE_L =0.5 mm.

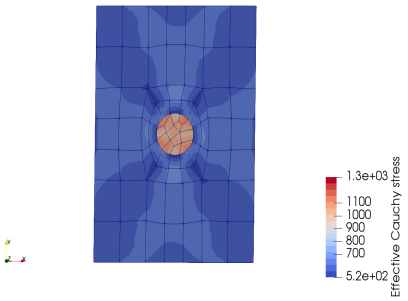

(b) Effective Cauchy stress field for the MS model utilising a RVE_L =0.5 mm considering a linear boundary condition at the micro-scale.

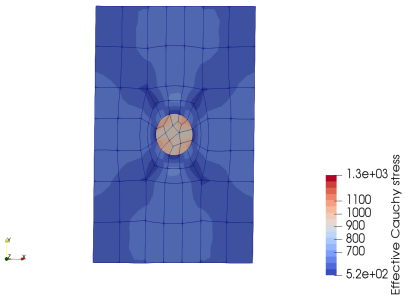

(c) Effective Cauchy stress field for the MS model utilising a RVE_L =0.5 mm considering a periodic boundary condition at the micro-scale.

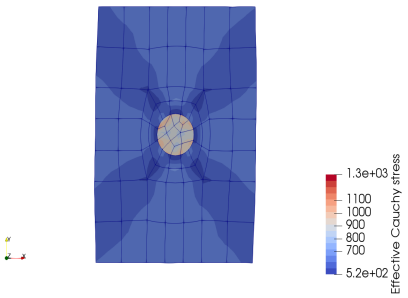

(d) Effective Cauchy stress field for the MS model utilising a RVE_L =0.5 mm considering a uniform traction boundary condition at the micro-scale.

Figure 4.41: Effective Cauchy stress field for the 12 mm notch specimen for a RVE_L =0.5 mm with an elastic inclusion.

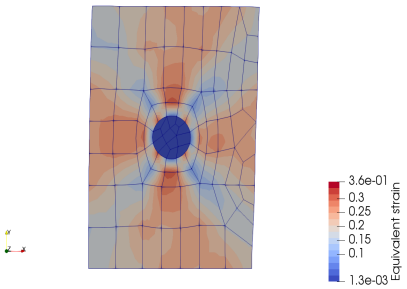

(a) Equivalent strain field for the DNS model utilising a RVE_L =0.5 mm.

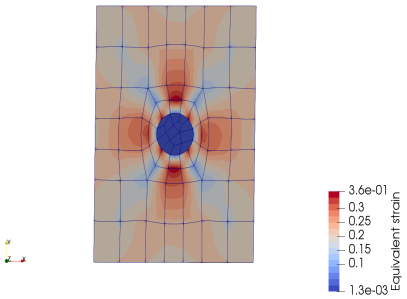

(b) Equivalent strain field for the MS model utilising a RVE_L =0.5 mm considering a linear boundary condition at the micro-scale.

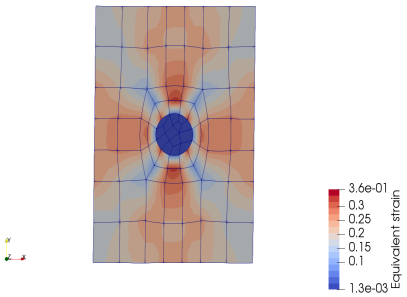

(c) Equivalent strain field for the MS model utilising a RVE_L =0.5 mm considering a periodic boundary condition at the micro-scale.

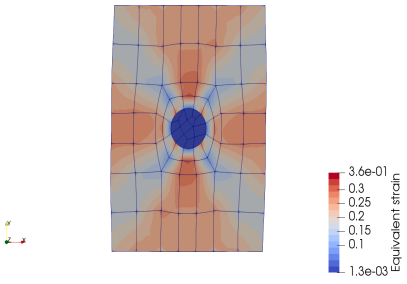

(d) Equivalent strain field for the MS model utilising a RVE_L =0.5 mm considering a uniform traction boundary condition at the micro-scale.

Figure 4.42: Equivalent strain field for the 12 mm notch specimen for a RVE_L =0.5 mm with an elastic inclusion.

RVE with a characteristic length of 1 mm

The results obtained at the macro-scale, the reaction forces, can be found bellow as follows.

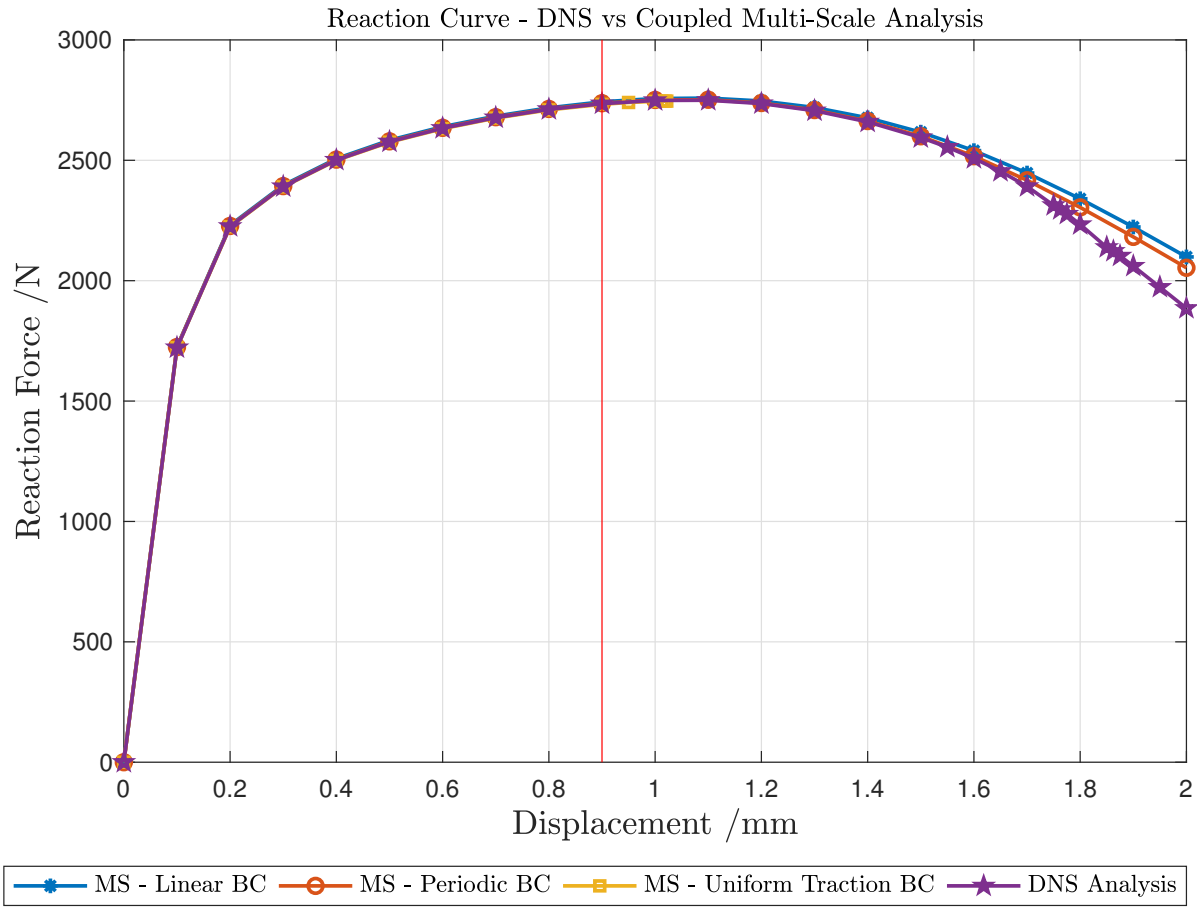

Figure 4.43: Reaction forces for the 12 mm notch specimen with a RVE with a characteristic length of 1 mm with an elastic inclusion.

Having already defined the RVEs that were considered, the results that were obtained at the micro-scale can be found in the next figures in terms of the effective Cauchy stress and equivalent strain fields, respectively.

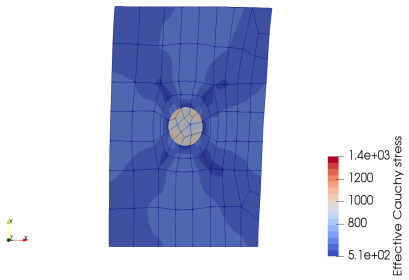

(a) Effective Cauchy stress field for the DNS model utilising a RVE_L =1 mm.

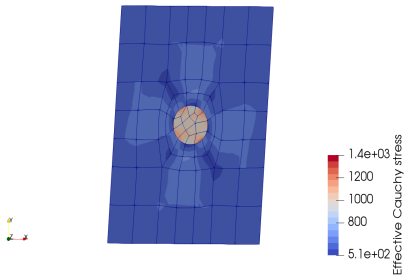

(b) Effective Cauchy stress field for the MS model utilising a RVE_L =1 mm considering a linear boundary condition at the micro-scale.

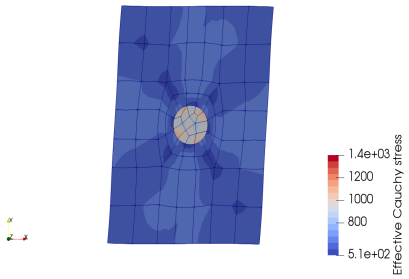

(c) Effective Cauchy stress field for the MS model utilising a RVE_L =1 mm considering a periodic boundary condition at the micro-scale.

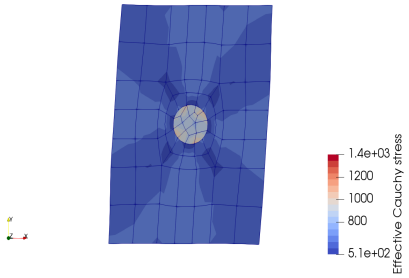

(d) Effective Cauchy stress field for the MS model utilising a RVE_L =1 mm considering a uniform traction boundary condition at the micro-scale.

Figure 4.44: Effective Cauchy stress field for the 12 mm notch specimen for a RVE_L =1 mm with an elastic inclusion.

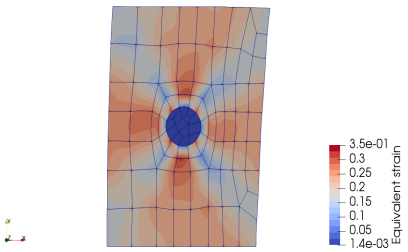

(a) Equivalent field for the DNS model utilising a RVE_L =1 mm.

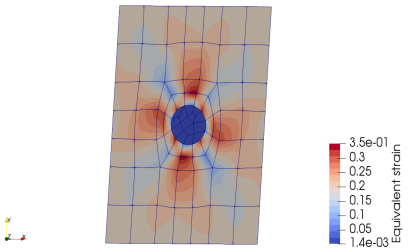

(b) Equivalent strain field for the MS model utilising a RVE_L =1 mm considering a linear boundary condition at the micro-scale.

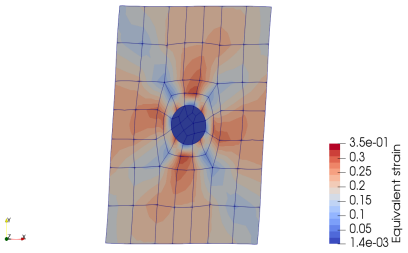

(c) Equivalent strain field for the MS model utilising a RVE_L =1 mm considering a periodic boundary condition at the micro-scale.

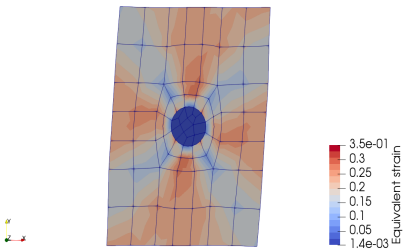

(d) Equivalent strain field for the MS model utilising a RVE_L =1 mm considering a uniform traction boundary condition at the micro-scale.

Figure 4.45: Equivalent strain field for the 12 mm notch specimen for a RVE_L =1 mm with an elastic inclusion.

RVE with a characteristic length of 2 mm

The results obtained at the macro-scale, the reaction forces, can be found bellow as follows.

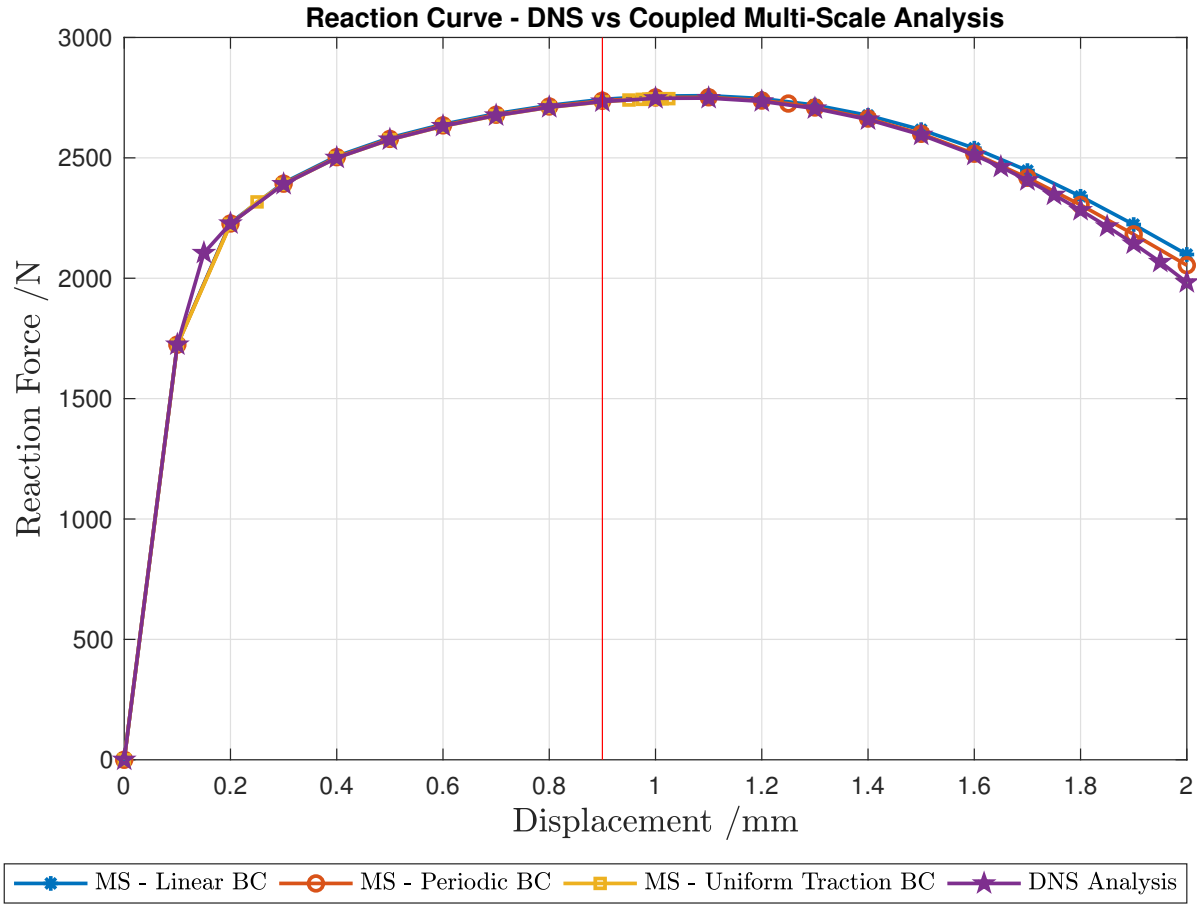

Figure 4.46: Reaction forces for the 12 mm notch specimen with a RVE with a characteristic length of 2 mm with an elastic inclusion.

Having already defined the RVEs that were considered, the results that were obtained at the micro-scale can be found in the next figures in terms of the effective Cauchy stress and equivalent strain fields, respectively.

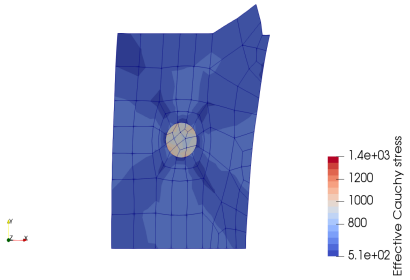

(a) Effective Cauchy stress field for the DNS model utilising a RVE_L =2 mm.

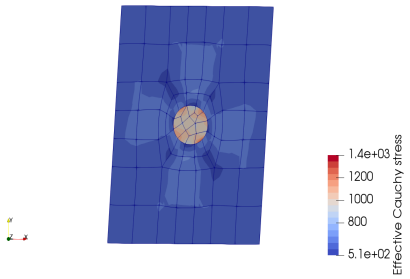

(b) Effective Cauchy stress field for the MS model utilising a RVE_L =2 mm considering a linear boundary condition at the micro-scale.

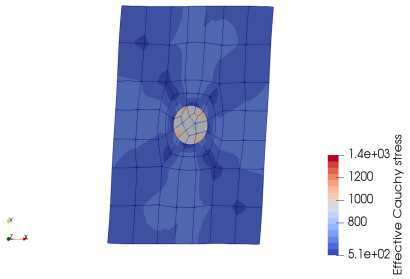

(c) Effective Cauchy stress field for the MS model utilising a RVE_L =2 mm considering a periodic boundary condition at the micro-scale.

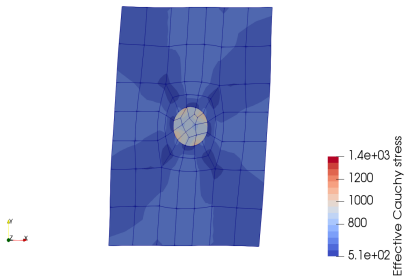

(d) Effective Cauchy stress field for the MS model utilising a RVE_L =2 mm considering a uniform traction boundary condition at the micro-scale.

Figure 4.47: Effective Cauchy stress field for the 12 mm notch specimen for a RVE_L =2 mm with an elastic inclusion.

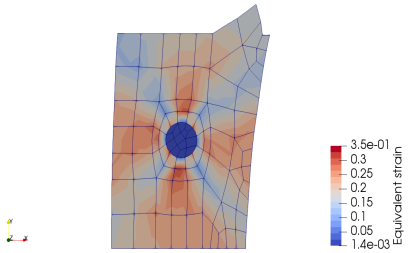

(a) Equivalent strain field for the DNS model utilising a RVE_L =2 mm.

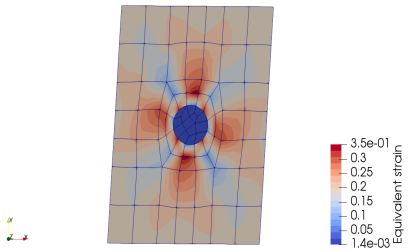

(b) Equivalent strain field for the MS model utilising a RVE_L =2 mm considering a linear boundary condition at the micro-scale.

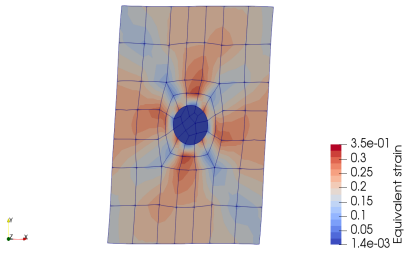

(c) Equivalent strain field for the MS model utilising a RVE_L =2 mm considering a periodic boundary condition at the micro-scale.

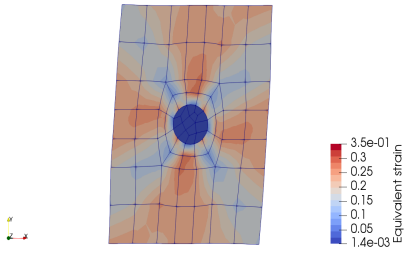

(d) Equivalent strain field for the MS model utilising a RVE_L =2 mm considering a uniform traction boundary condition at the micro-scale.

Figure 4.48: Equivalent strain field for the 12 mm notch specimen for a RVE_L =2 mm with an elastic inclusion.

Since the periodic boundary condition is the one that provides more accurate results at the macro-scale, in the next figure is shown the obtained DNS solutions for the different RVEs characteristic lengths and the periodic boundary condition solution (since a first-order homogenisation method was utilised the results will be the same for each characteristic length).

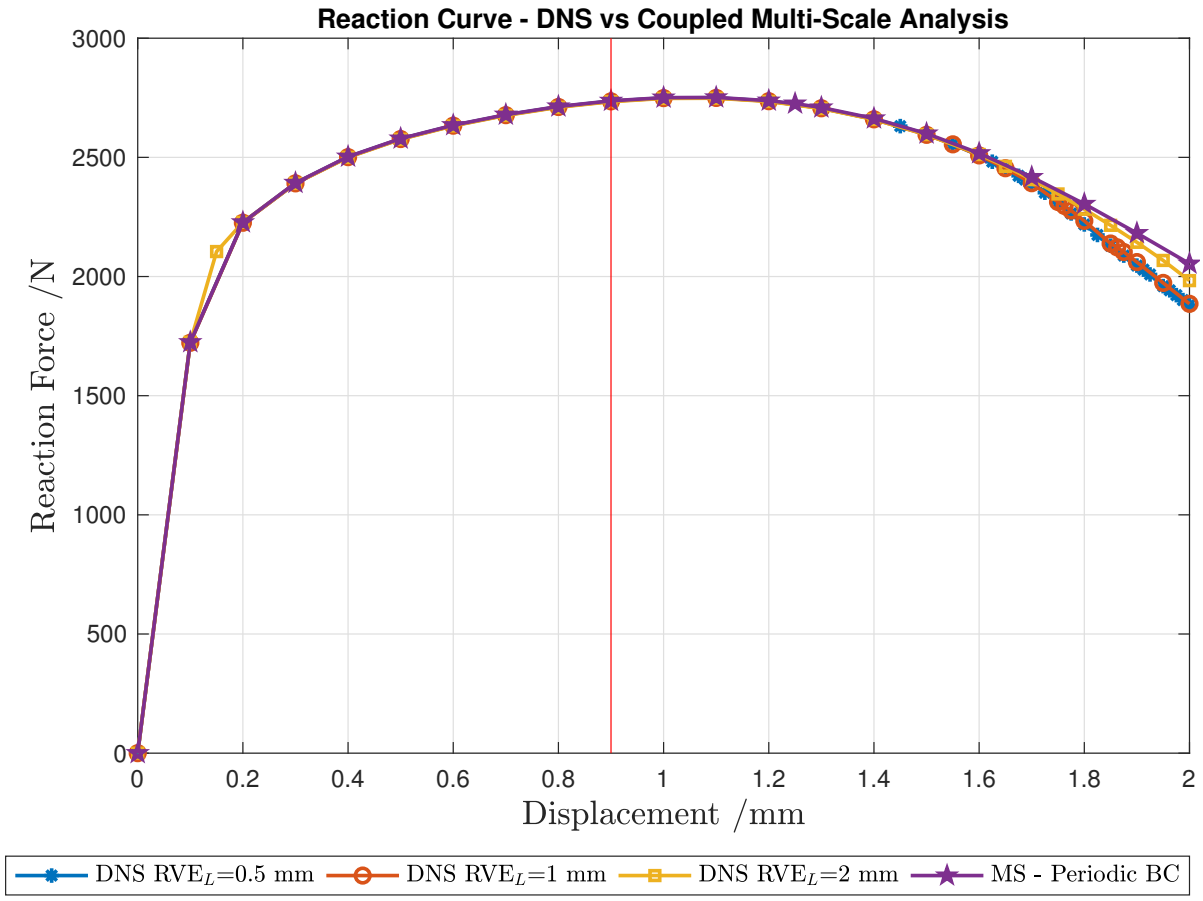

Figure 4.49: Reaction forces obtained for the different RVE characteristic lengths for the 12 mm notch specimen.

4.2.5 Results Analysis

In this case, the RVE instead of having a circular void, it had an elastic inclusion. It can be stated that, for all the characteristic lengths that have been studied, the solutions at the macro-scale (reaction forces) provided by the MS models, for all boundary conditions, fit exactly with the solutions provided by the DNS ones for both elastic and plastic regimes for both specimens of 4 and 12 mm notches. The separation between the curves only takes place during the softening regime.

In terms of micro-structural results (effective Cauchy stress and equivalent strain), once again it can be also concluded that the results obtained by a first-order homogenisation computational scheme provide results that fit with the ones that were obtained by the DNS solution.

Taking into account all information it can be stated that the principle of separation of scales hasn't been violated and that a second-order homogenisation isn't needed for this kind of solicitation and for this kind of RVE.

4.3 Conclusions

In this chapter, an assessment of the principle of separation of scales has been made for a tensile solicitation. Two different macro-scale specimens were studied and also two distinct types of RVE, being one with circular void and the other with an elastic inclusion.

It has been shown that, for the RVE with a circular void, the results provided by the DNS and MS models fit with each other until the considered representative displacement, being the periodic boundary condition the one that provides more accurate results. However, it was also shown that for both specimens, the reaction curves tend to separate but only after the representative displacement. It was also shown that for the 4 mm notch specimen the point of separation between the curves would occur for a smaller prescribed displacement, while for the 12 mm notch specimen the increase in the RVE size did not produce major differences which can be explained by the fact that the first specimen has a more pronounced notch.

For both cases, the micro-structural results (effective Cauchy stress and equivalent strain) provided by the MS models were accurate relatively to the DNS ones. Taking all results into consideration it is possible to state that the principle of separation of scales wasn't violated, and a second-order homogenisation wasn't needed.

For the RVE with an elastic inclusion, the results provided at the macro-scale by the DNS models fitted the ones provided by the MS models. Until the considered representative displacement the curves did not separate, fact which occurred only during the softening regime. In terms of micro-structural results the results provided by the MS models were accurate relatively to the DNS ones. In this case, also, the principle of separation of scales wan't violated and a second-order homogenisation wasn't needed.

Chapter 5

Assessment of the Principle of Separation of Scales of Beams Under a Bending Solicitation

This chapter aims to assess the principle of separation of scales in cases where a bending solicitation is prescribed. One will analyse the PSS taking into account a RVE with a central circular void. This study will be made for two beams with different geometric parameters. The PSS will be analysed by comparing the solutions obtained by the DNS models and the coupled multi-scale ones.

Furthermore, it will be presented a study of the influence of the utilisation of a second-order homogenisation scheme in the solutions at the micro-scale once that the coupled multi-scale model is still not implemented thus being only possible to solve the problem at the micro-scale.

Firstly one will present the geometry of the beams that have been studied, the multi-scale models that were utilised (macro and micro-scale geometries and material), the DNS models that were utilised and the numerical simulations that were made as well as the results that were obtained utilising a first-order homogenisation computational scheme. Then, it will be made a comparison between the micro-scale results provided by the DNS simulations, the first-order and the second-order homogenisation computational schemes. Lastly, some conclusions are made taking into account the results that have been obtained.

5.1 Beams' Characterization

In this study, two different types of beams have been studied depending on the ratio, $\frac{L}{\lambda}$, being L the length of the beam and λ its height. The beams that were modelled have a $\frac{L}{\lambda}$ ratio of 12.5 and 5, respectively. They are going to be designated as "Beam A" and "Beam B" from now on.

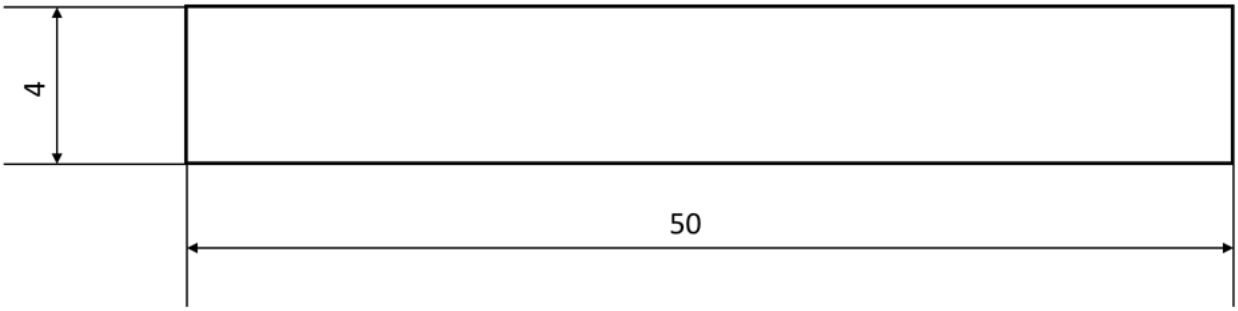

(a) Beam A geometry.

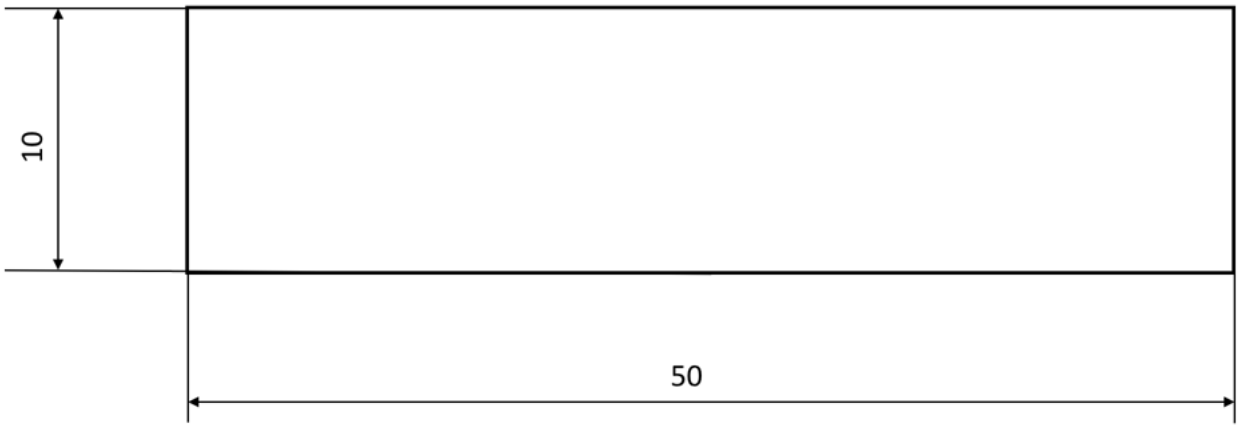

(b) Beam B geometry.

Figure 5.1: Beams that were studied.

5.2 Material Definition

The material that was considered in both cases was the aluminium alloy 2024-T351 already introduced in Section 4.1.2.

5.3 Multi-Scale Model

The multi-scale model can be divided into two distinct models. The macro-scale model and the micro-scale one. The multi-scale models that have been used are presented below.

5.3.1 Macro-Scale Meshes

The macro-scale meshes were obtained by means of an auxiliary software, GiD®. The type of elements that were utilised were a 8-noded quadratic element. The macro-scale meshes can be found below. The elements that are indicated are the ones that are going to be analysed later. A resume of the mesh properties can be found below in the following tables.

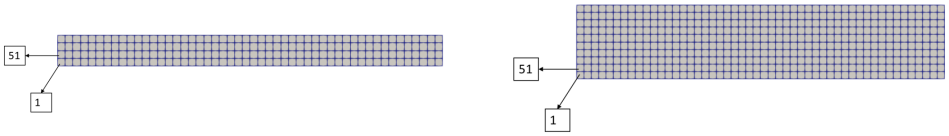

(a) Beam A macro-scale mesh.

(b) Beam B macro-scale mesh.

Figure 5.2: Macro-scales meshes of the samples that have been studied.

Table 5.1: Macro-scale mesh properties for the Beam A.

Number of Elements	Number of Nodes
200	709

Table 5.2: Macro-scale mesh properties for the Beam B.

Number of Elements	Number of Nodes
500	1621

5.3.2 Micro-Scale Mesh: Definition of the RVEs' Properties

The RVE and its mesh have already been presented in subsubsection 4.1.3.2 therefore they are not going to be repeated in this section.

5.4 DNS Models

Having introduced the samples geometry and the micro-scale mesh it is now possible to define the DNS models that have been utilised. As it has already been stated in the introductory chapters of the present report, a DNS simulation requires an explicitly modelation of the microsctructure of the material. The models that are going to be presented were made with the aid of the pre-processing software GiD® and are presented below, for the 4 and 12 mm notch samples, respectively. The highlighted RVEs are the ones that were compared with results from the coupled multi-scale models.

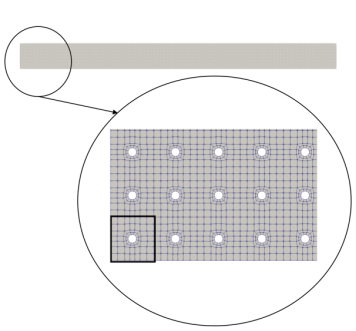

(a) Close up of the notch zone of the DNS model of the Beam A, using a RVE_L =0.5 mm.

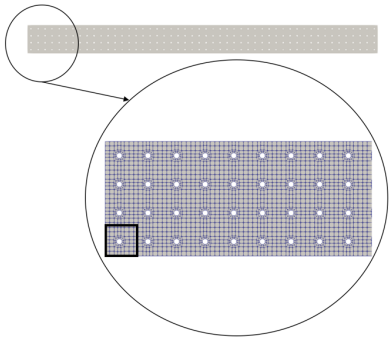

(b) Close up of the notch zone of the DNS model of the Beam A, using a RVE_L =1 mm.

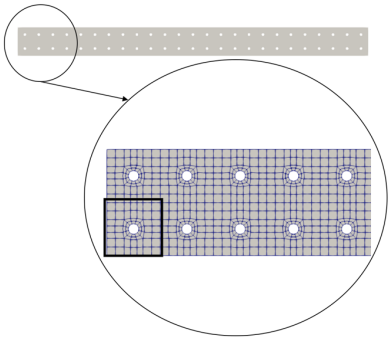

(c) Close up of the notch zone of the DNS model of the Beam A, using a RVE_L =2 mm.

Figure 5.3: Close up of the notch zone of the different DNS models for the Beam A.

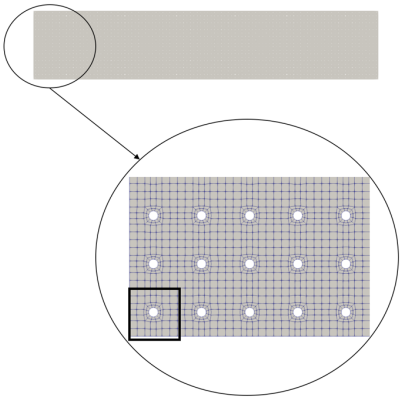

(a) Close up of the notch zone of the DNS model of the Beam B, using a RVE_L =0.5 mm.

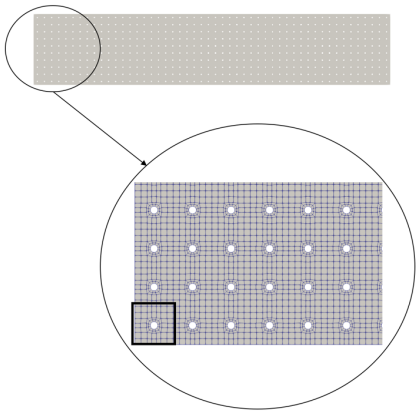

(b) Close up of the notch zone of the DNS model of the Beam B, using a RVE_L =1 mm.

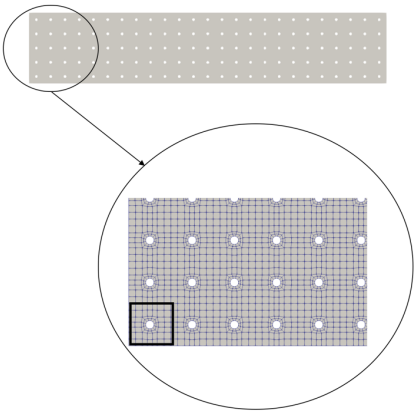

(c) Close up of the notch zone of the DNS model of the Beam B, using a RVE_L =2 mm.

Figure 5.4: Close up of the notch zone of the different DNS models for the Beam B.

A resume of the DNS mesh properties can be found below on the following tables.

Table 5.3: DNS meshes properties for the Beam A.

RVE_L	Number of Elements	Number of Nodes
0.5	51200	163913
1	12800	41357
2	3200	10529

For all different types of meshes, the element type that was utilised was a 8-noded quadratic element with reduced integration.

Table 5.4: DNS meshes properties for the Beam B.

RVE_L	Number of Elements	Number of Nodes
0.5	128000	407681
1	32000	102341
2	8000	25796

5.5 Numerical Simulations

Having already defined the properties of the multi-scale models as of the DNS ones, one can define the numerical simulations parameters. For every numerical simulation, it was prescribed a rotation of 120 degrees in the "right tip" of the macro-scale meshes as well as of the DNS ones. The prescribed rotation was divided in 40 increments for the case of the Beam A and in 80 increments in the case of the Beam B. This disparity happened due to increment cuts in the solution of the multi-scale model. The boundary conditions that were applied at the macro-scale were only the horizontal displacements being blocked in the "left tip" of the models. For the coupled multi-scale, the simulations were repeated for each micro-scale boundary condition (linear, periodic and uniform traction). All simulations were made considering a plane-strain case.

5.6 Results Obtained Utilising a First-Order Homogenization Method

In the following section, the results that were obtained are going to be presented. The presentation of the results is going to be made by separating the two scales, this is:

- Firstly, the results that are going to be compared are the results obtained at the macro-scale, this is, the reaction bending moment depending on the prescribed rotation. Thus, those curves are going to be presented taking into account the results provided by DNS model and the FE^2 ones (for each boundary condition) and for each RVE characteristic length;

- At the micro-scale one will present the Cauchy effective stress and the equivalent strain fields in the same conditions as above. It is important to note that this comparison has to be made in a qualitative way, once that it is impossible to directly relate a RVE in the DNS model to a RVE associated with a Gauss point in the FE^2 model. The RVEs that are going to be compared to the DNS ones (see Figure 5.3 and Figure 5.4) are linked with the Gauss points of the elements that are indicated in Figure 5.2. Since that the DNS RVEs are the same for both cases of the Beam A and Beam B the chosen RVEs of the MS analysis will also be the same for both cases. The Gauss points that were analysed were chosen by their proximity (in terms of coordinates) to the centroid of the

corresponding RVE that was analysed in the DNS model. Thus, the chosen Gauss points were the first and second Gauss points of the element number one and the first Gauss point of the element number 51 for the cases of the RVE_L =0.5 mm, RVE_L =1 mm and RVE_L ==2 mm respectively.

- The results' analysis will be made until a representative rotation, this is, the rotation that occurred until the point where began to occur localization of deformation. For the Beams A, the representative rotation is of 48 degrees and for the Beams B, it is of 36 degrees. For the results at the macro-scale, the representative rotations are demonstrated by a vertical red line.

5.6.1 Beam A

RVE with a characteristic length of 0.5 mm

The results obtained at the macro-scale, the reaction bending moment, can be found bellow as follows.

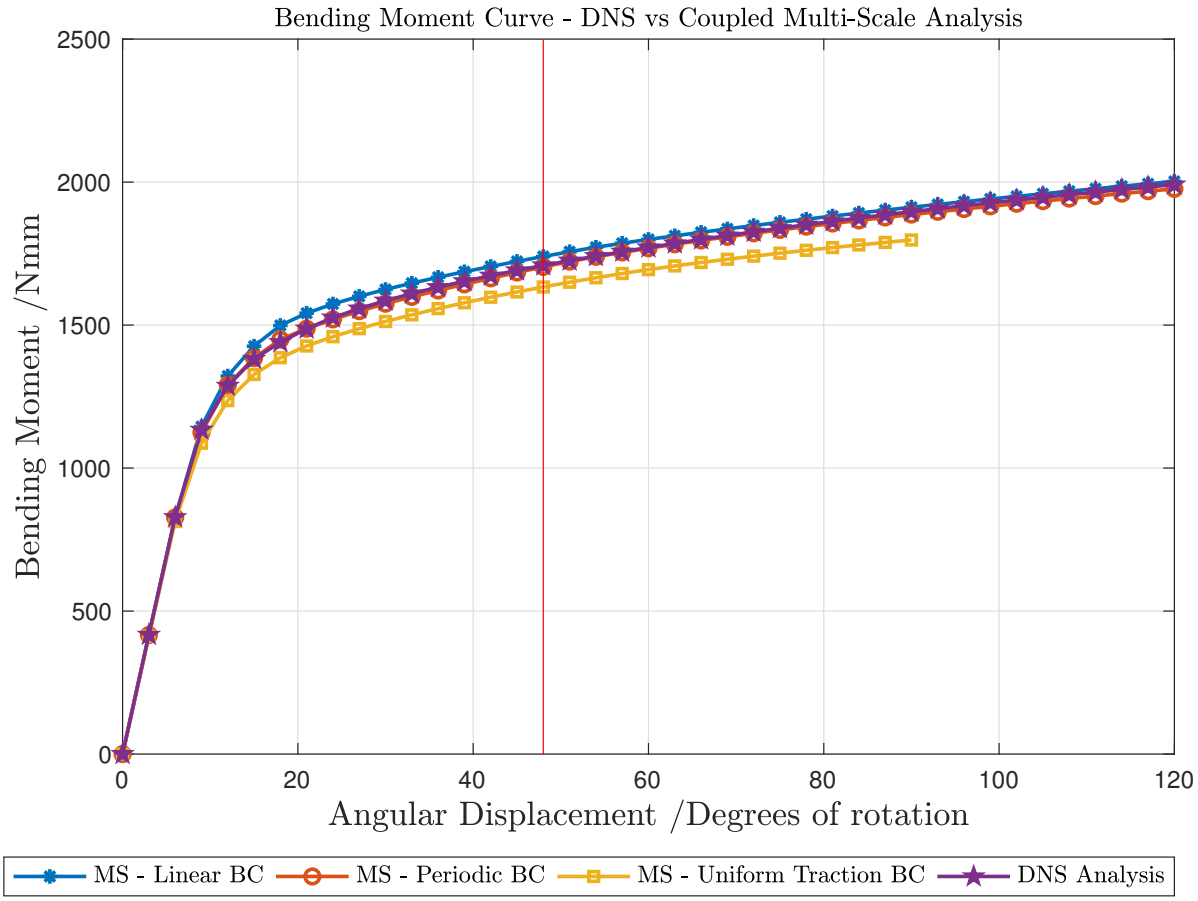

Figure 5.5: Reaction bending moment for the Beam A models with a RVE with a characteristic length of 0.5 mm with a concentric circular void.

Having already defined the RVEs that were considered, the results that were obtained at the micro-scale can be found in the next figures in terms of the effective Cauchy stress and equivalent strain, respectively.

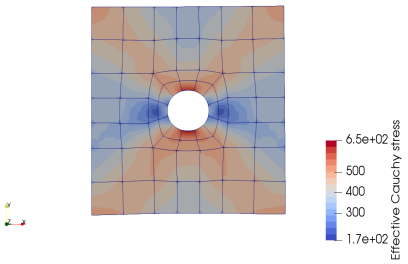

(a) Effective Cauchy stress field for the DNS model utilising a RVE_L =0.5 mm.

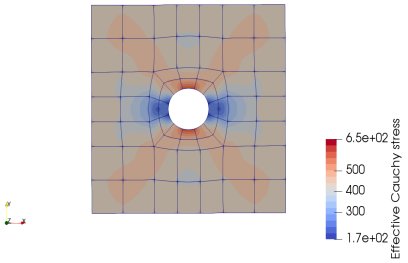

(b) Effective Cauchy stress field for the MS model utilising a RVE_L =0.5 mm considering a linear boundary condition at the micro-scale.

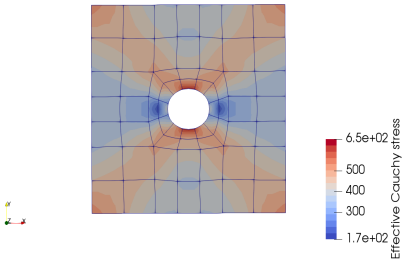

(c) Effective Cauchy stress field for the MS model utilising a RVE_L =0.5 mm considering a periodic boundary condition at the micro-scale.

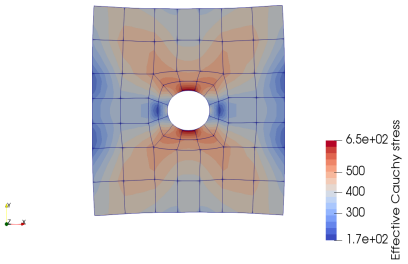

(d) Effective Cauchy stress field for the MS model utilising a RVE_L =0.5 mm considering a uniform traction boundary condition at the micro-scale.

Figure 5.6: Effective Cauchy stress field for the utilised Beam A models for a RVE_L =0.5 mm with a concentric circular void.

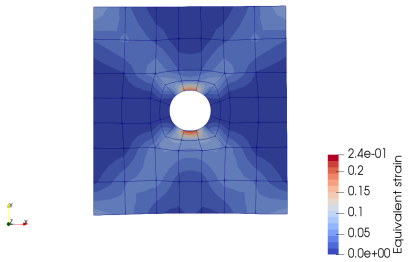

(a) Equivalent strain field for the DNS model utilising a RVE_L =0.5 mm.

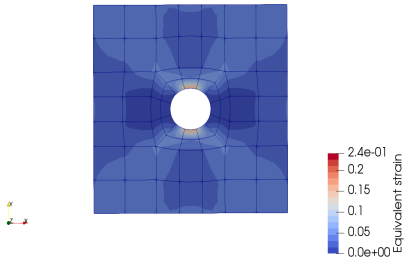

(b) Equivalent strain field for the MS model utilising a RVE_L =0.5 mm considering a linear boundary condition at the micro-scale.

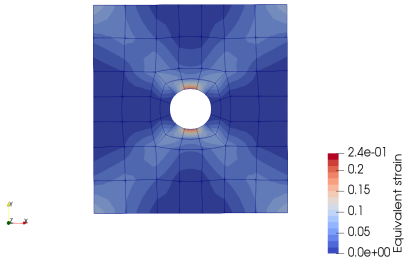

(c) Equivalent strain field for the MS model utilising a RVE_L =0.5 mm considering a periodic boundary condition at the micro-scale.

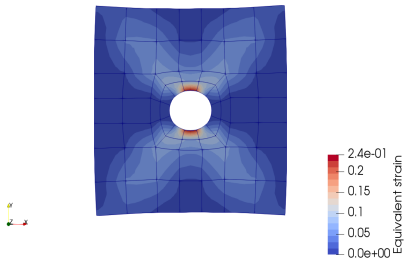

(d) Equivalent strain field for the MS model utilising a RVE_L =0.5 mm considering a uniform traction boundary condition at the micro-scale.

Figure 5.7: Equivalent strain field for the utilised Beam A models for a RVE_L =0.5 mm with a concentric circular void.

RVE with a characteristic length of 1 mm

The results obtained at the macro-scale, the reaction bending moment, can be found bellow as follows.

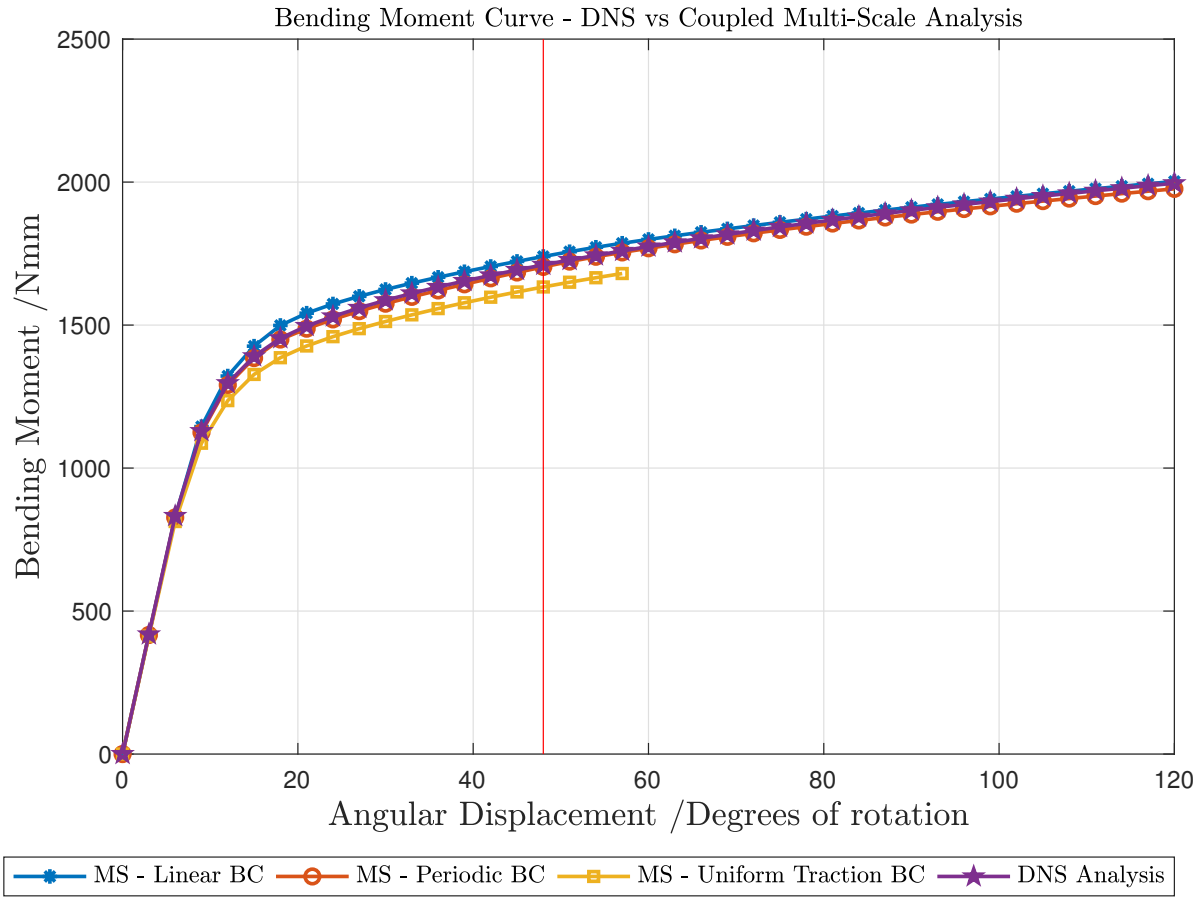

Figure 5.8: Reaction bending moment for the Beam A models with a RVE with a characteristic length of 1 mm with a concentric circular void.

Having already defined the RVEs that were considered, the results that were obtained at the micro-scale can be found in the next figures in terms of the effective Cauchy stress and equivalent strain, respectively.

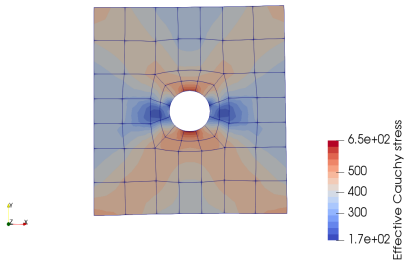

(a) Effective Cauchy stress field for the DNS model utilising a RVE_L =1 mm.

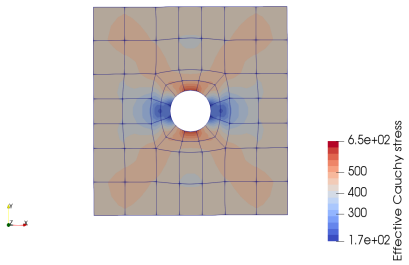

(b) Effective Cauchy stress field for the MS model utilising a RVE_L =1 mm considering a linear boundary condition at the micro-scale.

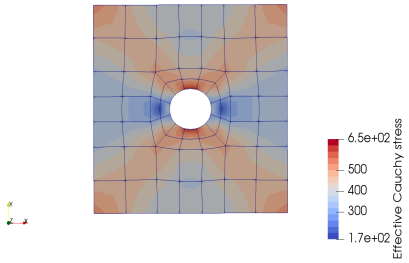

(c) Effective Cauchy stress field for the MS model utilising a RVE_L =1 mm considering a periodic boundary condition at the micro-scale.

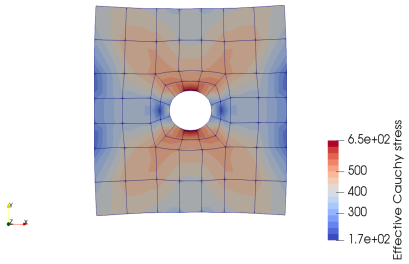

(d) Effective Cauchy stress field for the MS model utilising a RVE_L =1 mm considering a uniform traction boundary condition at the micro-scale.

Figure 5.9: Effective Cauchy stress field for the utilised Beam A models for a RVE_L =1 mm with a concentric circular void.

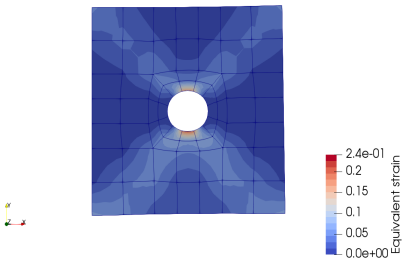

(a) Equivalent field for the DNS model utilising a RVE_L =1 mm.

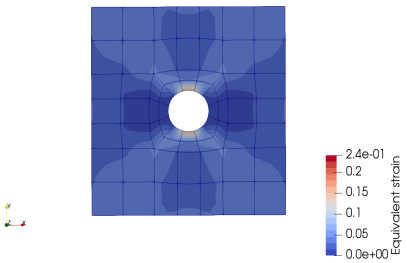

(b) Equivalent strain field for the MS model utilising a RVE_L =1 mm considering a linear boundary condition at the micro-scale.

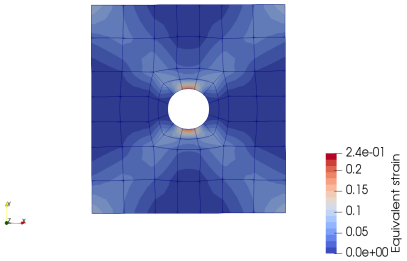

(c) Equivalent strain field for the MS model utilising a RVE_L =1 mm considering a periodic boundary condition at the micro-scale.

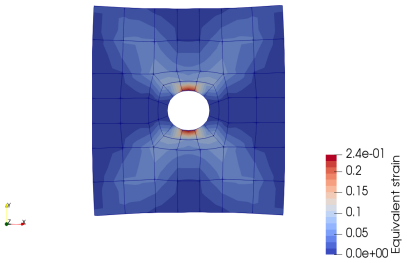

(d) Equivalent strain field for the MS model utilising a RVE_L =1 mm considering a uniform traction boundary condition at the micro-scale.

Figure 5.10: Equivalent strain field for the utilised Beam A models for a RVE_L =1 mm with a concentric circular void.

RVE with a characteristic length of 2 mm

The results obtained at the macro-scale, the reaction bending moment, can be found bellow as follows.

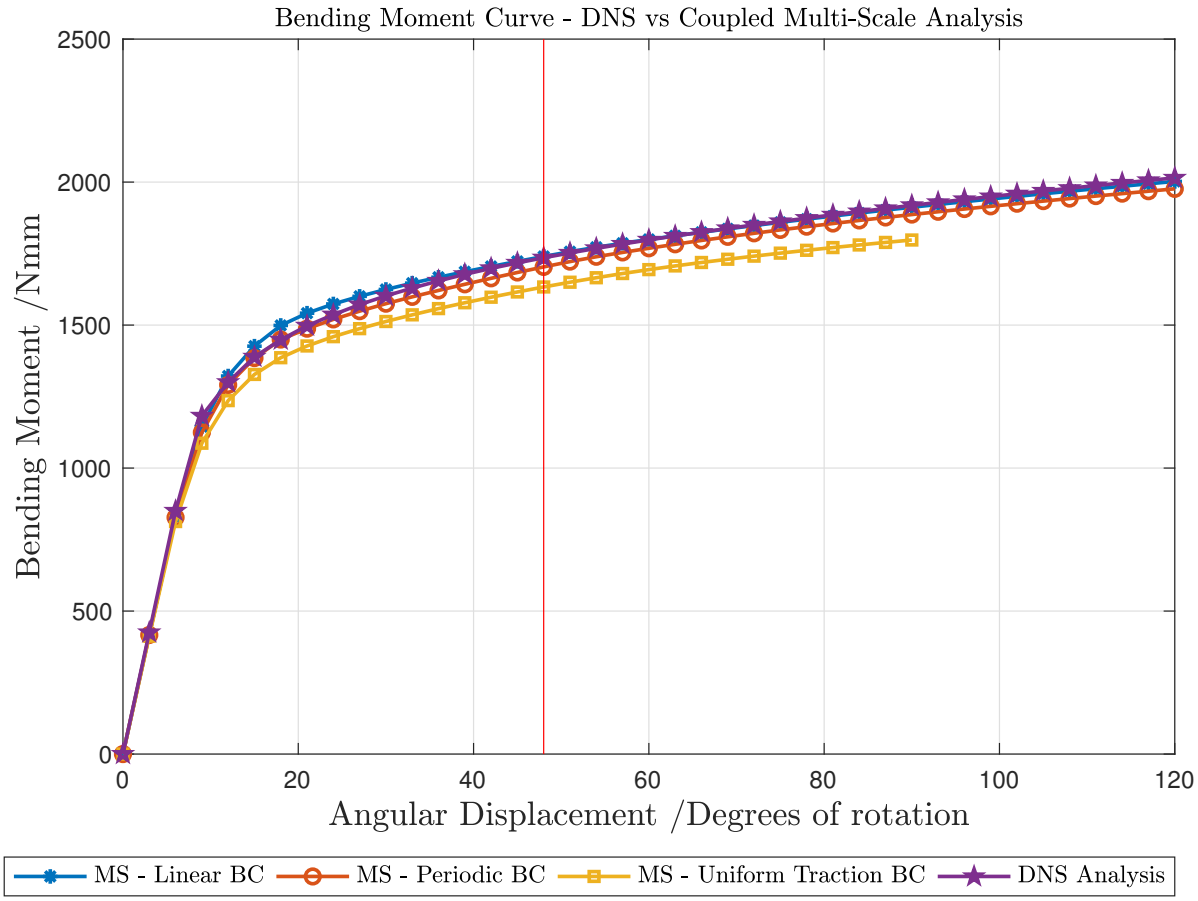

Figure 5.11: Reaction bending moment for the Beam A models with a RVE with a characteristic length of 2 mm with a concentric circular void.

Having already defined the RVEs that were considered, the results that were obtained at the micro-scale can be found in the next figures in terms of the effective Cauchy stress and equivalent strain, respectively.

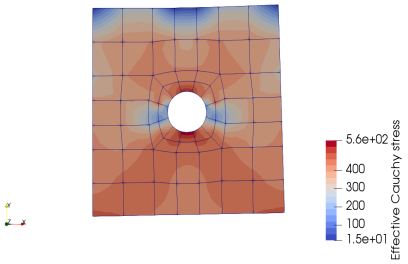

(a) Effective Cauchy stress field for the DNS model utilising a RVE_L =2 mm.

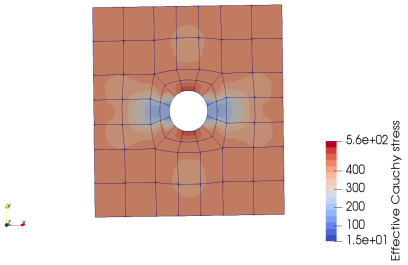

(b) Effective Cauchy stress field for the MS model utilising a RVE_L =2 mm considering a linear boundary condition at the micro-scale.

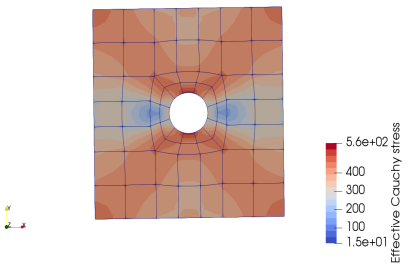

(c) Effective Cauchy stress field for the MS model utilising a RVE_L =2 mm considering a periodic boundary condition at the micro-scale.

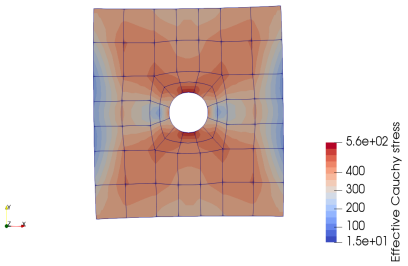

(d) Effective Cauchy stress field for the MS model utilising a RVE_L =2 mm considering a uniform traction boundary condition at the micro-scale.

Figure 5.12: Effective Cauchy stress field for the utilised Beam A models for a RVE_L =2 mm with a concentric circular void.

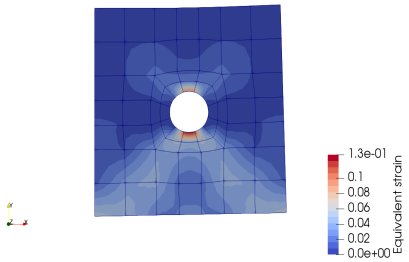

(a) Equivalent strain field for the DNS model utilising a RVE_L =2 mm.

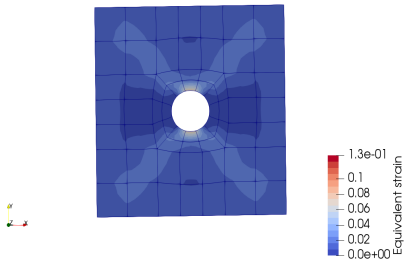

(b) Equivalent strain field for the MS model utilising a RVE_L =2 mm considering a linear boundary condition at the micro-scale.

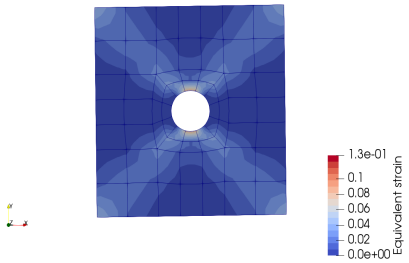

(c) Equivalent strain field for the MS model utilising a RVE_L =2 mm considering a periodic boundary condition at the micro-scale.

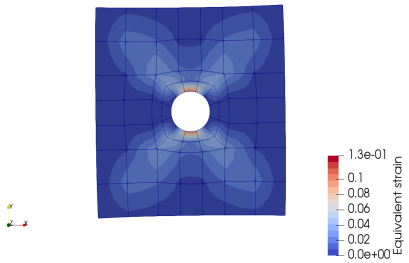

(d) Equivalent strain field for the MS model utilising a RVE_L =2 mm considering a uniform traction boundary condition at the micro-scale.

Figure 5.13: Equivalent strain field for the utilised Beam A models for a RVE_L =2 mm with a concentric circular void.

Since the periodic boundary condition is the one that provides more accurate results at the macro-scale, in the next figure is shown the obtained DNS solutions for the different RVEs characteristic lengths and the periodic boundary condition solution (since a first-order homogenisation method was utilised the results will be the same for each characteristic length).

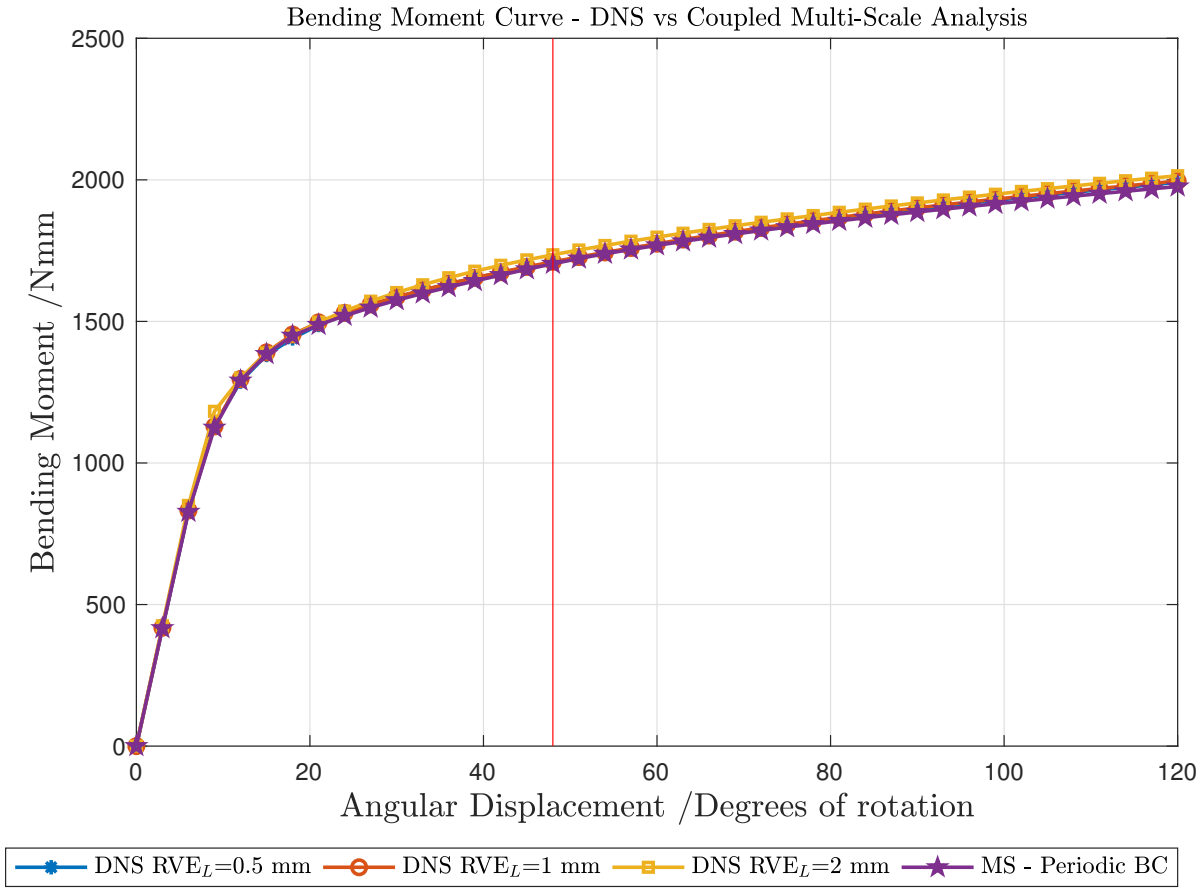

Figure 5.14: Reaction forces obtained for the different RVE characteristic lengths for the Beam A.

5.6.2 Beam B

RVE with a characteristic length of 0.5 mm

The results obtained at the macro-scale, the reaction bending moment, can be found bellow as follows.

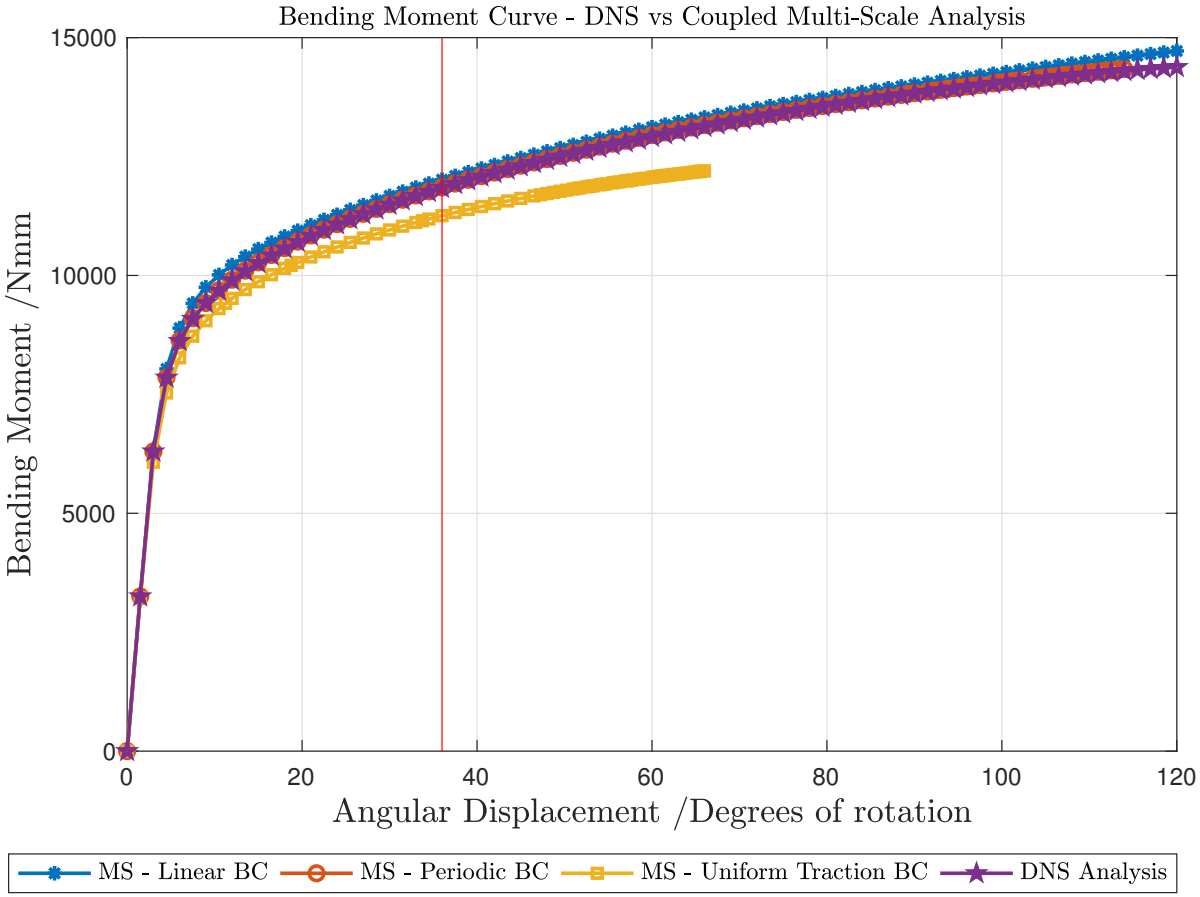

Figure 5.15: Reaction bending moment for the Beam B models with a RVE with a characteristic length of 0.5 mm with a concentric circular void.

Having already defined the RVEs that were considered, the results that were obtained at the micro-scale can be found in the next figures in terms of the effective Cauchy stress and equivalent strain, respectively.

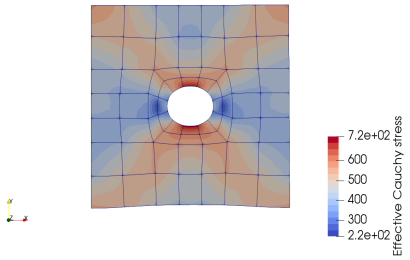

(a) Effective Cauchy stress field for the DNS model utilising a RVE_L =0.5 mm.

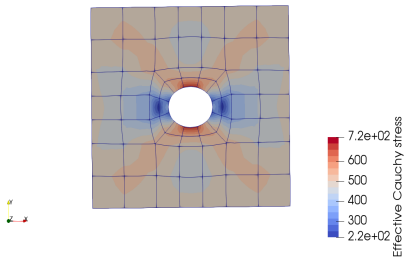

(b) Effective Cauchy stress field for the MS model utilising a RVE_L =0.5 mm considering a linear boundary condition at the micro-scale.

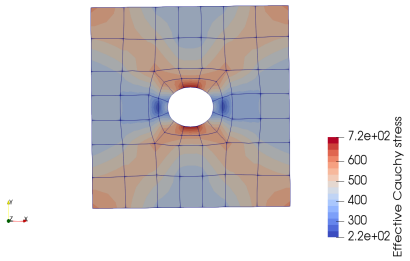

(c) Effective Cauchy stress field for the MS model utilising a RVE_L =0.5 mm considering a periodic boundary condition at the micro-scale.

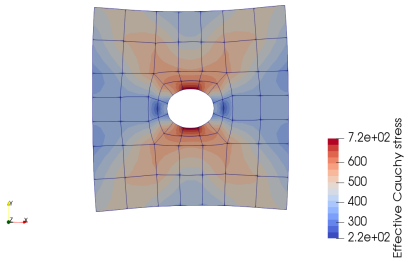

(d) Effective Cauchy stress field for the MS model utilising a RVE_L =0.5 mm considering a uniform traction boundary condition at the micro-scale.

Figure 5.16: Effective Cauchy stress field for the utilised Beam B models for a RVE_L =0.5 mm with a concentric circular void.

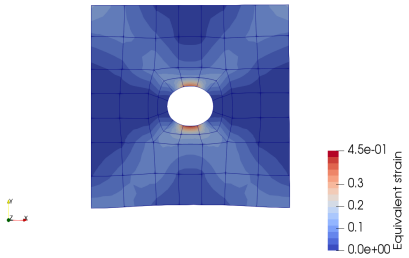

(a) Equivalent strain field for the DNS model utilising a RVE_L =0.5 mm.

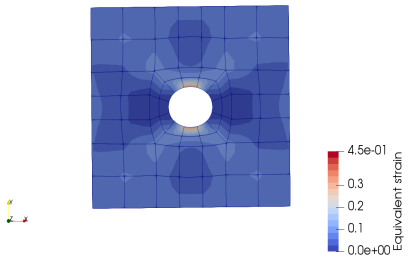

(b) Equivalent strain field for the MS model utilising a RVE_L =0.5 mm considering a linear boundary condition at the micro-scale.

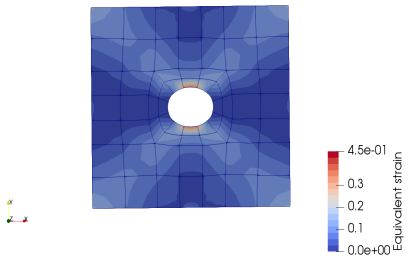

(c) Equivalent strain field for the MS model utilising a RVE_L =0.5 mm considering a periodic boundary condition at the micro-scale.

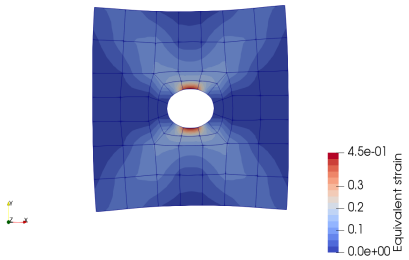

(d) Equivalent strain field for the MS model utilising a RVE_L =0.5 mm considering a uniform traction boundary condition at the micro-scale.

Figure 5.17: Equivalent strain field for the utilised Beam B models for a RVE_L =0.5 mm with a concentric circular void.

RVE with a characteristic length of 1 mm

The results obtained at the macro-scale, the reaction bending moment, can be found bellow as follows.

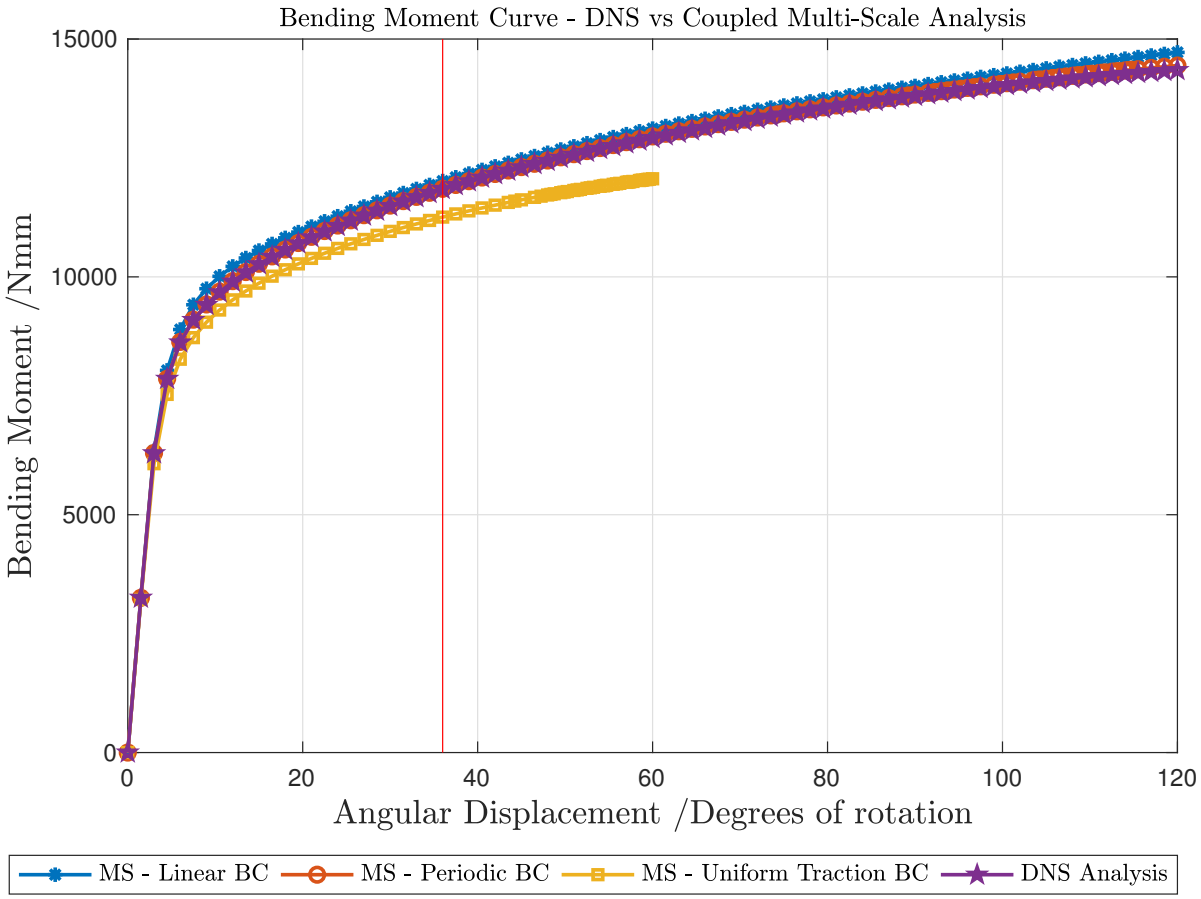

Figure 5.18: Reaction bending moment for the Beam B models with a RVE with a characteristic length of 1 mm with a concentric circular void.

Having already defined the RVEs that were considered, the results that were obtained at the micro-scale can be found in the next figures in terms of the effective Cauchy stress and equivalent strain, respectively.

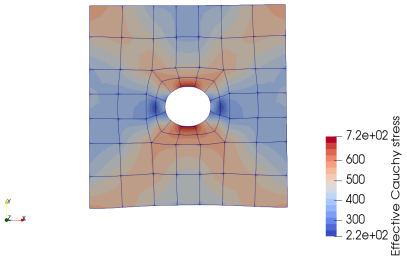

(a) Effective Cauchy stress field for the DNS model utilising a RVE_L =1 mm.

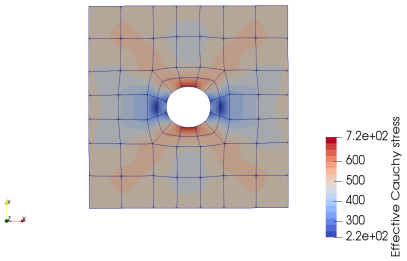

(b) Effective Cauchy stress field for the MS model utilising a RVE_L =1 mm considering a linear boundary condition at the micro-scale.

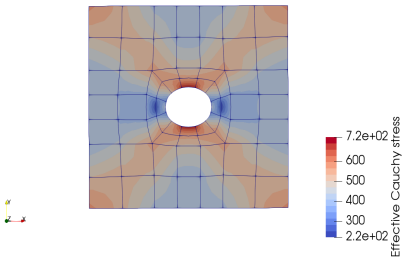

(c) Effective Cauchy stress field for the MS model utilising a RVE_L =1 mm considering a periodic boundary condition at the micro-scale.

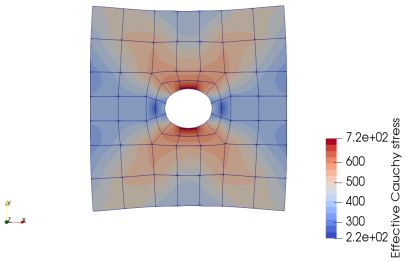

(d) Effective Cauchy stress field for the MS model utilising a RVE_L =1 mm considering a uniform traction boundary condition at the micro-scale.

Figure 5.19: Effective Cauchy stress field for the utilised Beam B models for a RVE_L =1 mm with a concentric circular void.

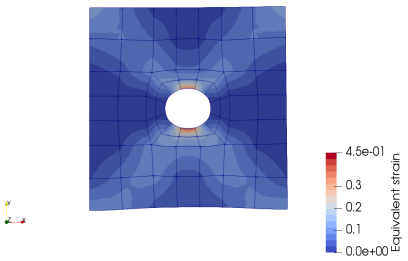

(a) Equivalent strain field for the DNS model utilising a RVE_L =1 mm.

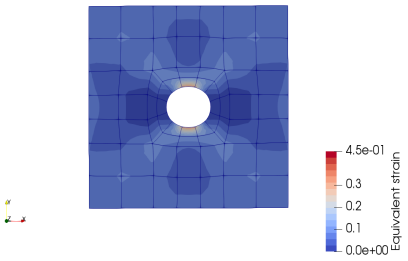

(b) Equivalent strain field for the MS model utilising a RVE_L =1 mm considering a linear boundary condition at the micro-scale.

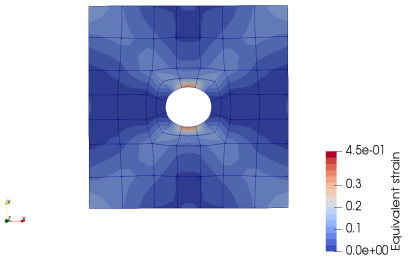

(c) Equivalent strain field for the MS model utilising a RVE_L =1 mm considering a periodic boundary condition at the micro-scale.

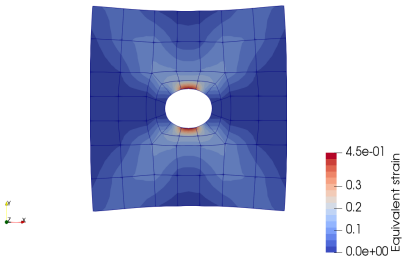

(d) Equivalent strain field for the MS model utilising a RVE_L =1 mm considering a uniform traction boundary condition at the micro-scale.

Figure 5.20: Equivalent strain field for the utilised Beam B models for a RVE_L =1 mm with a concentric circular void.

RVE with a characteristic length of 2 mm

The results obtained at the macro-scale, the reaction bending moment, can be found bellow as follows.

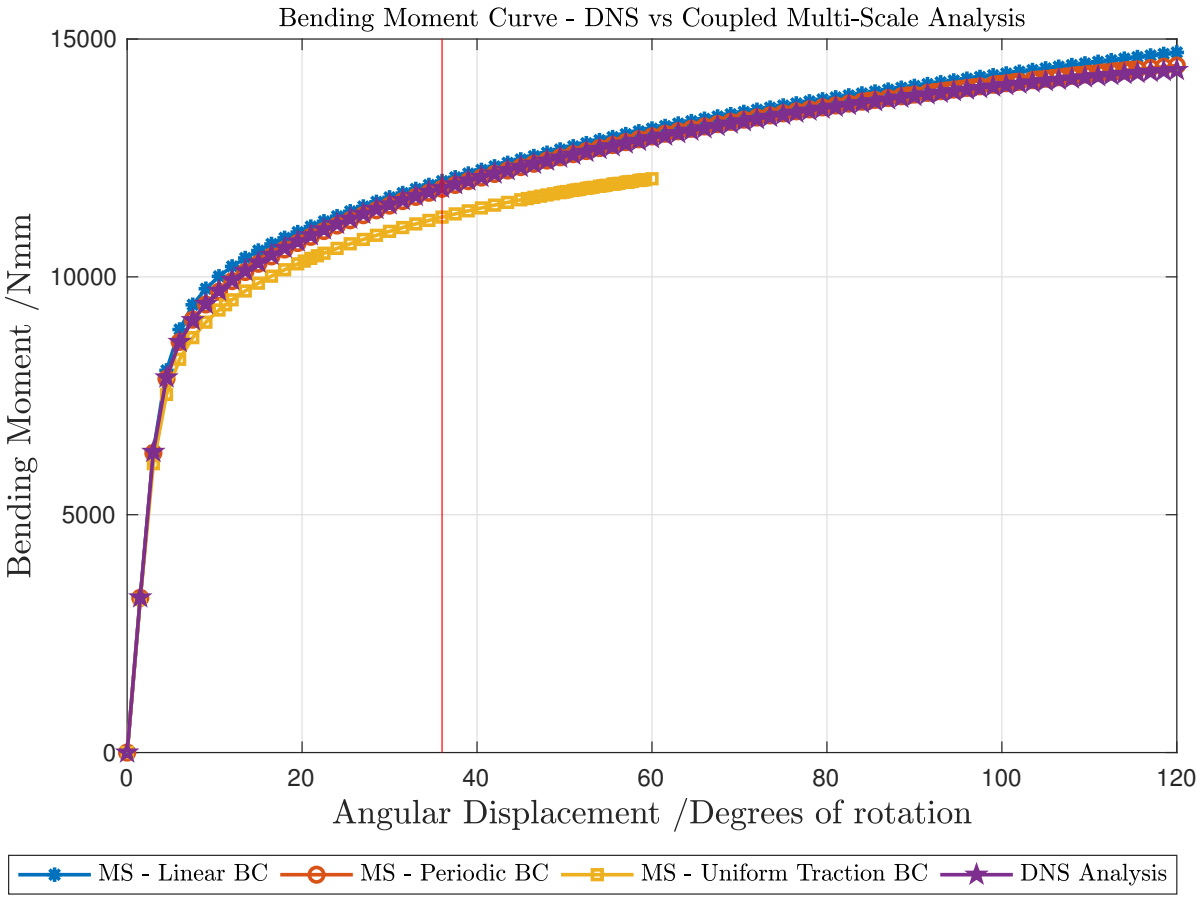

Figure 5.21: Reaction bending moment for the Beam B models with a RVE with a characteristic length of 2 mm with a concentric circular void.

Having already defined the RVEs that were considered, the results that were obtained at the micro-scale can be found in the next figures in terms of the effective Cauchy stress and equivalent strain, respectively.

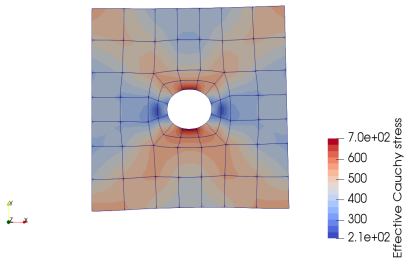

(a) Effective Cauchy stress field for the DNS model utilising a RVE_L =2 mm.

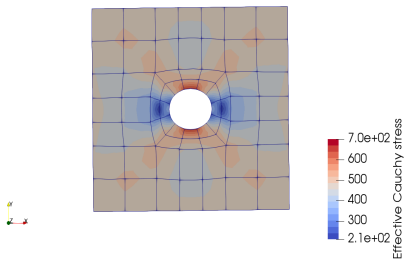

(b) Effective Cauchy stress field for the MS model utilising a RVE_L =2 mm considering a linear boundary condition at the micro-scale.

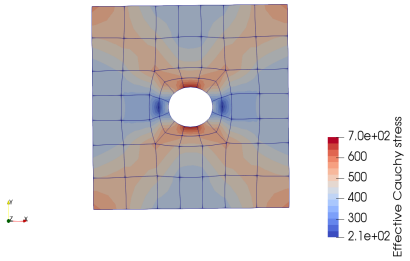

(c) Effective Cauchy stress field for the MS model utilising a RVE_L =2 mm considering a periodic boundary condition at the micro-scale.

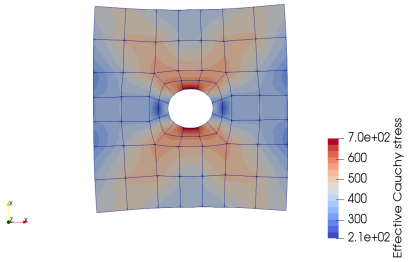

(d) Effective Cauchy stress field for the MS model utilising a RVE_L =2 mm considering a uniform traction boundary condition at the micro-scale.

Figure 5.22: Effective Cauchy stress field for the utilised Beam A models for a RVE_L =2 mm with a concentric circular void.

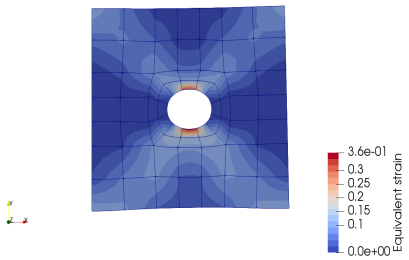

(a) Equivalent strain field for the DNS model utilising a RVE_L =2 mm.

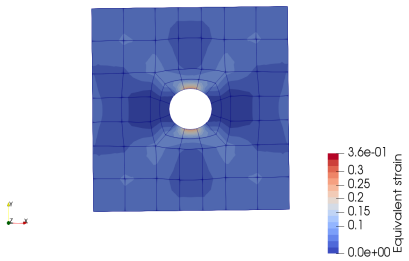

(b) Equivalent strain field for the MS model utilising a RVE_L =2 mm considering a linear boundary condition at the micro-scale.

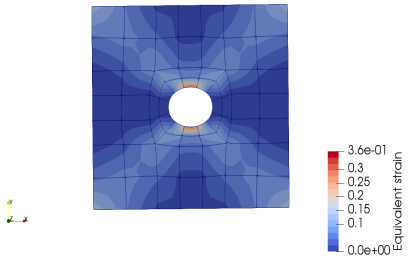

(c) Equivalent strain field for the MS model utilising a RVE_L =2 mm considering a periodic boundary condition at the micro-scale.

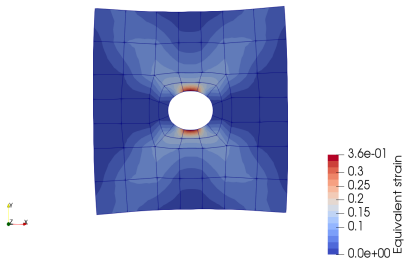

(d) Equivalent strain field for the MS model utilising a RVE_L =2 mm considering a uniform traction boundary condition at the micro-scale.

Figure 5.23: Equivalent strain field for the utilised Beam Amodels for a RVE_L =2 mm with a concentric circular void.

Since the periodic boundary condition is the one that provides more accurate results at the macro-scale, in the next figure is shown the obtained DNS solutions for the different RVEs characteristic lengths and the periodic boundary condition solution (since a first-order homogenisation method was utilised the results will be the same for each characteristic length).

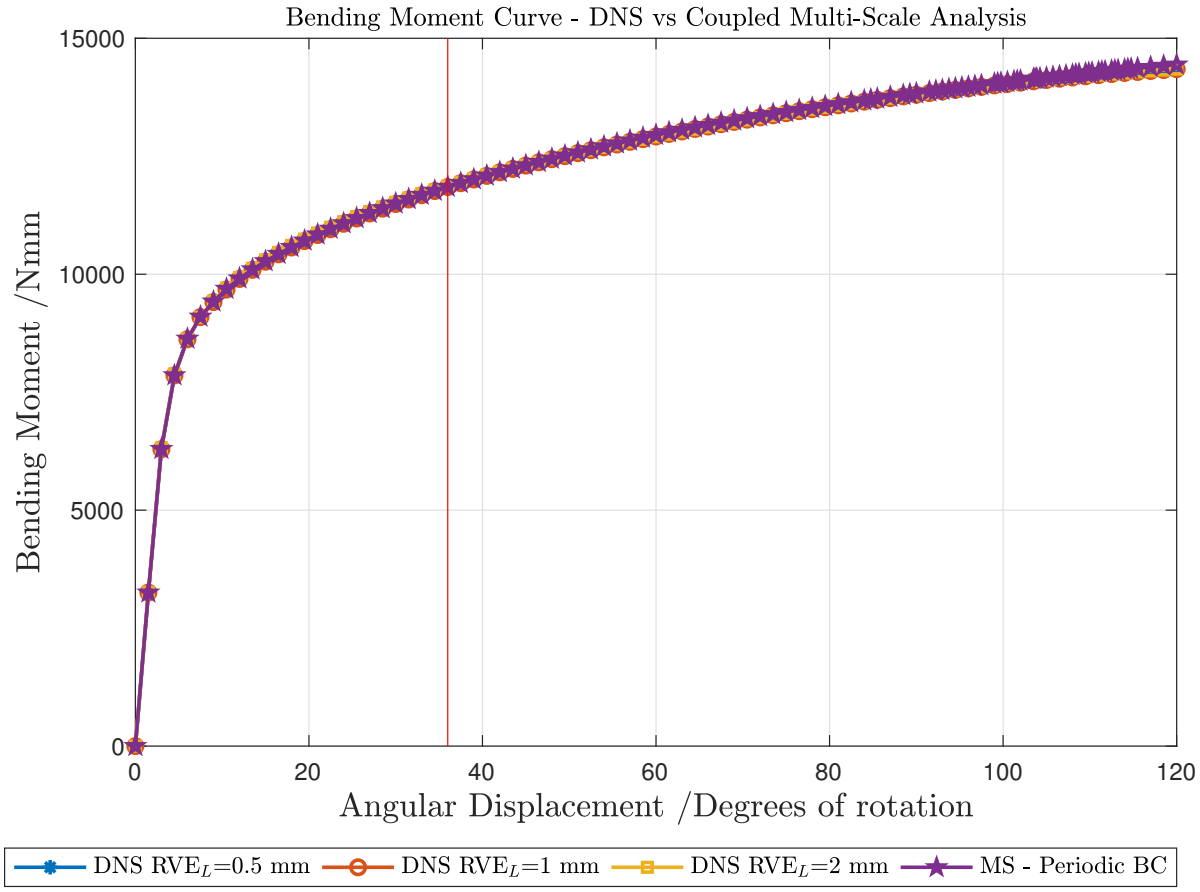

Figure 5.24: Reaction forces obtained for the different RVE characteristic lengths for the Beam B.

5.7 Bending Solicitation Utilising a Second-Order Homogenization Method

In this section will be presented the results of a case where only a micro-scale problem was solved by applying both the second-order displacements gradient and the deformation gradient that were obtained by the coupled multi-scale analysis in the Gauss points that were analysed in to a RVE. The boundary condition that was applied to the RVE was analogous to the periodic boundary condition in the first-order homogenization computational scheme.

The results obtained employing a second-order computational scheme will be compared, in terms of the effective Cauchy stress and equivalent strain fields, to the DNS ones already presented and, furthermore, the evolution of the effective Cauchy stress tensor (which can be considered as a measure of the norm of thefirst Piola-Kirchhoff stress tensor) depending on the equivalent strain tensor (which can be considered as a measure of the norm of the deformation gradient) will be compared with the results provided by the first-order homogenization results with the periodic boundary condition.

This studies will be made for the "critical characteristic size" of the RVE, which is of 2 mm, and for the case of the beam with the ratio $\frac{L}{\lambda} = 12.5$, once that the results obtained at the micro-scale employing a first-order computational homogenisation scheme cannot replicate the effects that were presented in the "corresponding" DNS RVE. All RVEs are represented with a scale factor in their displacements of 5.

5.7.1 Beam A

RVE with a characteristic length of 2 mm

Having already defined the RVEs that were considered, the results that were obtained at the micro-scale can be found in the next figures in terms of the effective Cauchy stress and equivalent strain, respectively.

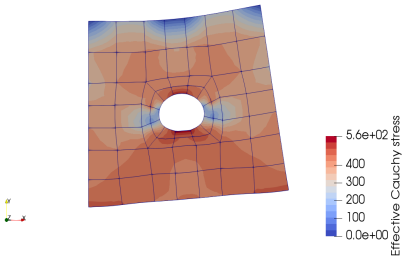

(a) Effective Cauchy stress field for the DNS model utilising a RVE_L =2 mm.

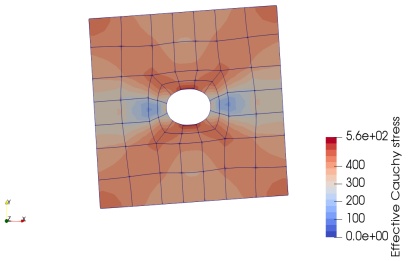

(b) Effective Cauchy stress field for the MS model utilising a RVE_L =2 mm employing a first-order homogenisation computational scheme.

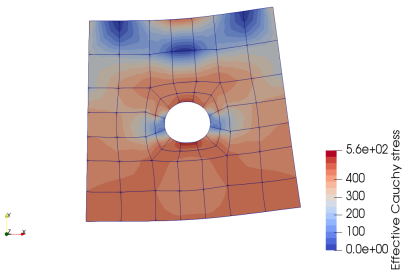

(c) Effective Cauchy stress field for the MS model utilising a RVE_L =2 mm employing a second-order homogenisation computational scheme.

Figure 5.25: Differences between the effective Cauchy stress field for the DNS and MS models utilising a RVE_L =2 mm. Utilised displacements scale factor of 5.

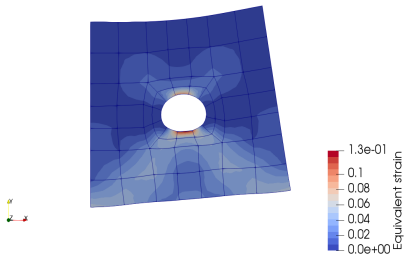

(a) Equivalent strain field for the DNS model utilising a RVE_L =2 mm.

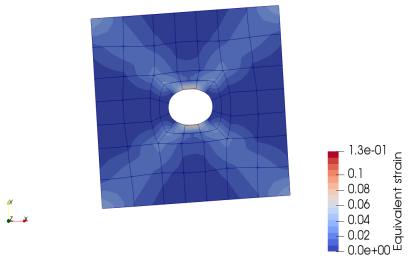

(b) Equivalent strain field for the MS model utilising a RVE_L =2 mm employing a first-order homogenisation computational scheme.

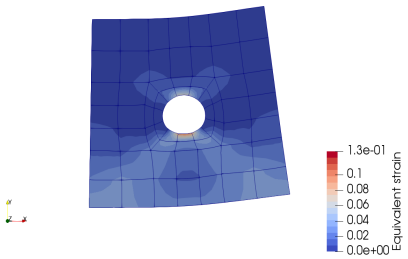

(c) Equivalent strain field for the MS model utilising a RVE_L =2 mm employing a second-order homogenisation computational scheme.

Figure 5.26: Differences between the equivalent strain field for the DNS and MS models utilising a RVE_L =2 mm. Utilised displacements scale factor of 5.

In terms of the evolution of the effective Cauchy stress depending on the equivalent strain at the micro-scale:

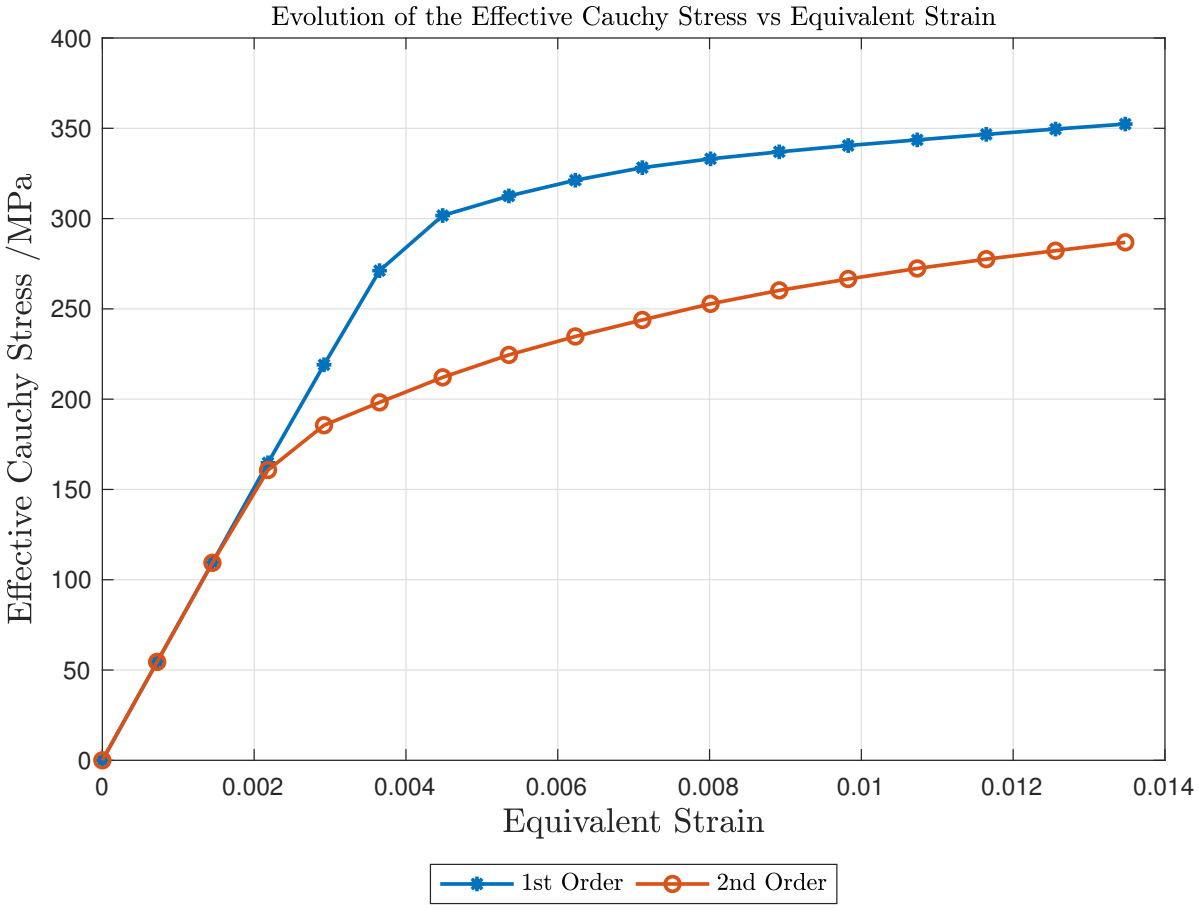

Figure 5.27: Evolution of the equivalent Cauchy stress depending on the equivalent strain.

5.8 Results Analysis

In this chapter, two different types of beams have been studied, one being thicker than the other. For the "thicker" beam, one can state that the results that have been obtained at the macro-scale (reaction bending moment) for all RVE characteristic length for both DNS and MS models tend to fit perfectly (considering the periodic boundary condition in the MS model). The linear and uniform boundary conditions tend to obtain higher and lower values for the bending moment and the probable cause for this happening is, once again, that they are the most and least restrictive boundary conditions. In terms of the micro-scale results it can be stated that for the Beam B, the effective Cauchy stress and equivalent strain fields provided by the DNS analysis tend to fit with the ones that have been obtained by the MS models, even for the RVEs with bigger characteristic length. It can be stated that, at the micro-scale level, both the periodic and the uniform traction boundary conditions seem to provide better results than the linear boundary condition.

For the Beam A, taking into consideration the results obtained at the macro-scale it can be stated that, for the RVEs with characteristic lengths of 0.5 and 1 mm the results provided by the MS models tend to fit (considering the periodic boundary condition) the results that are obtained by the DNS analysis. For the RVE with the bigger characteristic size, the DNS solution starts to drift away from the one that was obtained by the DNS model for a imposed rotation of 20 degrees, approximately- this can be an indication that a violation in the principle of separation of scales could be initiating. At the micro-scale, for both smaller RVEs (0.5 and 1 mm) the same conclusions that have been made for the Beam B can be taken. For the RVE with a characteristic size of 2 mm the results that have been provided by a first-order computational scheme don't fit with the results provided by the DNS analysis (in terms of effective Cauchy stress and equivalent strain fields). It can be seen that the MS models (using a first-order computational scheme) can not replicate what happens "inside" the corresponding RVE in the DNS solution, once that, for a first-order computational scheme, the imposed deformation gradient at the micro-scale (which is calculated in the corresponding Gauss point) is constant in all points of the RVE. Taking into account all informations about this case it is possible to state that a second-order computational homogenisation scheme would be required to have a more detailed study at the micro-scale.

Comparing the results that have been obtained between the DNS, with the first and second-order homogenisation schemes , for the periodic boundary condition, it can be stated that the second-order homogenisation should be used once that it can depict the deformation phenomenon that occurs in the DNS analysis. This is possible due to the fact that this computational scheme includes the second-order displacements gradient in its formulation which results in the fact the deformation gradient that is applied to the RVE is not constant and depends on the length of the RVE.

The differences between the results provided by the first and second-order homogenisation with periodic boundary conditions can be seen in terms of the evolution of the effective Cauchy

stress (measure of the norm of the homogenised first Piola-Kirchhoff stress tensor) depending on the equivalent strain (measure of the deformation gradient). In the elastic domain, both curves remain pratically identical, however, once the plastic behaviour begins, it can depict a large difference (in this case) in the two approaches. The fact is that the effective Cauchy stress in the second-order homogenisation scheme is lower that the first-order one, once that the latter doesn't contain information about the "neutral-axis" that happens in bending problems.

To sum up, in cases of bending, specially in "slender" beams, the characteristic length of the RVE already has a significant importance in the results that have been obtained, especially in terms of the results obtained in the micro-structure - therefore it might be useful to use a second-order homogenisation scheme in some cases as the case of the Beam A was (for the RVE with a characteristic length of 2 mm).

5.9 Conclusions

In this two distinct types of beams were studied, being one "thicker" that the other. It was shown that for the Beam B, the results provided by the DNS models and the MS ones were similar both at the macro and micro-scales, being the periodic boundary condition the one that provided "more accurate" results. Therefore, the principle of separation of scales wasn't violated and a second-order homogenisation wasn't necessary.

For the case of the Beam A, the increasing values of the RVE's characteristic length resulted in the occurrence of differences between the results provided by the DNS and MS models. It was shown that the curves provided from the DNS models started to differ from the ones provided by the MS model (being the periodic boundary condition the one that provided more accurate results). In the case when the characteristic size of the RVE was of 2 mm, the results provided by a first-order computational homogenisation didn't provided accurate results, being a second-order homogenisation needed.

Tu sum up, it is possible to conclude that for bending examples, the case of "slender" beams is more critical. It is also possible to state that in this kind of problems, a second-order homogenisation could be needed for a more accurate depiction of the deformation phenomenons that take place at the micro-scale. The RVE size is important, being that from a certain RVE size the principle of separation of scales can begin to be violated.

Chapter 6

Influence of the Heterogeneities and Material Behaviour in the Assessment of the Principle of Separation of Scales of Beams Under a Bending Solicitation

Having already analysed the PSS of a material with hardening behaviour, this chapter aims to enlarge the study of the PSS depending on the material behaviour. For that purpose, the example that was chosen to study was the most critical that was presented in Chapter 5, this is the case of the Beam A and the RVE_L =2 mm where it was already stated that a second-order homogenisation procedure should be applied in order to obtain information at the micro-scale level that is more reliable. All models (DNS and MS ones) are identical to the ones presented in the mentioned case, differing only in the material behaviour.

Furthermore the influence of the size of the heterogeneities of the material in the principle of separation of scales will be assessed. Therefore, one will analyse two distinct cases where the micro-structure is represented by a RVE with a circular void, which volume fraction is of 10% and 30%. It is important to note that, for this study, the RVEs that were analysed are identical to the ones that were analysed in Section 5.6 and the material is the aluminium alloy 2024-T351 that has already been presented, namely in Section 4.1.2.

Firstly one will present the materials that were studied, being one a material with elastic behaviour and the other one a "low-hardening" material resulting in a study of the two extremes of material behaviour. Then, one will present the results provided a the macro-scale, i.e. the reaction bending moment curves provided by the MS models (with linear, periodic and uniform traction boundary conditions) and by the DNS models. Secondly, one will present the results obtained at the micro-scale by comparing the equivalent strain fields of the RVE of the DNS simulation with the results obtained by the MS models for the periodic condition of both the first and second-order computational homogenisation. Lastly, a comparison its made between the evolution of the effective Cauchy stress tensor (can be taken as a measure of the norm of the first Piola-Kirchhoff stress tensor) depending on the equivalent strain (analogously to the

effective Cauchy stress tensor, it can be seen as a measure of the deformation gradient) between the first and second-order computational methods. It is important to note the the RVEs that were analysed are identical to the ones that were analysed in the previous chapter of this report (Section 5.6).

6.1 Material Behaviour Study

6.1.1 Material Definition

The material that was considered in both cases was aluminium, which properties have been already presented in Section 4.1.2 in Table 4.1. The difference to that case is that the behaviour of the material is going to be different, being one case an elastic behaviour and the second one a "low-hardening" material (modelled with a Von Mises model), being $\sigma_y = 352\text{MPa}$ for $\bar{\varepsilon_p} = 0$ and $\sigma_y = 452\text{MPa}$ for $\bar{\varepsilon_p} = 1$, hence, it is going to be assumed that the hardening behaviour of the material is linear in the plastic deformation zone.

6.1.2 Numerical Simulations

The properties of the numerical simulations were identical to the ones already presented in Section 5.5 being the only difference the number of increments in the uniform boundary condition for the case of the "low-hardening" material - in this case it was considered a number of 80 increments due to convergence problems.

6.1.3 Results Obtained

The results that were obtained will be presented in the next sections, accordingly to what is stated in introdutory remarks of this chapter. The representative displacement is of 48 degrees of rotation and it is represented by a vertical red line in the reaction curves. All micro-scale results are shown with a scale factor of 5 in terms of displacements.

6.1.3.1 Elastic Material

The results obtained at the macro-scale, the reaction bending moment, can be found bellow as follows.

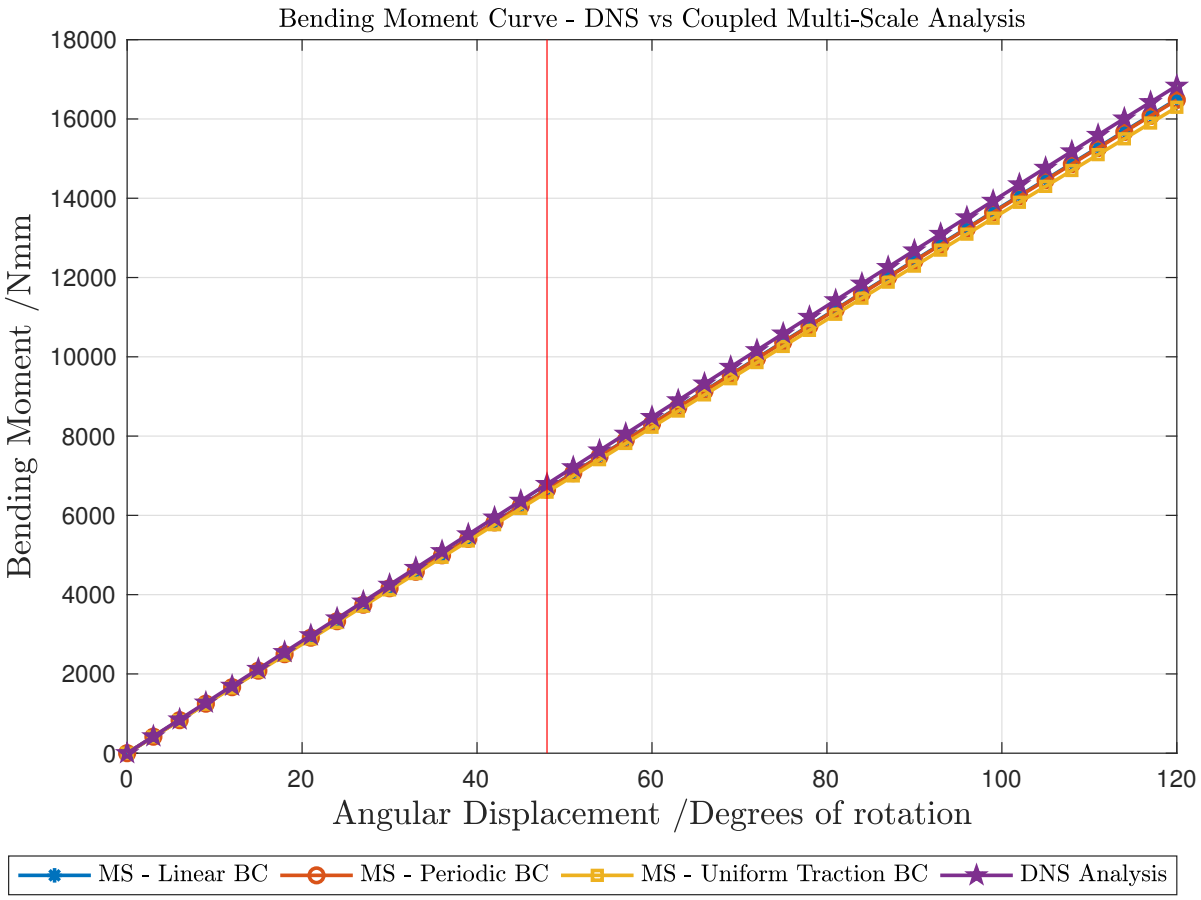

Figure 6.1: Reaction bending moment for the Beam A considering an elastic material behaviour.

Having already defined the RVEs that were considered, the results that were obtained at the micro-scale can be found in the next figures in terms of the equivalent strain.

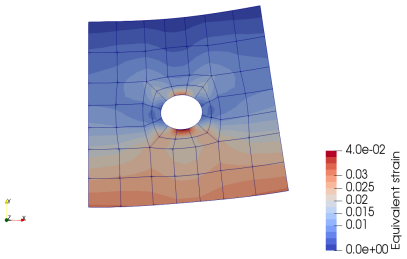

(a) Equivalent strain field for the DNS model utilising a RVE_L =2 mm.

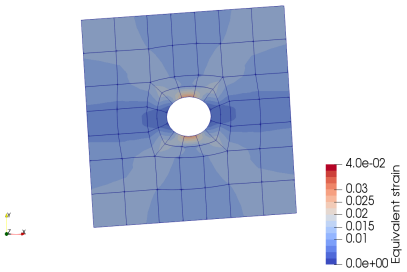

(b) Equivalent strain field for the MS model utilising a RVE_L =2 mm employing a first-order homogenisation computational scheme.

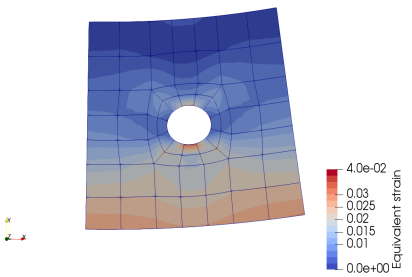

(c) Equivalent strain field for the MS model utilising a RVE_L =2 mm employing a second-order homogenisation computational scheme.

Figure 6.2: Equivalent strain fields for the material with elastic behaviour. Utilised displacements scale factor of 5.

In terms of the evolution of the effective Cauchy stress depending on the equivalent strain at the micro-scale:

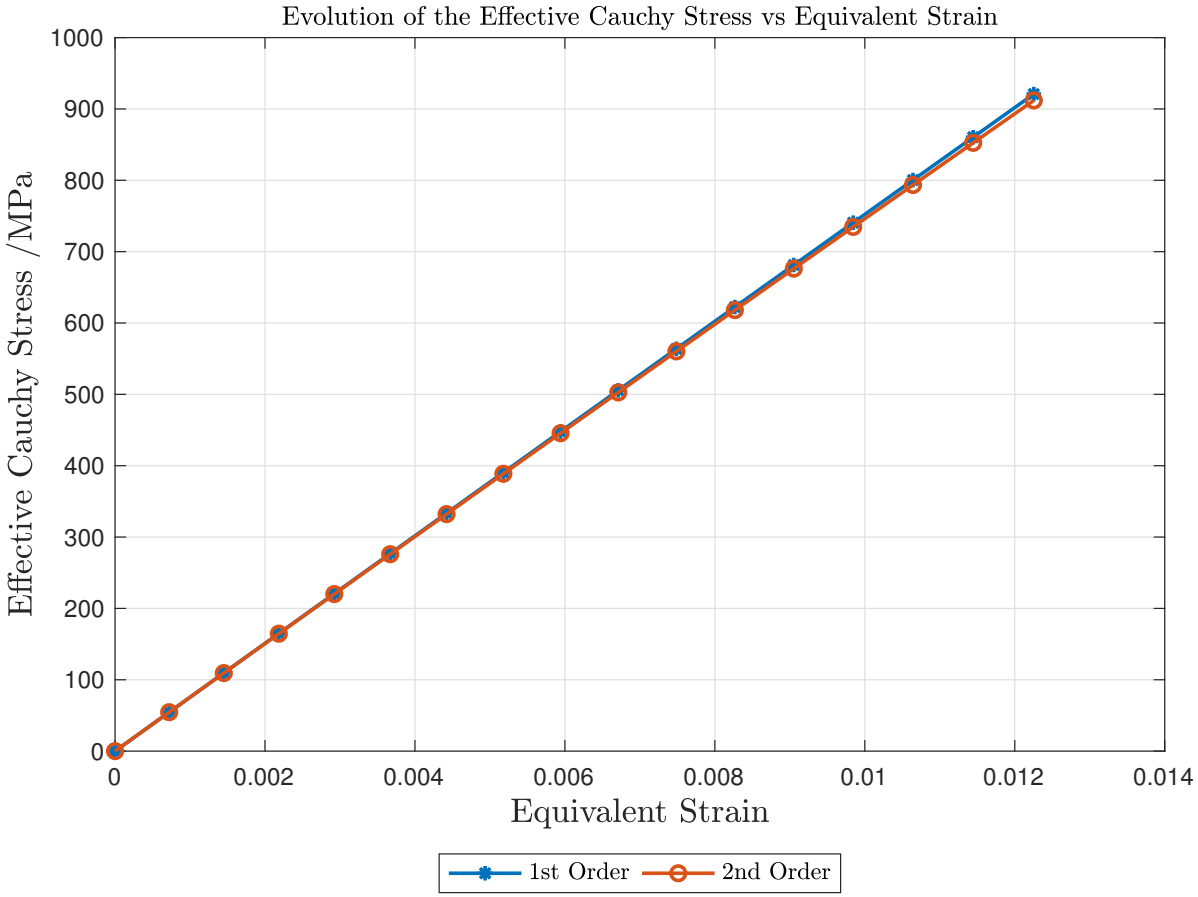

Figure 6.3: Evolution of the equivalent Cauchy stress depending on the equivalent strain.

6.1.3.2 Low Hardening Material

The results obtained at the macro-scale, the reaction bending moment, can be found bellow as follows.

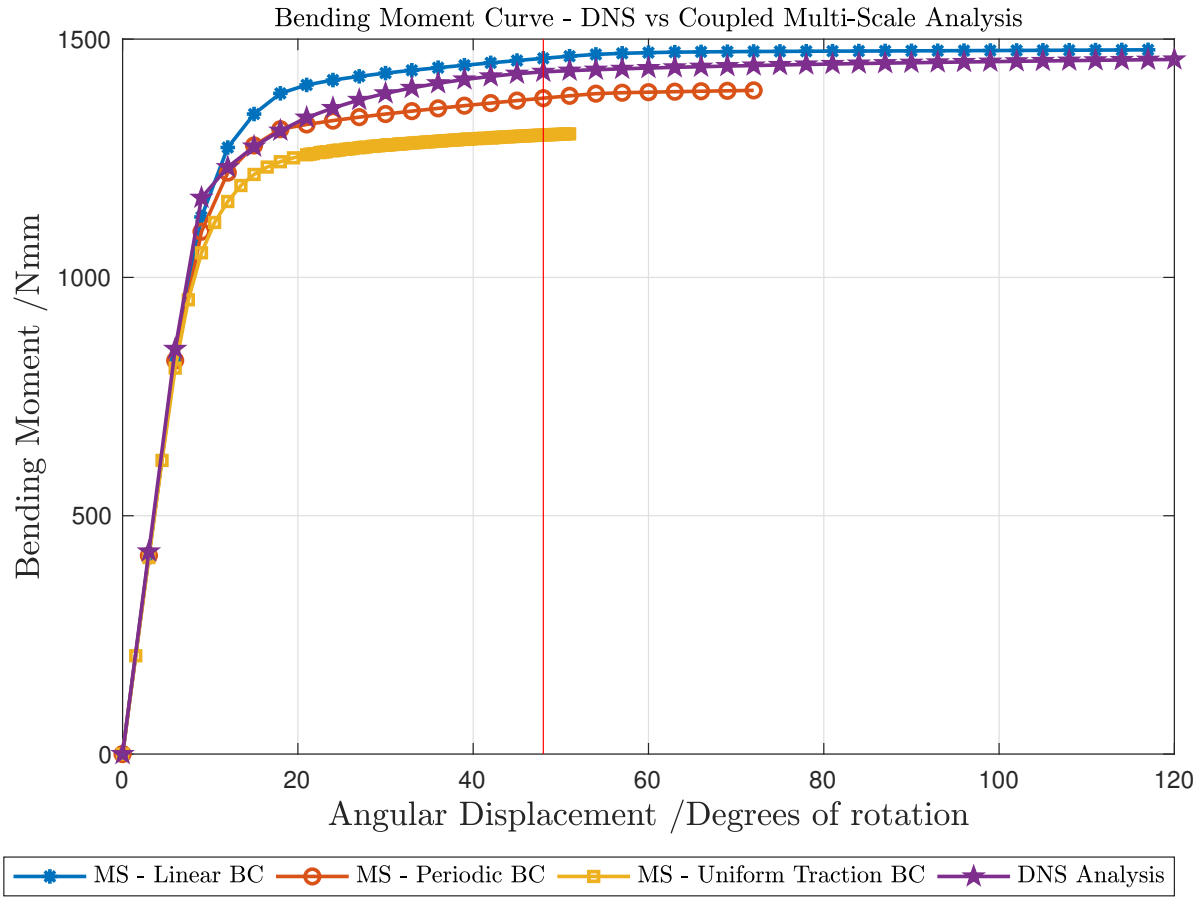

Figure 6.4: Reaction bending moment for the Beam A considering a "low-hardening" material behaviour.

Having already defined the RVEs that were considered, the results that were obtained at the micro-scale can be found in the next figures in terms of the equivalent strain.

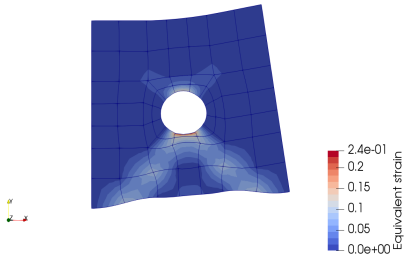

(a) Equivalent strain field for the DNS model utilising a RVE_L =2 mm.

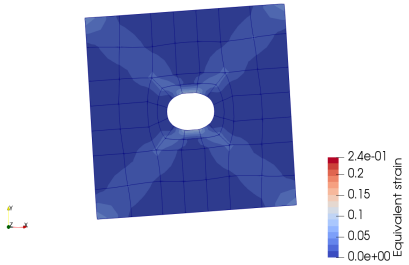

(b) Equivalent strain field for the MS model utilising a RVE_L =2 mm employing a first-order homogenisation computational scheme.

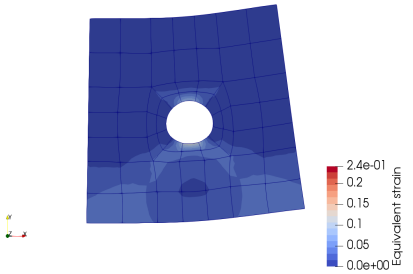

(c) Equivalent strain field for the MS model utilising a RVE_L =2 mm employing a second-order homogenisation computational scheme.

Figure 6.5: Equivalent strain fields for the material with "low hardening" behaviour. Utilised displacements scale factor of 5.

In terms of the evolution of the effective Cauchy stress depending on the equivalent strain at the micro-scale:

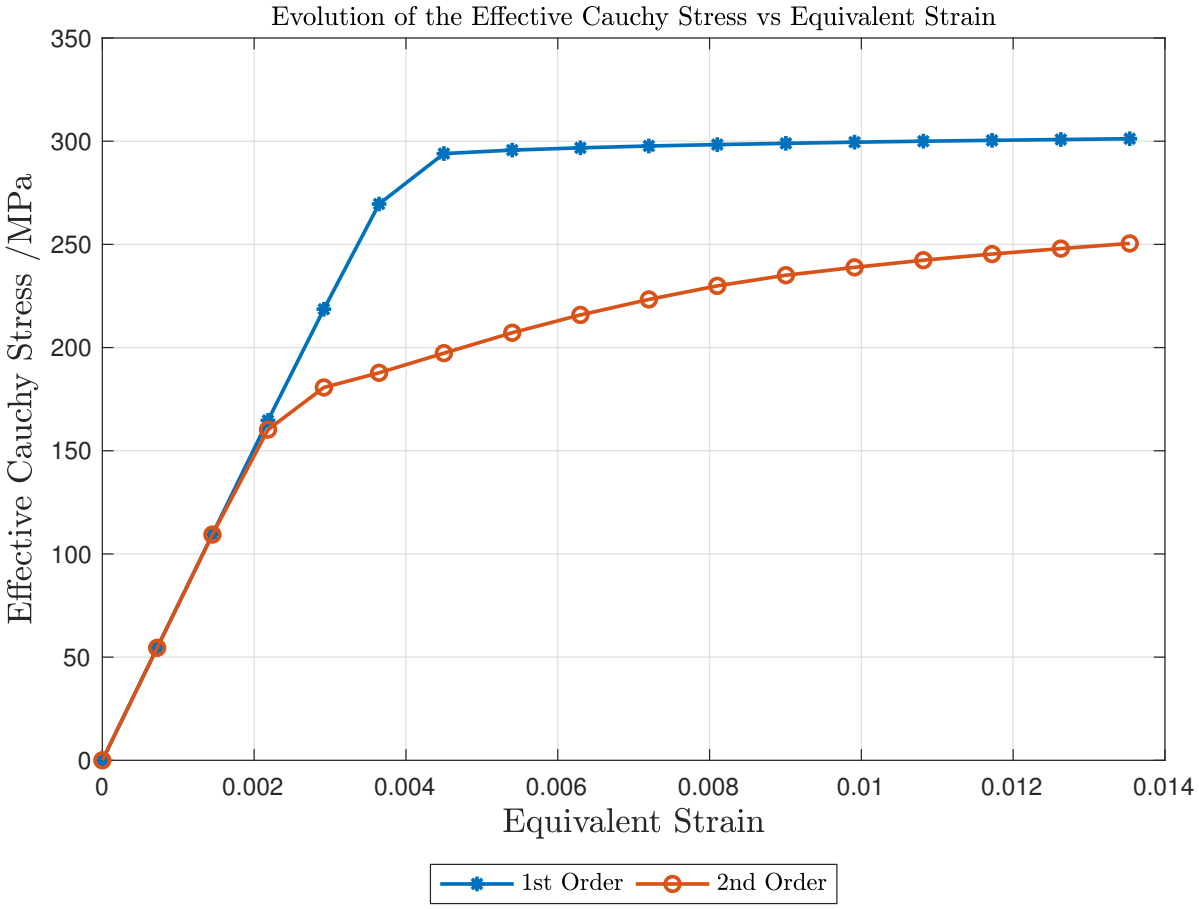

Figure 6.6: Evolution of the equivalent Cauchy stress depending on the equivalent strain.

6.1.4 Results Analysis

Two different types of material behaviour have been studied, being one a material with elastic behaviour and the other one a material with "low hardening" behaviour. For the elastic behaviour one can state that the results obtained at the macro-scale (reaction curves) for both the DNS and MS models (considering all boundary conditions) fit almost identically. For the material with a "low hardening" behaviour it is shown that the results between the DNS analysis and the MS one start to differ once the plastic regime begins.

The micro-structural results, for both material behaviours, in terms of the equivalent strain field, show that a second-order homogenisation procedure can replicate in a more exact way the microscopic deformation phenomenon that can be seen in the DNS analysis, leading to the conclusion, once again, that for this case (for the Beam A and a RVE with a characteristic length of 2 mm and with a bending solicitation) for a better understanding of the micro-structural strain field a second-order homogenisation scheme is more beneficial.

As for the evolution of the effective Cauchy stress (measure of the norm of the homogenised first Piola-Kirchhoff stress tensor) depending on the equivalent strain (measure of the deformation gradient), for the material with elastic behaviour, both curves remain pratically identical. However, for the material with "low hardening behaviour" the curves only remain identical until the beginning of the plastic regime, once that occurs, it can depict a large difference (in this case) in the two approaches.

6.2 Heterogeneities Size Study

6.2.1 Multi-Scale Model

The multi-scale model can be divided into two distinct models. The macro-scale model and the micro-scale one. The macro-scale model remains identical to the one utilised in Section 5.3.1.

6.2.2 Micro-Scale Mesh: Definition of the RVEs' Properties

The procedure to obtain the RVE geometry is the same as stated before in subsubsection 4.1.3.2. As it has already been stated in the introductory remarks of this chapter, two distinct cases of void volume fraction were analysed, being one of 10% and the other of 30%. The micro-scale meshes as well their properties can be found bellow. The type of elements that were utilised were a 8-noded quadratic element. A resume of the mesh properties can be found below in the

(a) Micro-scale mesh for the 10% void volume fraction RVE.

(b) Micro-scale mesh for the 30% void volume fraction RVE.

Figure 6.7: Micro-scales meshes of the micro-structures that have been studied.

following tables.

Table 6.1: Micro-scale mesh properties for the 10% void volume fraction RVE.

Number of Elements	Number of Nodes
64	240

Table 6.2: Micro-scale mesh properties for the 10% void volume fraction RVE.

Number of Elements	Number of Nodes
64	256

6.2.3 DNS Models

Having introduced the samples geometry and the micro-scale mesh it is now possible to define the DNS models that have been utilised. As it has already been stated in the introductory

chapters of the present report, a DNS simulation requires an explicitly modelation of the microsctructure of the material. The models that are going to be presented were made with the aid of the software GiD® and are presented below. Again, the highlighted RVEs are the ones that are going to be analysed later.

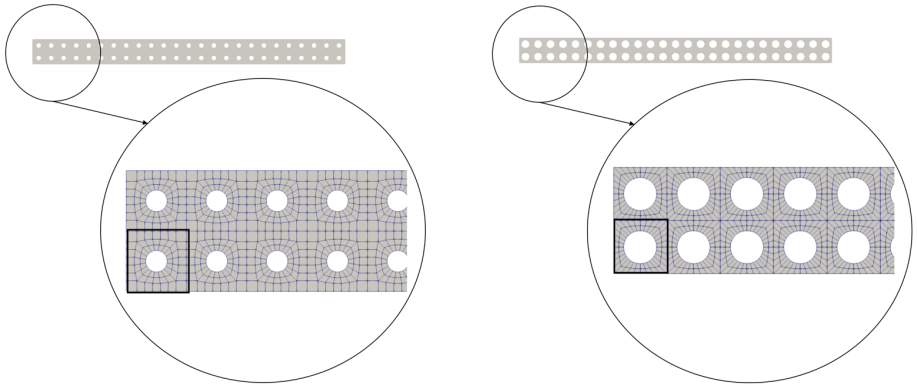

(a) Close up of the notch zone of the DNS model of the Beam A, using a 10% void volume fraction RVE.

(b) Close up of the notch zone of the DNS model of the Beam A, using a 30% void volume fraction RVE.

Figure 6.8: Close up of the notch zone of the different DNS models for the Beam A.

A resume of the DNS mesh properties can be found below on the following tables.

Table 6.3: DNS meshes properties for the 10% void volume fraction RVE.

Number of Elements	Number of Nodes
3200	10929

Table 6.4: DNS meshes properties for the 30% void volume fraction RVE.

Number of Elements	Number of Nodes
3200	11583

For all different types of meshes, the element type that was utilised was a 8-noded quadratic element with reduced integration.

6.2.4 Numerical Simulations

The properties of the numerical simulations were identical to the ones already presented in Section 5.5 being the only difference the number of increments in the uniform boundary condition for the case of the RVE with a 30% void volume fraction- in this case it was considered a number of 80 increments due to convergence problems.

6.2.5 Results Obtained

The results that were obtained will be presented in the next sections, accordingly to what is stated in introductory remarks of this chapter. The representative displacement is of 36 degrees of rotation and it is represented by a vertical red line in the reaction curves. All micro-scale results are shown with a scale factor of 5 in terms of displacements.

6.2.5.1 Void Volume Fraction of 10%

The results obtained at the macro-scale, the reaction bending moment, can be found bellow as follows.

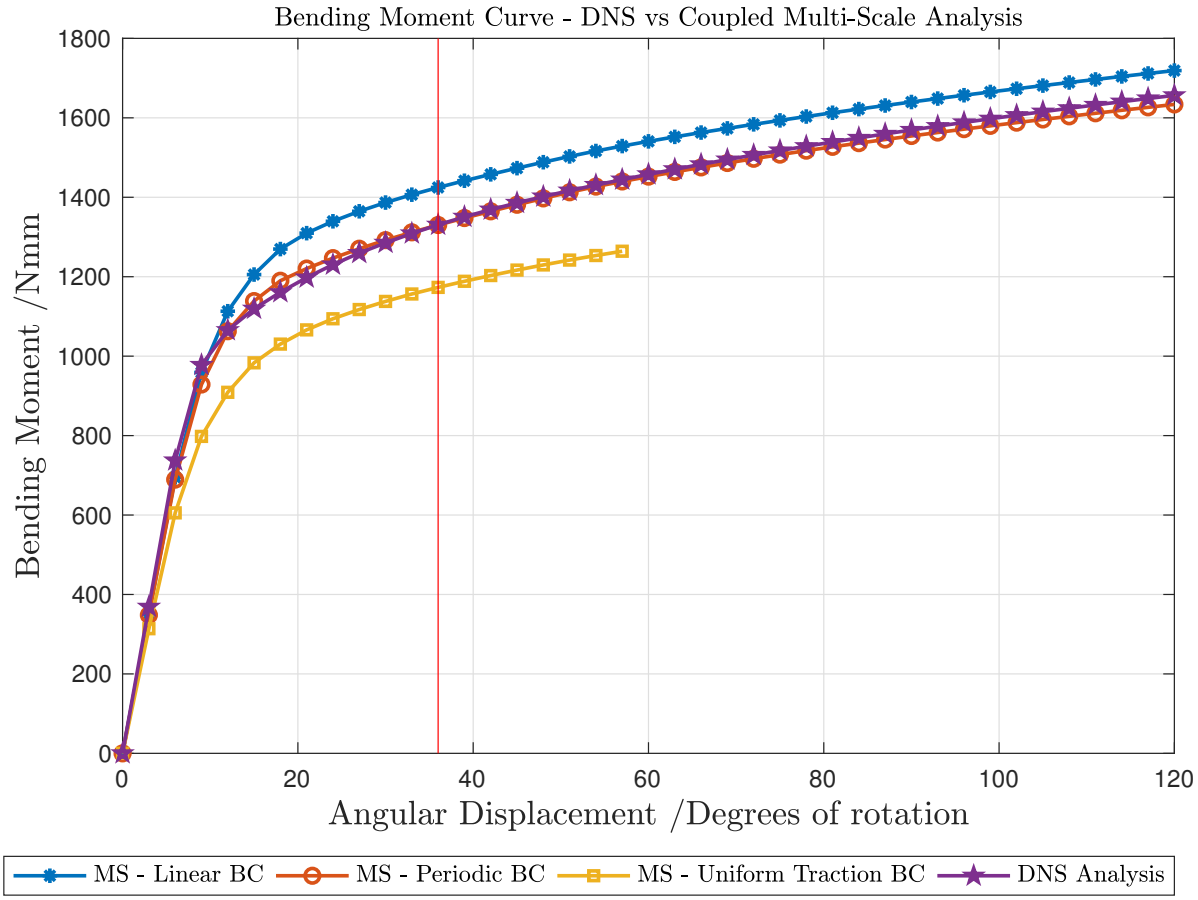

Figure 6.9: Reaction bending moment for the Beam A considering a 10% void volume fraction RVE.

Having already defined the RVEs that were considered, the results that were obtained at the micro-scale can be found in the next figures in terms of the equivalent strain.

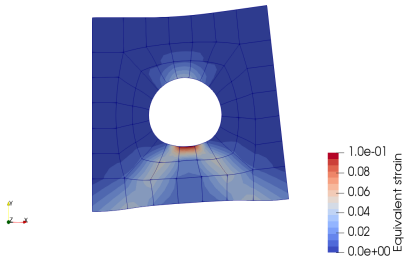

(a) Equivalent strain field for the DNS model utilising a 10% void volume fraction RVE.

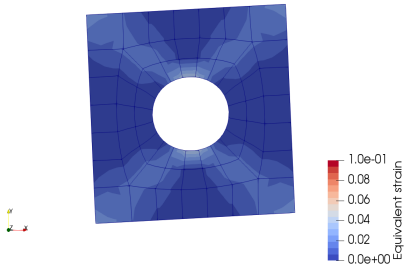

(b) Equivalent strain field for the MS model utilising a 10% void volume fraction RVE employing a first-order homogenisation computational scheme.

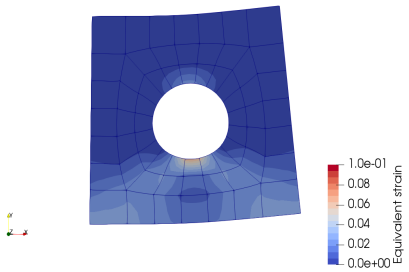

(c) Equivalent strain field for the MS model utilising a 10% void volume fraction RVE employing a second-order homogenisation computational scheme.

Figure 6.10: Differences between the equivalent strain field for the DNS and MS models utilising a 10% void volume fraction. Utilised displacements scale factor of 5.

In terms of the evolution of the effective Cauchy stress depending on the equivalent strain at the micro-scale. The representation is made until the equivalent strain that corresponds to the representative increment:

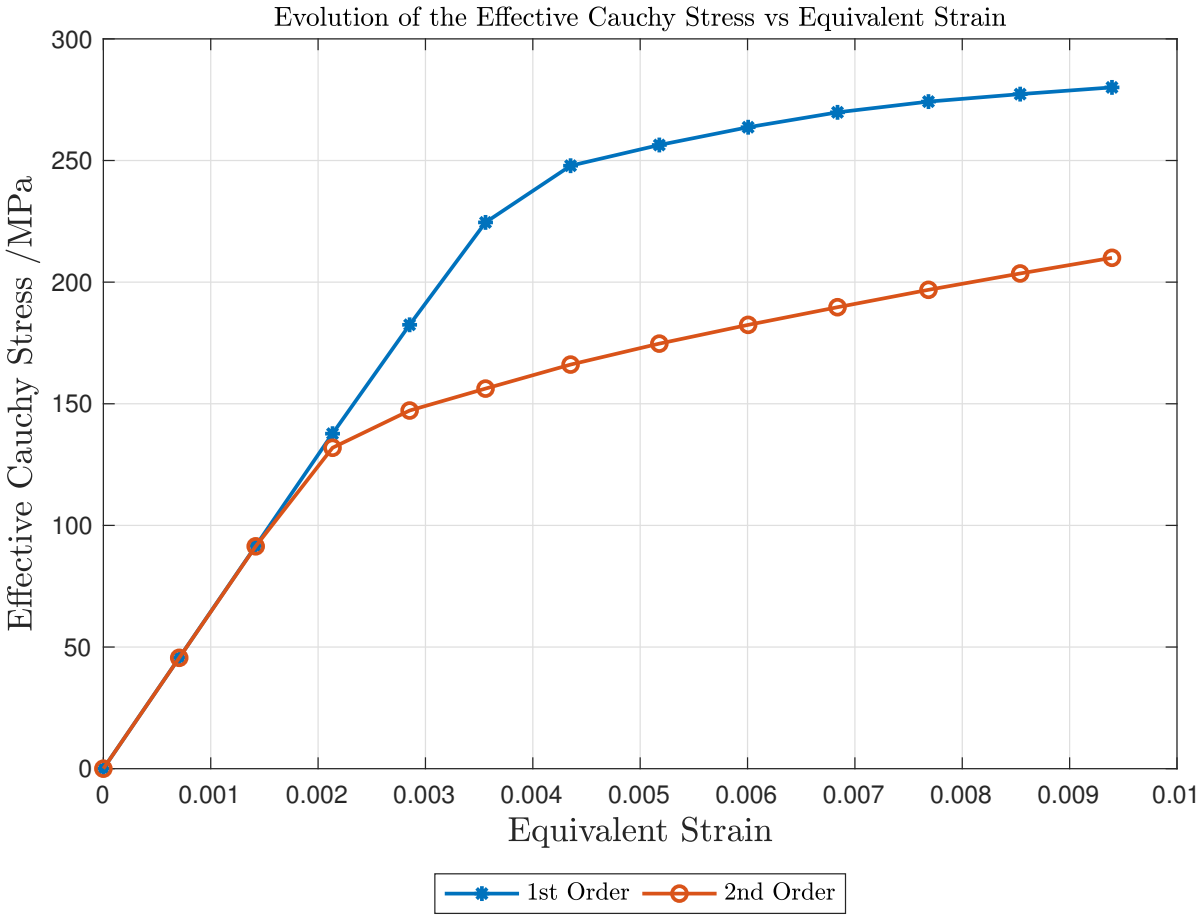

Figure 6.11: Evolution of the equivalent Cauchy stress depending on the equivalent strain.

6.2.5.2 Void Volume Fraction of 30%

The results obtained at the macro-scale, the reaction bending moment, can be found bellow as follows.

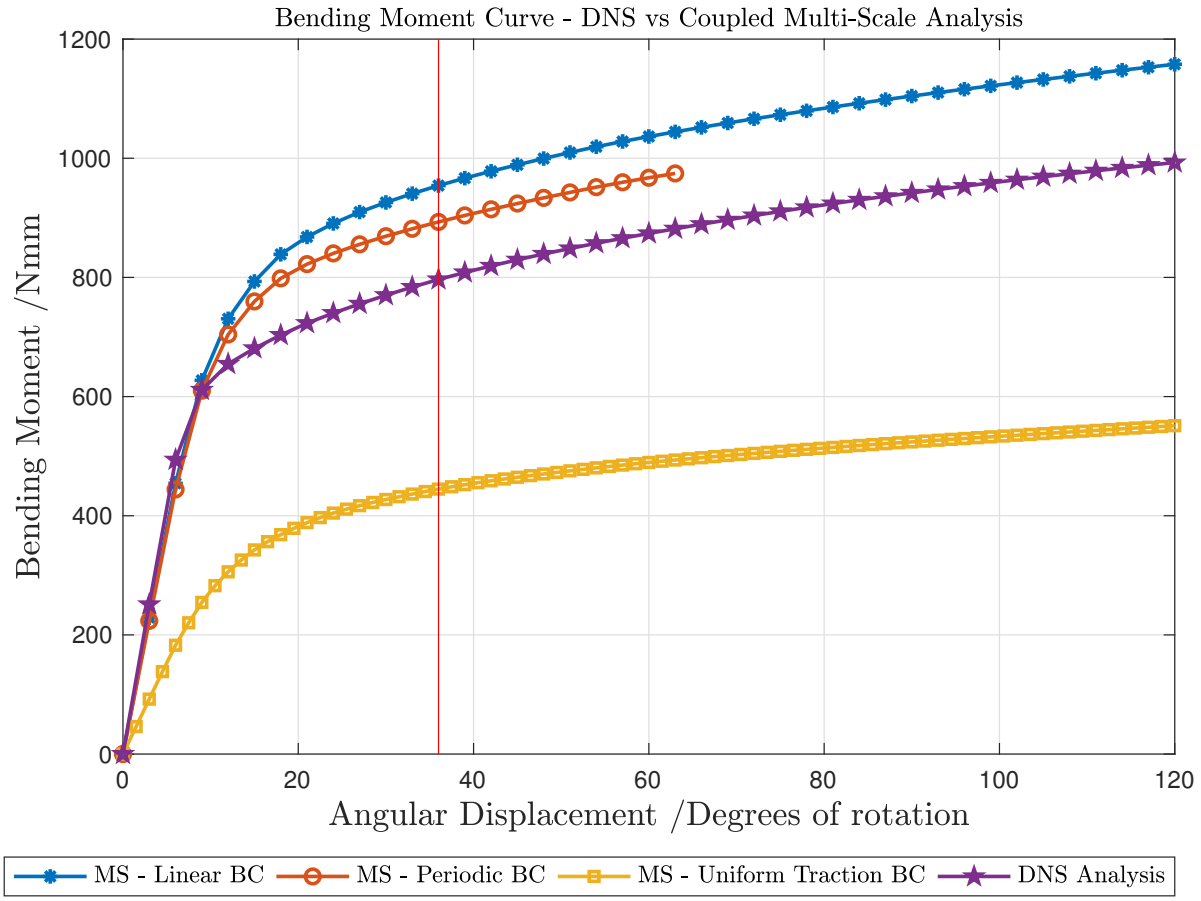

Figure 6.12: Reaction bending moment for the Beam A considering a 30% void volume fraction RVE.

Having already defined the RVEs that were considered, the results that were obtained at the micro-scale can be found in the next figures in terms of the equivalent strain.

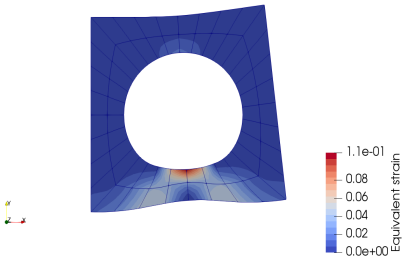

(a) Equivalent strain field for the DNS model utilising a 30% void volume fraction RVE.

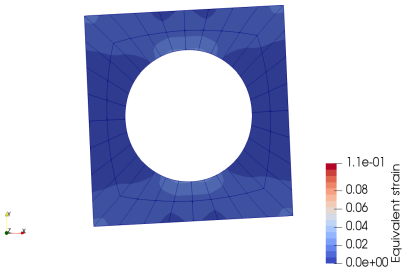

(b) Equivalent strain field for the MS model utilising a 30% void volume fraction RVE employing a first-order homogenisation computational scheme.

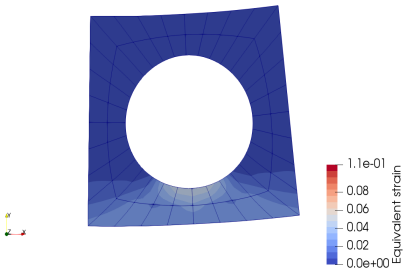

(c) Equivalent strain field for the MS model utilising a 30% void volume fraction RVE employing a second-order homogenisation computational scheme.

Figure 6.13: Differences between the equivalent strain field for the DNS and MS models utilising a 30% void volume fraction. Utilised displacements scale factor of 5.

In terms of the evolution of the effective Cauchy stress depending on the equivalent strain at the micro-scale:

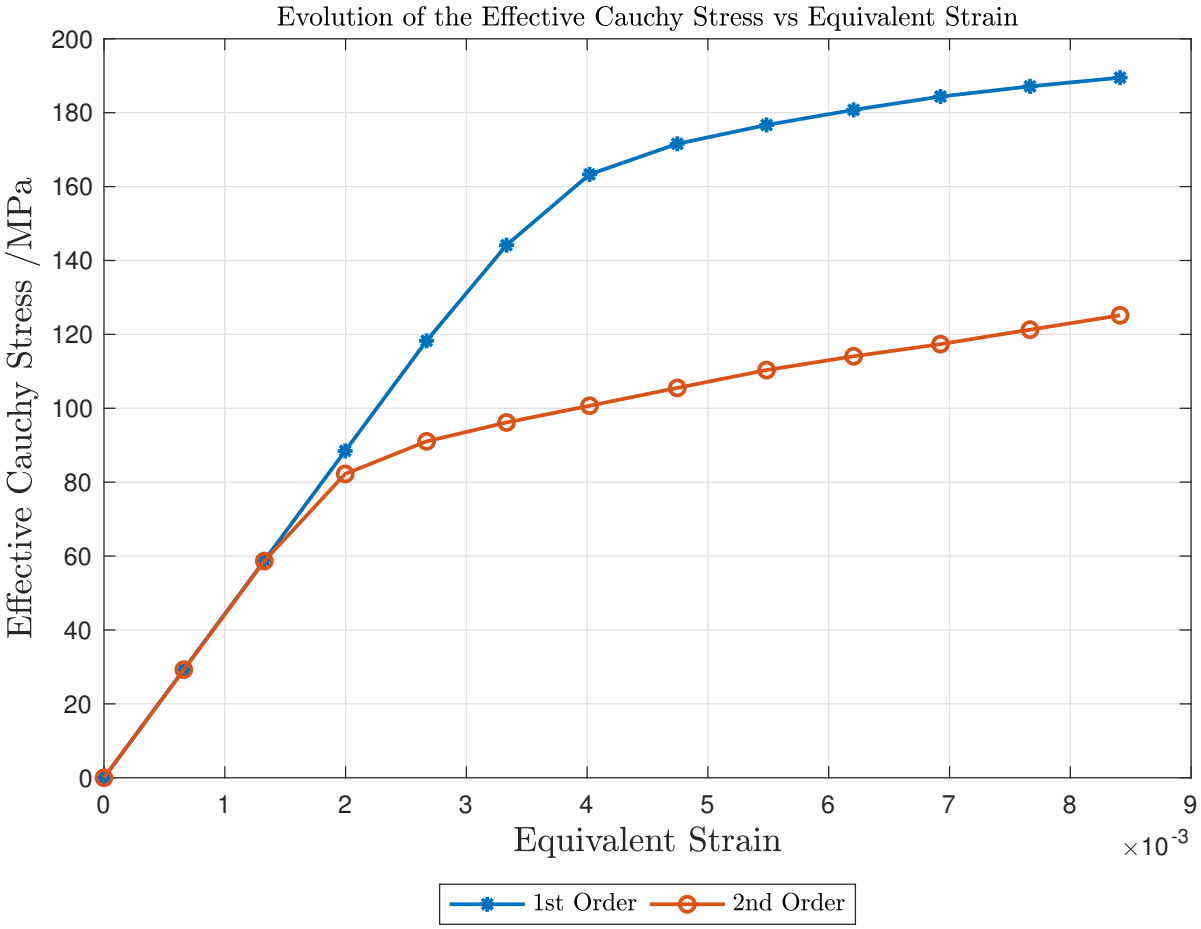

Figure 6.14: Evolution of the equivalent Cauchy stress depending on the equivalent strain.

6.2.6 Results Analysis

Two different kinds of RVE were studied, differing one from another in terms of the void volume fraction. In terms of the reaction curves it can be stated that for both cases, in the elastic domain, the curves provided by the DNS model fit almost perfectly with the curves that result from the MS analysis. Once the plastic behaviour starts to occur, it can be seen that for the RVE with a higher void volume fraction, the separation of the DNS curves from the ones that result from the coupled multi-scale analysis (once again, the periodic boundary condition that provides better results) is occured for a smaller prescribed rotation and is more significant than the case with a RVE with less void volume fraction.

The results obtained at the micro-scale (in terms of equivalent strain field) prove once again, that for the case that was analysed, a second-order homogenisation characterizes in a more accurate way the microscopic deformation phenomenon.

As for the evolution of the effective Cauchy stress (measure of the norm of the homogenised first Piola-Kirchhoff stress tensor) depending on the equivalent strain (measure of the deformation gradient), for both cases, the curves only remain identical until the beginning of the plastic regime, once that occurs, it can depict a large difference (in this case) in the two approaches.

6.3 Conclusions

In this chapter the influence of material behaviour and of the heterogeneities was studied for the "critical" case of the Chapter 5.

It was shown that for elastic materials, the DNS curve fitted the ones provided by the MS models. However, at the micro-scale, the results provided by a first-order homogenisation didn't provide accurate results in terms of the equivalent strain, being a second-order homogenisation needed.

For the "low hardening" behaviour it was shown that the DNS curve started to differ from the ones that were obtained by the MS modles. At the micro-scale, once again, a second-order homogenisation was needed to depict the micro-scale deformation phenomenon and, thus, providing results more closer to the ones obtained by the DNS analysis.

It was also shown that for larger void volume fractions, the curves provided by the DNS models would differ in a larger way the ones provided by the MS models. This can be explained by the fact that in RVEs with higher void volume fraction, the void promotes larger deformation variation throughout the RVE, making it impossible to a first-order homogenisation method to depict this behaviour properly. In terms of the micro-scale results it was once more shown that a second-order homogenisation was needed for a more accurate depiction of the micro-scale deformation phenomenon.

It is possible to conclude that not only does the RVE characteristic length has influence in the assessment of the principle of separation of scales, but also the deformation phenomenon that takes place at the micro-scale. In cases where the "variation" of the deformation inside the RVE is large, a first-order homogenisation cannot depict and provide accurate results, resulting

in a violation of the principle of separation of scales, therefore a second-order homogenisation must be employed.

Chapter 7

Conclusions and Future Works

In the present report, an assessment of the principle of separation of scales has been made taking into account several parameters such as the characteristic length of the RVE (were analysed three different lengths), type of solicitation (traction and bending), the material behaviour (elastic, "low-hardening" and hardening behaviours) and the size and type of the heteregeneities (voids and elastic inclusions).

Taking into account all the analysis made in those chapters it is important to conclude that for the traction solicitation, for both samples geometries (4 and 12 mm notches) the size of the RVE didn't produce major differences in the results obtained by the DNS and MS models, specially in the case where the heterogeneity was an elastic inclusion. Furthermore, it was demonstrated also, that for the RVEs with a circular void, the periodic boundary condition provided more accurate results in comparison with the DNS ones. For the RVE with an elastic inclusion, all boundary conditions provided accurate results also. The RVE's characteristic length made the results provided by the DNS and MS models differ on the bending solicitation, particularly for the beam with ratio $\frac{L}{\lambda} = 12.5$ (Beam A). It was demonstrated that for the RVE with a characteristic length of 2 mm the reaction curves obtained from the DNS model and the ones that resulted from the MS analysis started to differ slightly - once again, the periodic boundary condition was the one that provided better results. It was also demonstrated that in the case mentioned above, for an accurate demonstration of the microscopic deformation phenomena a second-order homogenisation computational scheme should be used, once that tje first-order homogenisation uses a constant deformation gradient throughout the RVE that is being analysed (resulting in the fact that the results that are provided by a MS model using a first-order homogenisation technique are independent of the RVE's characteristic length) whereas the second-order homogenisation technique includes the second order displacements gradient which results in the fact that the results are dependent of the RVE's size.

With the study of the curves evolution of the effective Cauchy stress depending on the equivalent strain for a first and second-order homogenisation computational scheme it was shown that during the elastic domain the results provided by both schemes fitted almost exacly.

This allows one to state that in the elastic domain, where the deformations are generally small (in the plastic domain localization of deformations starts to appear, i.e., the plastic domain is dominated by bigger deformations than the elastic domain, for the same material, obviously) the RVE size is not going to be preponderant in the results obtained at the macro-scale, once that they depend on the average of the properties determined at the micro-scale (i.e. of the homogenisation process). Furthermore, while analysing the material with an elastic behaviour, it was shown that even though the results provided by the first and second-order homogenisation schemes were different (in terms of equivalent strain field, the second-order homogenisation corresponded much better to the DNS results) the macro-scale results (for the DNS model and the coupled multi-scale model that uses only a first-order homogenisation) didn't show notable differences. However, for the material with the "low hardening" behaviour the same results started to differ. This allows one to state that the RVE characteristic length, by its own, doens't contribute for the principle of separation of scales. What makes the RVE size contribute is the magnitude of strain variations "inside" the RVE, this is, localization of strain that "only" occurs in plastic behaviour or with more complex RVEs (with higher void volume fractions, multiple voids, etc.). This fact was also proved right while analysing the two distinct kinds of RVEs with different void volume fractions, resulting in the fact that only the RVE with the void volume fraction of 30% provided results largely different when comparing the DNS with the MS ones. In that chapter it can been seen that for the two distinct RVEs, the equivalent strain field in the DNS model has a wider zone of yielding for the RVE with a void volume fraction of 30%.

Taking into account all the arguments presented above, it is possible to state that the RVE size, **by its own**, does not have a major influence in the PSS - despite that the RVE characteristic length is important to characterize in a proper way the strain/stress fields at the micro-scale. What is possible to state is that for bigger RVEs that are associated with higher magnitude of strain variations "inside" them the results (at the macro-scale and at the micro-scale) provided by the DNS model and the coupled multi-scale ones will differ. The difference will be bigger, the bigger the magnitude of the strain variation inside the RVE.

7.1 Future Works

Relying on the work earlier presented, further developments and validations could be done. For instance, it would be interesting to model different sizes of RVEs with a more complex micro-structure (multiple voids, higher void volume fractions, etc.) and to compare the results provided by the DNS simulations to the corresponding multi-scale ones. It would be interesting also to implement a fully working second-order homogenisation multi-scale model, once that for now it is only possible to solve this kind of problems at the micro-scale by introducing into a RVE the second-order deformation gradient (and the first-order also) that is calculated by the first-order multi-scale model - it would be expected that a multi-scale model with second-order homogenisation could provide results that would be closer to the ones that are provided by the

DNS models. It would be interesting also to remake the material study and the heterogeneities study present in this report for smaller RVEs and to document the results.

References

Bishop, J. E., Emery, J. M., Field, R. V., Weinberger, C. R., and Littlewood, D. J. (2015). Direct numerical simulations in solid mechanics for understanding the macroscale effects of microscale material variability. *Computer Methods in Applied Mechanics and Engineering*, Complete(287):262–289.

Carvalho, R. P. (2015). Análise do Comportamento Elasto-plástico de Materiais Dúcteis baseada em Homogeneização Computacional. Tese de Mestrado, Faculdade de Engenharia da Universidade do Porto.

Coenen, E. W. C., Kouznetsova, V. G., and Geers, M. G. D. (2012). Novel boundary conditions for strain localization analyses in microstructural volume elements. *International Journal for Numerical Methods in Engineering*, 90:1–21.

Ferreira, B. P. (2017). Avaliação da Precisão de um Modelo de Dano Contínuo através de um Modelo Multi-escala baseado em Homogeneização Computacional. Tese de Mestrado, Faculdade de Engenharia da Universidade do Porto, Porto.

Ghosh, S., Lee, K., and Moorthy, S. (1995). Multiple scale analysis of heterogeneous elastic structures using homogenization theory and voronoi cell finite element method. *International Journal of Solids and Structures*, 32(1):27–62.

Hashin, Z. (1983). Analysis of composite materials - A survey. *Journal of Applied Mechanics*, 50:481–505.

Hill, R. (1963). Elastic properties of reinforced solids: Some theoretical principles. *Journal of the Mechanics and Physics of Solids*, 11(5):357–372.

Holzapfel, G. A. (2000). *Nonlinear Solid Mechanics: A Continuum Approach for Engineering*. Wiley.

Kouznetsova, V. (2002). Computational homogenization for the multi-scale analysis of multi-phase materials. *Software Process: Improvement and Practice - SOPR*.

Neto, E. A. d. S. and Feijoo, R. (2006). Variational Foundations of Multi-Scale Constitutive Models of Solid: Small and Large Strain Kinematical Formulation.

Neto, E. A. d. S., Peric, D., and Owen, D. R. J. (2011). *Computational Methods for Plasticity: Theory and Applications*. John Wiley & Sons.

Rubin, D., Krempl, E., and Lai, W. M. (2012). *Introduction to Continuum Mechanics*. Newnes.

Tadmor, E. B., Miller, R. E., and Elliott, R. S. (2012). *Continuum Mechanics and Thermodynamics: From Fundamental Concepts to Governing Equations*. Cambridge University Press.

Teng, X. (2008). Numerical prediction of slant fracture with continuum damage mechanics. *Engineering Fracture Mechanics*, 75(8):2020–2041.

Zienkiewicz, O. C. and Taylor, R. L. (2000). *The Finite Element Method: Solid mechanics*. Butterworth-Heinemann.

Zienkiewicz, O. C., Taylor, R. L., and Zhu, J. Z. (2013). *The Finite Element Method: Its Basis and Fundamentals*. Butterworth-Heinemann.